Optimisation of a Novel Technique for Measuring Microviscous Environments in Living Cells



Alex Foley

Lincoln College

University of Oxford

A thesis submitted for the degree of

Doctor of Philosophy

Trinity 2020

This thesis is for Ray and Mary Jane,
without whom I could not have done this.

And for Neil, for helping me over the finish line.

Acknowledgements

I would firstly like to thank Prof. David Vaux for taking me in to his lab for misfit toys, and for his endless patience with my antics and my potty mouth. I would also like to thank the other members of the Vaux lab: Letitia Jean for all the cigarettes I've bummed over the years, which have likely taken at least a year off my lifespan; Ivan Boubriak for the always entertaining perspective from beyond the iron curtain; Helder Carmen and Marek Drodz for helping me get adjusted to the lab, and for shielding me from the wrath of She Who Must Not Be Named that time I broke her centrifuge; Lior Pytowski for at least attempting to veil his perennial annoyance my work style caused; Daina Šadurska for making my attendance look exceptional by comparison; and Zayra Núnez for all the sweets I pretended to enjoy. Special mention to Swaraj Dash for making this thesis look beautiful. Finally, I would like to thank Niall Moon and Max Haughey for synthesising the probes I have used throughout this project.



Statement of Originality

Parts of work reported in this Thesis were published in the following manuscripts with permission from all of the authors:

1. Jean, L. *et al.* The physiological and pathological implications of the formation of hydrogels, with a specific focus on amyloid polypeptides. Biomolecules 7, 70 (2017).

2. Pytowski, L. *et al.* A novel technique for mapping viscosity in discrete subcellular locations with a BODIPY based fluorescent probe (preprint). doi:10.1101/522532

Abstract

Microviscosity is a critical physical parameter to be taken into account when modelling cellular environments, and yet it has largely been ignored in cell biology because of the technical impediments to measuring it in cells. Traditional methods of measuring viscosity operate on far too gross a scale to be useful for making measurements on the cellular level, while more granular techniques all suffer from their own limitations. Molecular rotors, in combination with Fluorescence Lifetime Imaging Microscopy (FLIM), present a means of overcoming many of these limitations. However, to date, most molecular rotors for use in cell biology rely upon the addition of specific chemical groups for delivery to discrete organelles. In this thesis, I endeavour to optimise a novel BODIPY-based molecular rotor that has a benzyl guanine group, allowing it to be targeted to any protein tagged with the SNAP-tag enzyme. We show that BG-BODIPY is well tolerated by cells, and can be targeted to a range of different organelles, both membrane bound and membraneless. We then go on to show that it can be targeted to much smaller targets than whole organelles, namely the nuclear pore complex. Finally, we show that BG-BODIPY can stain whole semi-terrestrial invertebrates and monitor their internal states during desiccation, making it one of the most versatile molecular rotors developed to date.

Name: Alex Foley

Department: Sir William Dunn School of Pathology

College: Lincoln College

Word Count: 30,000

Contents

1 Introduction **1**

1.1 Understanding microviscosity 2
1.2 Methods for measuring viscosity 3
1.2.1 Single particle tracking 3
1.2.2 Fluorescence anisotropy 4
1.2.3 Molecular rotors 6
1.2.3.1 Lifetime-based rotors 7
1.2.3.2 Ratiometric motors 8
1.3 Time-correlated single photon counting 9
1.4 Fluorescence lifetime imaging microscopy 11
1.5 Biological hydrogels 13
1.5.1 Physiological hydrogels 16
1.5.1.1 Bacterial biofilms 16
1.5.1.2 Hydrophobins 17
1.5.2 Pathological amyloid hydrogels 18
1.5.2.1 IAPP and type II diabetes mellitus 18
1.5.2.2 Amyotrophic lateral sclerosis and frontotemporal dementia 18

2 Materials & Methods **22**

2.1 Buffer preparation 22
2.2 Cell culture 22
2.3 Plasmid DNA preparation and transfection 22
2.4 Immunofluorescence 23
2.5 Macrophage experiments 23
2.5.1 Macrophage preparation and culture 23
2.5.2 Macrophage phagocytosis assay 23
2.6 Confocal microscopy 24

2.7 Creation of the microfluidic chamber grids 24
2.8 Viscosity probe calibration 24
2.9 Generation of SNAP-tag/mCherry cell lines by CRISPR/Cas9 25
2.9.1 Donor plasmid generation 25
2.9.2 Localisations signals 25
2.9.3 gRNA plasmid generation 26
2.9.4 Transfection and cell sorting 26
2.10 Generation of SNAP-tag/nucleoporin cell lines by CRISPR/Cas9 . . 26
2.10.1 Donor plasmid generation 26
2.10.2 gRNA plasmid generation 26
2.11 SNAP-tag labelling for FLIM and confocal microscopy 28
2.12 Fluorescence lifetime measurements 28
2.13 Tardigrade culture and staining 28
2.14 Tardigrade tun formation 29
2.15 Rotifer culture and desiccation 29

3 Optimisation, calibration, and proof of principle of BG-BODIPY in human cells 30
3.1 Introduction 30
3.2 Results 33
3.2.1 BODIPY-C12 can detect phagocytosis in macrophages 33
3.2.2 Synthesis of BG-BODIPY and its longer linker derivatives . . 35
3.2.3 Fluorescence spectra of BG-BODIPY, 2-linker BG-BODIPY, and 3-linker BG-BODIPY 36
3.2.4 BG-BODIPY is sensitive to viscosity in the lifetime and intensity domains 39
3.2.5 BG-BODIPY is non-toxic to mammalian cells 40
3.2.6 BG-BODIPY targets specifically to SNAP-tags expressed in various cellular locations 41
3.2.7 BG-BODIPY reports distinct lifetimes at various cellular locations 43
3.2.8 Mapping cellular viscosity using BG-BODIPY in both the intensity and lifetime domains 45
3.2.9 mCherry lifetime dominates BG-BODIPY in FLIM images . . 47
3.2.10 BG-BODIPY can discriminate microviscosities in different sub-compartments of the same organelle 49

3.2.11 BG-BODIPY can target to and measure viscosity in membraneless organelles . . . 51
3.3 Discussion . . . 54

4 Using BG-BODIPY to probe the nuclear pore complex 58
4.1 Introduction . . . 58
4.1.1 The nuclear pored complex: structure and function . . . 58
4.1.2 Barrier nucleoporins . . . 59
4.1.3 Models of NPC selective barrier function . . . 60
4.2 Results . . . 63
4.2.1 BG-BODIPY detects changes in microviscosity during IAPP gelation . . . 63
4.2.2 BG-BODIPY can target to NPCs . . . 66
4.2.3 FLIM of transiently expressed FG-nups . . . 67
4.2.4 Mitoxantrone alters the microviscous environment of transiently expressed nup214 . . . 69
4.2.5 Generation of cell lines . . . 71
4.2.6 FLIM measurements of tagged FG-Nups . . . 73
4.2.7 Disrupting the NPC permeability barrier to investigate its phase . . . 74
4.2.8 Ac5SGlcNAc treatment did not disrupt the permeability barrier . . . 75
4.2.9 A note on the picture from the perspective of nuclear transport factors . . . 77
4.3 Discussion . . . 79

5 Investigating invertebrate cryptobiosis with BG-BODIPY 81
5.1 Introduction . . . 81
5.2 Results . . . 85
5.2.1 Uptake and distribution of BG-BODIPY in whole eukaryotic organisms . . . 85
5.2.2 Viscosity measurements of tardigrades in physiological conditions . . . 85
5.2.3 Internal viscosity of tuns formed in response to desiccation . . . 87
5.2.4 *H. exemplaris* appears to tolerate osmotic stress . . . 90
5.2.5 Tuns formed in response to desiccation and osmotic stress have differing internal viscosities . . . 90

5.2.6 Measuring microviscosity in bdelloid rotifers 91
5.2.7 Rotifer desiccation leads to a sharp increase in viscosity . . . 93
5.3 Discussion 94

6 Discussion **97**
6.1 Summary of results 97
6.2 Inferences from results 100
6.3 Future directions 102

Bibliography **106**

List of Figures

1.1 **The Principle of TCPSC.** The waveform of optical output is extrapolated from a histogram with many even time bins, which builds up as numerous photons hit the detector at various time points after each pulse. Reproduced from B&H TCSPC handbook (Becker, 2015). 10
1.2 **The principle of CFD.** The deleterious contribution of timing jitter is demonstrated on the left. The right shows how the zero cross point of the input and delayed pulses is independent of amplitude. Reproduced from B&H TCSPC handbook (Becker, 2015). 11
1.3 **Architecture of a classic TCSPC device.** Reproduced from Becker (2015). 12

3.1 **Pockets of low lifetime around phagocytosed beads.** Macrophages labelled with BODIPY-C12 and introduced to opsonized beads. Once they were phagocytosed, we observed spots of high lifetime in the exact position of the beads, surrounded by pockets of low lifetime. Arrows indicate better examples. 34
3.2 **BODIPY-C12 reports changes in internal viscosity of macrophages during phagocytosis.** a. Lifetime histograms and b. FLIM images of macrophages at different time points following the introduction of opsonized beads. 35
3.3 **Chemical structures of molecular rotors used in this thesis.** a. BG-BODIPY b. BODIPY-C12 c. The longer linker versions of BG-BODIPY where the portion in brackets indicates the rigid phenylacetylene linker moiety that is repeated n times, either twice or three times in the 2-linker and 3-linker probes. 37
3.4 Fluorescence spectra of BG-BODIPY and its longer linker derivatives. 38
3.5 **The Isocell microfluidics printer.** Inset shows an example of a grid printed by the Isocell under FC40. 39

3.6 **BG-BODIPY reports microviscosity in both the lifetime and intensity domains and is pH insensitive.** Calibration of BG-BODIPY. a. The lifetime of BG-BODIPY in picoseconds (z-axis) measured at various pH values (y-axis) and glycerol concentrations (x-axis). b. The log plot of fluorescence lifetime as a function of the log viscosity for BG-BODIPY in pH 7 MOPS buffer. The function is linear, expressed by the equation $Y = 0.3035X + 2.581$. c. The intensity of BG-BODIPY fluorescence measured at various pH values (y-axis) and glycerol concentrations (x-axis). d. The ratio of lifetime over intensity at various pH values (y-axis) and glycerol concentrations (x-axis). 41

3.7 **BG-BODIPY does not affect cell viability.** Cells were treated with BG-BODIPY as described in the methods and were imaged in an Incucyte for 18h every 5 minutes. From left to right, top to bottom: WT, ER, Golgi apparatus, Lysosomes, Peroxisomes, Mitochondria, Nucleoplasm, Cytoplasm mCherry-SNAP-Tag tagged cells lines. We show here the beginning and ending timepoints, demonstrating continued cell division. 42

3.8 **Unspecific bound BG-BODIPY can be removed with fatty acid free BSA containing DMEM washes.** a. Green channel fluorescence images of cells stained with BG-BODIPY and washed with 5% BSA for 3 x 5 minutes, 3 x 10 minutes, or 3 x 20 minutes compared with cells that had not been stained at all. b. A graphic depiction of the relative fluorescence intensities of the various washing conditions compared with the unstained cells. Only the 5 minute washes are significantly brighter than the control. 43

3.9 **BG-BODIPY targets specifically to subcellular compartments.** Colocalization of Mitotracker with transient expression of a Cox8/SNAP-tag fusion protein (Overlap Coefficient=0.986 rs^2= 0.971). 44

3.10 **BG-BODIPY targeted to different cellular environments reports different fluorescent lifetimes.** FLIM images and lifetime histograms for BG-BODIPY labelling of cells expressing the pSnapf-ADR and pSnapf-COX8A plasmids. 45

3.11 **BG-BODIPY targets to organelles expressing SNAP-tag with targeting sequences from the AAVS1 site.** Colocalization of Mitotracker with A. mCherry and BG-BODIPY targeted to the mitochondria via residues 1 to 29 of HsCOX8 (Overlap Coefficient=0.938 r^2=0.879). 46
3.12 **mCherry-BG-BODIPY can be targeted to all cellular compartments and reports relative microviscosity.** The viscosity is highly variable in different cellular compartments. The mCherry-SNAP-Tag fusion protein targeted to distinct cellular compartments was constitutively expressed from the AAVS1 locus and and tagged with BG-BODIPY by subsequent incubation with the probe. Ratiometric analysis of the fluorescence intensity of mCherry and BODIPY enabled us to assess the compartment viscosity. The analysis shown is based on 3 experimental replicates of approximately 40 to 50 cells each. 48
3.13 **Fluorescence recovery of mCherry after bleaching.** Images show a time course of the mCherry/SNAP-tag line that targets to the ER. A large square area in the bottom portion of each field of view has been bleached by the 559 laser, while a strip at the top has been left unbleached for reference. Recovery was measured for 80 minutes, or roughly the amount of time it took to stain cells with BG-BODIPY following bleaching and set them up on the Olympus for imaging. . 49
3.14 **Effect of bleaching of mCherry on the BG-BODIPY lifetime.** a. FLIM images of mCherry/SNAP-tag targeted to the ER labelled with BG-BODIPY. The left hand image was taken without the mCherry having been bleach while the right hand image was acquired post bleaching. b. A comparioson of the lifetime histogram of cells targeting mCherry and BG-BODIPY to the ER and peroxisomes prior to and after bleaching. 50

3.15 **BG-BODIPY reports microviscosity in sub cellular compartments.** a. Diagram of BG-BODIPY localisation in the mitochondrial matrix and mitochondrial intermembrane space. b. Intensity profiles orthogonal to mitochondrial edges showing the single and double peaks of intensity confirming the correct localisation of BG-BODIPY. c. A histogram showing the viscosities reported from FLIM analysis of BG-BODIPY bound to the Cox8/SNAP-tag fusion protein or in the mitochondrial matrix. Mean viscosity for intermembrane space and matrix are respectively 309 cP and 600 cP. 52

3.16 **BG-BODIPY targets to and measure viscosity in membraneless organelles.** a. C-terminal fragment of TDP43 labelled with BG-BODIPY targets to the nucleoplasm plus a diffuse cytoplasmic signal. b. In the presence of $ZnCl_2$ TDP43 forms cytoplasmic condensates. c. the microviscosity of stress granules is significantly higher to the nucleoplasm and cytoplasm. 54

3.17 **Mitoxantrone dissolves TDP-43/GFP containing cellular condensates.** Cells that had been treated overnight with $ZnCl_2$ induce the formation of TDP-43/GFP positive cytoplasmic condensates (large examples are highlighted with white arrows), were treated with mitoxantrone. Condensates have nearly disappeared after 90 minutes of treatment. 54

4.1 **Models of NPC selective permeability barriers.** a. The virtual gate model, in which FG-nups act purely as an entropic barrier. b. And c. show variations on the selective phase model in which the hydrogel is nonsaturated and saturated, respectively. 62

4.2 **At the AWI, BG-BODIPY or 0.2µm fluoresbrite carboxylate YG beads colocalise with IAPP.** 3.6µM IAPP was incubated with 0.4µM bIAPP-0.08µM avidin D Texas red, and with 5.56µM BG-BODIPY (green fluorescence) (a) or 9.5±0.4x105 0.2µm green fluorescent beads (b) in PBS and H_2O in a well of a 96-well plate. Z-stacks that encompassed the AWI and an area spanning 1417x1417µm^2 were collected for at least 18 h. 3D projections were then visualised with the AWI at the front facing the experimentalist and the bulk solution behind it. Images are snapshots at various time points. The right hand side images are higher mag images of the inset areas at the 18 h time points. 65

4.3 **FLIM measurements of IAPP gelation.** a. FLIM images of the AWI region of a 4µM IAPP-5.56µM BG-BODIPY solution, in H_2O or D_2O, at 25°C and 5 or 21 h. Shown in each row are images of three independent replicates per incubation condition. The insets are zoomed in snapshots of the full FLIM images (with the brightness having been increased), which depict representative regions of the AWI that contain several fluorescence lifetime values. The lookup table shows the colour assigned for each fluorescence lifetime value, from red (short lifetime) to blue (long lifetime). b. Fluorescence lifetime histograms of BG-BODIPY in H_2O and D_2O at 5 and 21 hrs. 66

4.4 **BG-BODIPY targets to transiently expressed nup214.** Two airyscan images of BG-BODIPY labelling in HeLa cells expressing a nup214/SNAP-tag construct. The left hand image is a crosssection of the cell showing the punctate ring pattern typical of NPCs, as well as large cytoplasmic aggregates. The right hand image is a grazing section of the top of the nucleus, showing individual NPCs from above. 68

4.5 **FLIM of cells transiently expressing nup214/SNAP-tag.** a. A FLIM image of a crosssection of a HeLa cell showing the lifetime of BG-BODIPY targeted to nup214 in the NPC, as well as several cytoplasmic inclusions. b. A lifetime histogram of BG-BODIPY targeted to nup214 (peak value = 2287.2). 69

4.6 **Mitoxantrone reduces reported lifetime from within NPCs labelled with BG-BODIPY.** Regions of interest were drawn around the NEs of cells expressing nup214/SNAP-tag either treated with 10µM mitoxantrone or not, and the peak fluorescence was recorded. Mitoxantrone treatment resulted in a significant (p<0.001) decrease in the peak lifetime. 70

4.7 **Confirmation of the presence of SNAP-tag at the NPC in CRISPR'd cell lines through IF.** mab414 was labelled with donkey anti-mouse IgG Alexa Fluor 594, while anti-SNAP-tag was labelled with goat anit-rabbit IgG Alexa Fluor 488. There is clearly colocalisation with mab414 for all three CRISPR lines despite the high background, but there is very little colocalisation in wild type cells. 72

4.8 **HCT-116 cells expressing SNAP-tag at endogenous levels at different faces of the NPC have disparate average lifetimes.** ROIs were drawn around the NEs of cells expressing the SNAP-tag enzyme attached to either nup214, nup98, or nup153 and labelled with BG-BODIPY. The peak lifetime values of the histograms within these ROIs were then measured for individual cells of each line and plotted. We found there was a significant difference between nup214 and nup153 ($p = 0.0002$), and nup214 and nup98 ($p = 0.008$), but not nup98 and nup153. The schematic to the left shows the positions of the individual nups within the pore complex with the cytoplasm at the top and the nucleoplasm at the bottom. 74

4.9 **Mitoxantrone disrupts the selective permeability function of NPCs.** a. Timecourse of mCherry-NLS following treatment with 10µM mitoxantrone. The signal becomes increasingly diffuse and cytoplasmic as time passes. b. Ratio of nuclear to cytoplasmic mCherry signal at the beginning and ending time points in a. c. DMSO treatment of cells for the equivalent time does not result in leakage of mCherry from the nucleus. d. 24 hour treatment with Ac5SGlcNAc did not result in the breakdown of the selective permeability barrier as has been shown previously (see Section 4.2.8). 76

4.10 **Mitoxantrone reduces the viscosity within the NPC at nups 214, 98, and 153, while lipoamide does not.** The left hand column shows the comparative viscosity histograms for untreated cells and cells (n=∼20) treated with 10µM lipoamide for all three cell lines. The x-axis represents the viscosity in cP, while the y-axis is frequency in arbitrary units. The right hand column depicts the same control viscosities for each of the cell lines compared with the reported viscosity in cells treated with 10µM mitoxantrone. 77
4.11 **BG-BODIPY targeted to transiently expressed Importin5α reports similar lifetimes to those of the NPC.** A FLIM image and its lifetime histogram (peak at ∼2500ps) of BG-BODIPY targeted to Importin5α. 78

5.1 Tardigrade anatomy. Taken from Bespalova, 2019. 83
5.2 **BG-BODIPY staining of tardigrades.** Airyscan images of a. two frontal planes of a tardigrade showcasing staining of the midgut (mg), storage cells (sc), pharynx (p), feeding apparatus (fa), mouth (m), dorsal nerve ganglion (dg), claw glands (cg) and b. a sagittal plane section showing the ovary (ov) and salivary gland (sg). 86
5.3 **FLIM measurements of whole live tardigrades.** a. A frontal plane and two midsagittal plane FLIM images of three individual tardigrades with most of the major structures on view. b. Viscosity histogram of a whole tardigrade, with a peak at ∼180cP. c. A 3D projection of FLIM Z-stacks collected of a frontal plane of a tardigrade. All images are oriented such that the caudal end of the organism is to the left of the image. 87
5.4 **Comparative internal states of tardigrade tuns formed under different stress conditions.** a. FLIM images of tardigrade tuns formed in high humidity (slow drying) and low humidity (fast drying) conditions, in high humidty while treated with mitoxantrone, and during acute osmotic stress (see Section 5.2.5). b. A comparison of the viscosity (cP) histograms for tuns in each condition. 89

5.5 ***H. exemplaris* forms tuns in response to acute osmotic stress.** Tardigrades form tuns in response to acute osmotic stress from 90% PBS by 30 minutes and 3 hours in 20% PBS. In both conditions, when tuns were reintroduced to water, the organisms appeared to recover and regain motility. Images are examples, but all tuns ($n = 6$, $n = 4$) behaved uniformly. 91

5.6 **Desiccation of rotifers results in tuns with increased viscosity.** a. FLIM images of hydrated rotifers. In respones to chloroform, the rotifers retract, making it difficult to discern all of the anatomical features. The red spots in the right hand image are likely autofluorescence of bacteria in the gut. b. A FLIM image of a row of 6 rotifer tuns that had formed in a line agains the edge of a well. All tuns demonstrate a fairly uniform increase in lifetime, which, as can be seen in c., corresponds to a large upward shift in viscosity. 94

List of Abbreviations

AD - Alzheimer's disease

ADC - analogue-to-digital converter

ADR - adrenergic receptor

AGT - *O*6-alkyguanine-DNA alkyltransferase

ALS - amyotrophic lateral sclerosis

AWI - air-water interface

BCECF - 2,7-bis-carboxyethyl-5 (and 6)-carboxy-fluorescein

BG-BODIPY - benzylguanine-boron-dipyrrin

BODIPY - boron-dipyrrin

BSA - bovine serum albumin

CAHS - cytoplasmic abundant heat soluble

CFD - constant fraction discriminator

COX8 - cytochrom C-oxidase subunit 8

M-CSF - macrophge colony-stimulating factor

DMEM - Dulbecco's Modified Eagle's Medium

DMSO - dimethyl sulfoxide

DNA - deoxyribonucleic acid

DPH - 1,6-diphenyl-1,3,5-hexatriene

ECM - Extracellular Matrix

EDRF/NO - endothelium-derived relaxing factor/nitric oxide

ER - endoplasmic reticulum

FBS - fetal bovine serum

FLIM - fluorescence lifetime imaging microscopy

FSG - fish skin gelatin

FTD - frontotemporal dementia

FUS - fused in sarcoma

GUV - giant unilamellar vesicle

IAPP - islet amyloid precursor polypeptide

IDP - intrinsically disordered protein

IDR - intrinsically disordered region

IF - immunofluorescence

INM - inner nuclear membrane

IRF - instrument response function

LEA - late embryogenesis abundant

LLPS - liquid liquid phase separation

MAHS - mitochondrial abundant heat soluble

MDCK - Madin-Darby canine kidney

MSG - mature secretory granule

NE - nuclear envelope

NEAA - non-essential amino acids

NIDDM - non-insulin dependent diabetes mellitus type II

NLS - nuclear localisation signal

NPC - nuclear pore complex

NTF - nuclear transport factor

NTR - nuclear transport receptor

NUP - nucleoporin

ONM - outer nuclear membrane

PBS - phosphate buffered saline

PM - plasma membrane

PMT - photomultiplier tube

RBP - RNA binding protein

RNA - ribonucleic acid

ROI - region of interest

RRM - RNA-recognition motif

SAHS - secretory abundant heat soluble

SG - stress granule

SPT - single particle tracking

TAC - time-to-amplitude converter

TCPSC - time-correlated single photon counting

TDP-43 - TAR DNA-binding protein 43

TICT - twisted intramolecular charge transfer

TR-FA - time-resolved fluorescence anisotropy

TR-FAIM - time-resolved fluorescence anisotropy imaging microscopy

VSV - vesicular somatic virus

Chapter 1

Introduction

As our understanding of the complexity of and variation within the intracellular environment becomes more complete, it becomes increasingly clear that viscosity is a vital and understudied parameter in cell biology. Many molecules must diffuse across densely-packed cellular compartments to transduce signals within a given time-frame in order for cells to function properly, and the viscous environment they encounter will significantly impact on their ability to do so. As would be expected, perturbations in cellular viscosity that have a negative impact on cell function are associated with a variety of disease states.

For example, *E. coli* segregate aggregates of misfolded protein to the cell poles to minimise the amount of aggregated material in each daughter cell (Lindner *et al.*, 2008). However, in cells that are exposed to reduced temperatures or are plasmolysed, these aggregates no longer localise to the poles and accumulate in the midcell, resulting in an inability to create an asymmetrical distribution of aggregates in the sister cells, and therefore rejuvenate the cell line (Oliviera *et al.*, 2016). This failure was shown to be caused by the increase in cytoplasmic viscosity in both of these conditions.

In humans, changes in lipid viscosity have been shown to be associated with a variety of diseases. The membrane fluidity of platelets in individuals at risk of developing Alzheimer's disease (AD) (i.e. with a first degree relative with AD) was shown to be increased compared to the average (Zubenko *et al.*, 1999). Increasing the membrane cholesterol levels in endothelial cells progressively inactivates the activity of membrane-bound NO synthase, and reduced release of endothelium-derived relaxing factor/nitric oxide (EDRF/NO) is associated with atherosclerosis

(Deliconstantinos *et al.*, 1995). A similar finding in elderly rats showed that insulin receptor insensitivity was linked to increased membrane viscosity in liver cells, potentially due to the increased viscosity inhibiting the receptor aggregation required for proper signalling (Nadiv *et al.*, 1994).

It is possible that a raft of other diseases are associated with changes in microviscosity at other points within the cell. However, due to technological limitations I will outline below, it has hitherto been difficult to measure viscosity within living cells without causing major disruption to the cells. There is very much a need within the field for a means of measuring changes in viscosity in living cells that can be targeted to numerous subcellular locations through a universal mechanism. This thesis contains our efforts to develop a probe to fill such a niche.

1.1 Understanding microviscosity

Viscosity, as it is understood on a macro-scale, is defined as the resistance of a liquid or gas to flow. This property is mediated by the internal friction of the molecules within the fluid – the higher the frictional forces, the more resistant the fluid is to flow. This resistance applies both to objects moving through a fluid and to the motion of layers of the fluid itself. For example, if a plate of area, A, is moved with a velocity, $\mathbf{v}$, parallel to the surface of a liquid it is covering, then a force of F will be applied to the liquid. The shear stress, τ, is then defined as $\tau = F/A$. However, the velocity of the layers of the liquid as a response to the application of the shear force decreases with further distance, y, from the plate. Viscosity can therefore be understood as a proportionality constant, η, in relation to shear stress and the local shear velocity at a point y away from the plate $\frac{\partial v}{\partial y}$ or Equation 1.1,

$$\tau = \eta \frac{\partial v}{\partial y} \tag{1.1}$$

This viscosity is referred to as 'dynamic', or 'absolute', viscosity, which is an average property of the molecular interactions of a given fluid. Traditionally, viscosity has been measured with devices such as Zahn cups or capillary viscometers, which apply a physical constraint on the flow of the liquid to infer its viscosity, or falling sphere viscometers that measure the speed with which a sphere of a known density is dropped into the liquid and the time it takes for it to reach a specified point is recorded. These techniques are unsuited to the task of measuring viscosity on the cellular level due to their mechanisms of action, which require large volumes

of sample fluid, report only a spatially and temporally averaged viscosity across the system, and would require the cells to be homogenised.

Further, as one approaches the level of the molecule, absolute viscosity begins to break down as a useful concept. The cell is an exceptionally complex environment; highly disparate cellular processes often occur in the same cellular milieu. The cytoplasm is a highly crowded environment with an estimated 400mg of proteins, lipids, nucleic acids, etc. in each ml (Fulton, 1982). On the microscale, the homogeneity of a liquid can no longer be assumed. A spherical molecule's translational diffusion through the cytoplasm is impacted by the heterogeneous organisation of the solvent molecules. The sphere can diffuse through two mechanisms: Stokes' diffusion, a viscous process in which the molecule pushes solvent molecules out of its path, or free volume diffusion, in which the sphere occupies the free volume gaps between the solvent molecules (Valeur, 2001). The molecule's diffusion will also be greatly impacted by its size, charge interactions, and hydrogen bonding properties, and polarity.

The microviscous environment, then, cannot be gleaned from the viscous properties of the bulk fluid. In order to measure microviscosity, one must then attempt to measure the sum of the forces affecting the resistance to flow of individual molecules rather than the bulk fluid. Thus, in order to make measurements of microviscosity, the sensor should be on the order of a molecule. Fluorescent techniques lend themselves particularly well to measuring microviscosity, and I shall outline some of the methods that have utilised fluorescent probes below.

1.2 Methods for measuring viscosity

1.2.1 Single particle tracking

Single particle tracking (SPT) dates back to the 1980s, when it was demonstrated that colloidal gold particles could be rigidly attached to biomolecules and imaged on the surface of living cells (Geerts *et al.*, 1987; Brabander *et al.*, 1988). The large Rayleigh intensity scattering of these particles meant that the centre of the particles' positions could be tracked within nanometres using differential interference contrast microscopy, allowing for the first time the tracking of molecules *in vivo* with a high level of precision.

Since then, numerous probes have been developed for use with SPT, and the algorithms for calculating movement of the particles have evolved considerably. The probes can be roughly divided into two classes: strong scatterers such as gold particles and latex beads, and fluorescent probes such as fluorescent molecules, gene-encodable fluorescent molecules, and quantum dots. As is the case with most scientific techniques, there is a tradeoff between these two classes of probes. The ability of the former to scatter light is positively correlated with the size of the particle, meaning that probes on the order of 20-100 nm in diameter are required (Levi *et al.*, 2005), meaning the probe could easily be many times larger than the target molecule. This means that the particle will significantly impact the movement of the molecule, introducing artefacts. However, these probes are incredibly stable, and can be tracked over long periods.

Quantum dots, by contrast, are only 5-10 nm, but their blinking behaviour and problems with labelling makes SPT difficult. Fluorescent molecules are even smaller, and gene-encodable fluorescent molecules benefit from being expressed with the protein of interest, eliminating labelling issues. The catch is, these molecules cannot be tracked for long periods due to fluorescence bleaching.

Because of the above, SPT is a very limited means of measuring viscosity in cellular compartments. Kalwarczyk *et al.* (2011) found that as probes varied in size, they reported different viscosities within the cytoplasm, highlighting the technique's susceptibility to artefacts. That being said, SPT has been employed to estimate the cytoplasmic viscosities in mammalian cells and *Xenopus* oocytes (Kalwarczyk *et al.*, 2011; Tseng *et al.*, 2002; Selvaggi *et al.*, 2010), as well as to measure the motion of phagosomes carrying phagocytosed beads through the cytoplasm in fibroblasts (Levi *et al.*, 2005). SPT was also used to measure movements of lipid molecules in the plane of the cell membrane, leading to identification of high viscosity regions that have come to be known as the highly contentious 'lipid rafts' (Fujiwara *et al.*, 2002; Murase *et al.*, 2004).

1.2.2 Fluorescence anisotropy

Fluorescence anisotropy is a technique that relies on polarised light and a class of anisotropy fluorophores that are only excited by incident light that is parallel to the fluorophore's excitation dipole and solely emit in that same plane (Theodorakis & Haidekker, 2007). During the fluorescence lifetime, between excitation and emission, the molecule is able to rotate and tumble, which results in depolarisation

of the emitted light. This rotation of the molecule is dependent on the viscous environment of the probe. Higher viscosity prevents movement of the fluorophore, preserving the high anisotropy of the resultant fluorescence; low viscosity environments lead to increased fluorophore rotation and therefore lower anisotropy.

Steady state fluorescence anisotropy has been used to study viscosity on the cellular level in a number of contexts. Dix and Verkman (1990) were able to demonstrate entry of 2,7-bis-carboxyethyl-5 (and 6)-carboxy-fluorescein (BCECF) into the cytoplasm of Madin-Darby canine kidney (MDCK) cells and Swiss 3T3 fibroblasts and measure the viscosity - (around 13cP for both cell lines). Dombek and Ingram (1984) were able to measure the impact of ethanol on the viscosity gradient across *E. coli* plasma membrane. 1,6-diphenyl-1,3,5-hexatriene (DPH), one of the most popular anisotropy probes, was employed to measure decreased microviscosity within the membranes of rabbit polymorphonuclear leukocytes during phagocytosis (Berlin & Ferra, 1977).

The main limitation of steady state anisotropy measurements is that it is impossible to delineate between real high-viscosity environments and signal from probe that is limited in motion because it is bound to protein. Time-resolved fluorescence anisotropy is able to overcome this by using a pulsed polarised light source and collecting information about the lifetime of the polarised fluorescence emission. This additional information allows for the identification of the proportion of high anisotropy that is contributed by bound probe, as this will have a constant, long lifetime compared to the variable lifetimes of the unbound fraction. The Dix and Verkman (1990) paper cited above used TR-FA to differentiate between the fraction of BCECF free in the cytoplasm, and that which was trapped beneath tight junctions.

When combined with a microscope, the technique is referred to as time-resolved fluorescence anisotropy imaging microscopy (TR-FAIM). This technique is able to produce an image where each pixel's intensity is an average of the fluorescence anisotropy decay, giving a spatial representation of a sample's response to a pulsed polarised light source. This is useful for applying the anisotropy measurements to the cell, and TR-FAIM has indeed been used to measure microviscosity in living cells (Parker *et al.*, 2010), although it still suffers from photobleaching, and requires very specialised equipment, including polarisation preserving light paths for the laser pulses.

1.2.3 Molecular rotors

All molecular rotors operate through the same basic mechanism: competition between two photon emission pathways, fluorescence and a non-radiative decay that is achieved through intramolecular rotation (and therefore lowers the excitation state without emitting a photon). Any increase in surrounding viscosity interferes with the rotor's ability to rotate, which causes the decay to favour the radiative pathway and, thus, fluorescence. The largest class of these fluorophores are the Twisted Intramolecular Charge Transfer (TICT) molecular rotors (Haidekker & Theodorakis, 2007). These molecules have been studied for decades, and Förster and Hoffman characterised the power-law relationship of quantum yield and viscosity in the eponymous Equation 1.2

$$\Phi_f = Z\eta^{\alpha} \tag{1.2}$$

where Z and α are constants and Φ_f is the fluorescence quantum yield. The fluorescent quantum yield, and the other main parameter of fluorescence, the fluorescence lifetime, are defined by Equation 1.3

$$\Phi_f = \frac{k_r}{k_r + k_{nr}} = k_r \tau_f \tag{1.3}$$

where k_r and k_{nr} are the radiative and non-radiative decay constants, respectively. It follows that a plot of $\log \Phi_f$ against $\log \eta$ yields a straight line with slope α. Depending on how the power law relationship is derived, α can have a value of 2/3 or somewhere between 1/3 and 2/3 (Kuimova, 2012). Molecular rotors benefit further from being able to be used irrespective of the polarity of the solvent, as quantum yield and fluorescence lifetime are affected by viscosity, but polarity changes cause a shift in the peak emission wavelength (Haidekker & Theodorakis, 2007).

Whilst numerous molecular rotors of various chemical structures have been developed (Table 1.1), they all share the same general structure, comprising an electron donating subunit and an accepting subunit, separated by a spacer unit (Haidekker & Theodorakis, 2010). So long as the transfer of charge between the nitrogen electron donor and the nitrile electron acceptor in the core structure is not affected, a large range of modifications can be made to the rotor without affecting its viscosity reporting ability (Haidekker & Theodorakis, 2007). This modularity can be exploited to attach various functional groups or targeting/recognition elements to a molecular rotor to alter its sub-cellular localisation, or to alter the fluorescent properties of the dye.

Group	Benzonitrile-based flourophores	Benzylidene malonor
Representative molecule	DMABN	DCVJ
Peak excitation (approx.)	290 nm	489 nm
Peak emission (LE, TICT) (approx.)	342 nm, 460 nm	505 nm
Reference	Atsbeha *et al.*, 2010	Haidekker *et al.*, 2001

Table 1.1: Typical molecular rotors of various classes and their properties. (Adapted from Haidekker & Theodorakis, 2010)

1.2.3.1 Lifetime-based rotors

As the fluorescence intensity depends greatly on the concentration of the molecular rotor, it is therefore often more useful to measure the fluorescence lifetime of the molecules. This too can be used to determine viscosity, as can be seen by substituting Φ_f from Equation 1.2 for τ_f in Equation 1.3 to yield Equation 1.4:

$$\tau_f = \frac{Z\eta^{\alpha}}{k_r} \tag{1.4}$$

and Equation 1.5

$$\log \tau_f = \log \frac{Z}{k_r} + \alpha \log \eta \tag{1.5}$$

With the resultant equation, one can see that plotting $\log \tau_f$ against $\log \eta$ should also give a straight line with a slope of the same α value as for quantum yield as a function of viscosity (Kuimova, 2012). This second relationship is vital for avoiding concentration uncertainty and is the underpinning of fluorescent lifetime imaging microscopy (FLIM), a powerful technique for imaging fluorescence decays across a pixelated field using either time- or frequency-domain measurements.

The first such probe was developed by Kuimova *et al.* (2008), and was composed of a BODIPY-based fluor attached to a hydrophobic fatty acyl chain that incorporated the molecule into the plasma membrane (Kuimova *et al.* 2008; Levitt *et al.*, 2009), and was used to measure viscosity throughout SK-OV-3 cells. This probe has been utilised by numerous groups for a variety of purposes, including measuring the viscosity in lipid-ordered and lipid-disordered domains of giant unilamellar vesicles (GUVs) (Wu *et al.*, 2013; Dent at al, 2015); measuring the microviscosity of aerosol particles in response to humidity changes, hydration, and chemical ageing (Hosny *et al.*, 2013; Hosny *et al.*, 2016); measuring sol-gel transitions (Hungerford *et al.*, 2009); and mapping the viscosity within different layers of *Bacillus* spores (Loison *et al.*, 2013).

Other BODIPY-based probes have been developed, such as one for lysosomal targeting through the attachment of a morpholine group (Wang *et al.*, 2013), and another that can measure both viscosity and polarity due to the presence of a Nile Red moiety separated from the BODIPY by a linker (Yang *et al.*, 2014). A number of BODIPY-based probes have been developed for targeting to the mitochondria, with one that had a triphenylphosphonium moiety for targeting, used to make FLIM measurements of the viscosity within the organelle (Su *et al.*, 2016).

Non-BODIPY-based lifetime molecular rotors include Cy3, which has also has been used to measure viscosity in aerosols (Hosny *et al.*, 2013; Hosny *et al.*, 2016). Another Cy3 probe was developed with the presence of a trimethoprim group, allowing it to be targeted to any protein of interest that is expressed with *E. coli* dihydrofolate reductase (eDHFR) (Gallagher *et al.*, 2010).

1.2.3.2 Ratiometric motors

Because of concentration effects, molecular rotors need to be measured in the lifetime domain, which can be a restrictive requirement for groups without access to a FLIM measurement. To circumvent this, molecular rotors can be used in combination with another fluorophore that does not respond to viscosity to make ratiometric measurements. Luby-Phelps *et al.* used the cyanine dyes Cy3 and Cy5 attached to Ficoll70, the former of which is viscosity sensitive while the latter is insensitive, to make ratiometric measurements in living cells (Luby-Phelps *et al.*, 1993). This study simply injected the two dyes within cells and assumed they would label all regions equally, which is far less desirable than having two fluors bound to one another to ensure 1:1 labelling.

Haidekker and colleagues managed to overcome this by putting both the viscosity-independent and -dependent fluors in a single molecule (Haidekker *et al.*, 2006). In this system, the insensitive fluorescent unit acted as a donor for resonance energy transfer to the dependent fluorescent unit, the quantum yield of which varied with viscosity. Similar probes were produced by Yoon *et al.* and were employed to measure changes in lipid vesicle membrane viscosity in response to propanol treatment (Yoon *et al.*, 2011). A carbazole-based cyanine derivative Caz-Cy2, made from conjugating a Caz moiety with Semi-Cy2, was used to measure mitochondrial viscosity in HeLa cells (Liu *et al.* 2012).

In contrast, the Kuimova group has been developing an interesting class of fluorophore that can be used for ratiometric measurements without the requirement

of a second fluor. This can be achieved by using porphyrin dimers which have two peaks in its fluorescence emission spectra, the relative intensity of which change depending on the viscous environment (Kuimova *et al.*, 2009; Vyšniauskas *et al.*, 2017). They utilised this probe to watch increases in viscosity during cell death (Kuimova *et al.*, 2009).

1.3 Time-correlated single photon counting

How then does one measure the fluorescence lifetime of a probe in a biological system? This can be achieved in three main ways: in the frequency domain by phase modulation of excitation intensity in relation to acquisition sensitivity, in the time domain either by using a pulsed light source in conjunction with a time-gated CCD camera to construct images from selected emission time bins, or by the use of time-correlated single photon counting detectors. Time-correlated single-photon counting (TCSPC) is typically employed to this end, and relies on the detection of single photons emitted from fluorophores excited by a pulsed laser source with a known pulse frequency. The chances of detecting multiple photons within the signal period following a low intensity, and therefore the detection of the first single photons arriving at the detector source, can be built up to create a photon distribution over time (Figure 1.1). This represents the 'waveform' of the optical output, which does not actually exist, but in reality represents a photon probability distribution assessed from the photon output after many pulses.

In a traditional TCPSC set up, the pulse from the fluorescent molecule (representing the 'start' pulse) from the photomultiplier tube (PMT) and a pulse from a reference pulsed light source (the 'stop' pulse) enter the 'Constant Fraction Discriminator' (CFD), which triggers the rest of the circuit. Simple thresholding of the incoming signals cannot be used, as both the PMT signal and that of the reference photodiode will vary in amplitude and would lead to a timing jitter. CFD avoids this by delaying the second reference pulse, inverting it, and combining it to take the 'zero cross point', which is independent of amplitude (Figure 1.2). This configuration in which the PMT signal starts the CFD and the reference pulse stops it is called a 'reverse' mode. In the other configuration, where the reference pulse switches on the CFD, there will be numerous occasions for which no photon arrives to switch it off, and the TAC has to reset and discharge the voltage, which

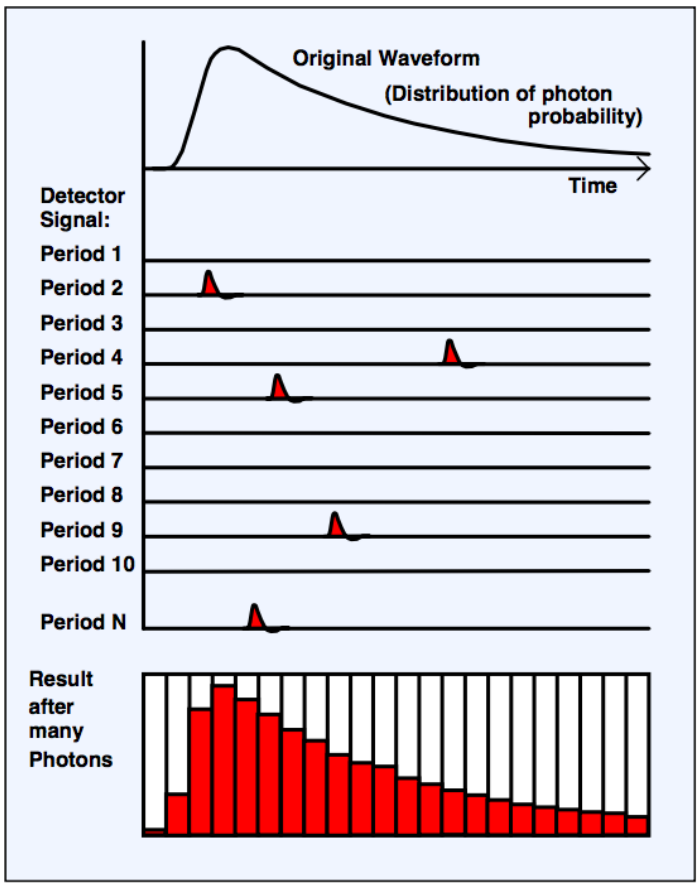

Figure 1.1: **The Principle of TCPSC.** The waveform of optical output is extrapolated from a histogram with many even time bins, which builds up as numerous photons hit the detector at various time points after each pulse. Reproduced from B&H TCSPC handbook (Becker, 2015).

will result in dead time (during which no measurement can be made). Operating in the reverse mode eliminates this problem, as the reference pulse will arrive irrespective of whether the TAC has been switched on.

These pulses, upon triggering the CFD, are passed on to a time-to-amplitude converter (TAC), which is responsible for creating a signal that is proportional to the time between the start and stop pulses. Usually this is achieved with a switched current source that charges a capacitor, with the start pulse switching on the current and the stop pulse terminating it. Assuming the current charging the capacitor is constant, then the resulting voltage in the capacitor is proportional to the timing differences between the two pulses. Time differences within a few ps can be detected in this manner.

The voltage produced from TAC is then passed on to a biased amplifier (AMP)

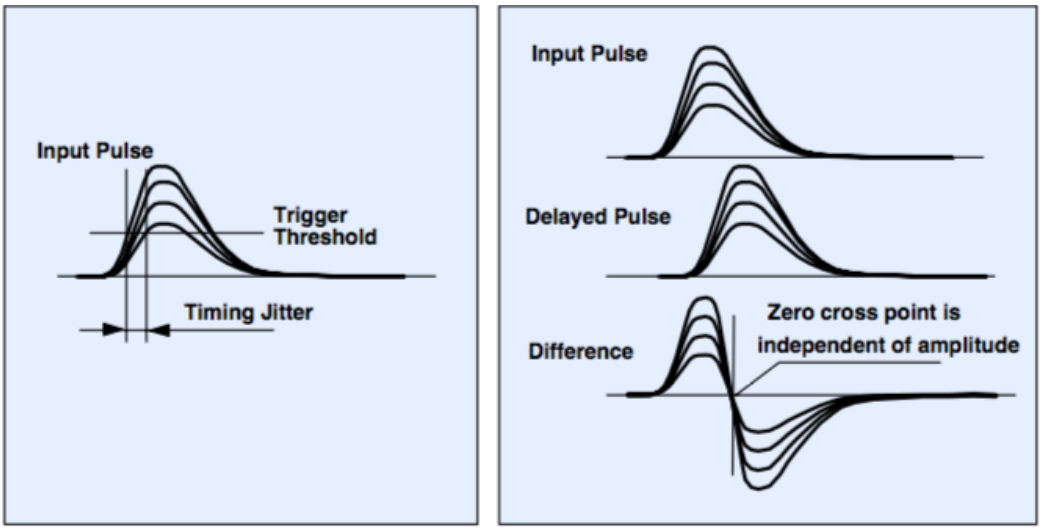

Figure 1.2: **The principle of CFD.** The deleterious contribution of timing jitter is demonstrated on the left. The right shows how the zero cross point of the input and delayed pulses is independent of amplitude. Reproduced from B&H TCSPC handbook (Becker, 2015).

with variable gain and offset and determines whether the signal is within the expected limits. The amplified signal then goes to an analogue-to-digital converter (ADC). The ADC converts the amplified signal into a digital memory address for an appropriate time bin. It is vital that all of these time bins be of equal width to avoid any distortion in the histogram.

This process occurs again and again for numerous pulse events until a histogram of sufficient photon count has been produced. Note that this method sets an upper bound on the emission photon flux that can be accurately measured, since it relies on the assumption that there will be a maximum of one photon per pixel per excitation pulse, so measuring the first arrival time will be representative of all emission behaviour. Adjusting the excitation laser pulse frequency can facilitate longer lifetime measurements, but the limit of single photon counting at the detector still applies.

1.4 Fluorescence lifetime imaging microscopy

Fluorescence lifetime imaging microscopy (FLIM) is a powerful technique that combines elements of TCSPC with conventional laser-scanning confocal microscopy in order to build up images encoded with fluorescence lifetime information. In FLIM, the TCSPC module receives not only the information about the time of the

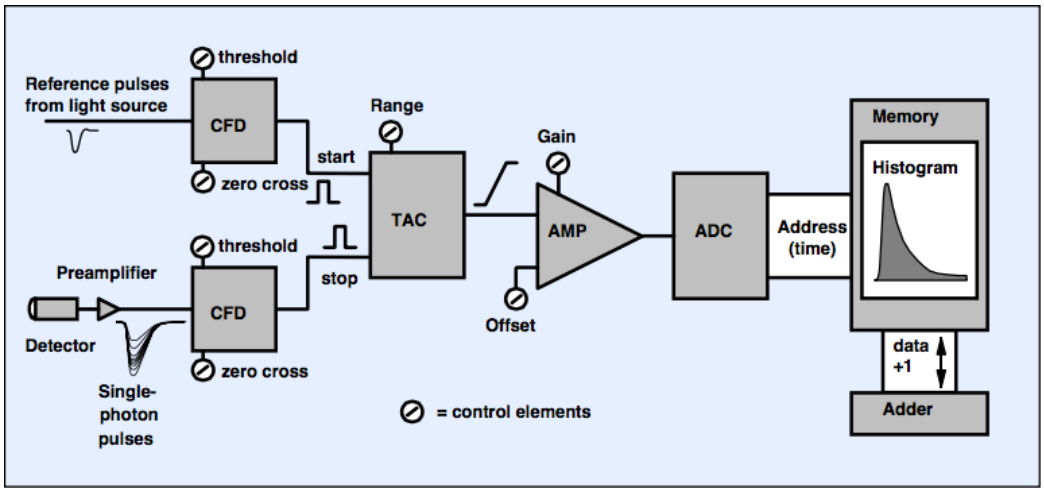

Figure 1.3: **Architecture of a classic TCSPC device.** Reproduced from Becker (2015).

photon arrival, but also the scan clock signals from the scan controller of the confocal (pixel, line, and frame clock), and synchronously, a scanning interface that counts the X and Y positions of the incoming photon.

Because of this, the memory builds up a distribution of the time and positional coordinates for each pulse, and the resultant data is the formation of a 2D image for which each pixel contains the fluorescence decay lifetime information. In other words, FLIM produces a heat map of the area being scanned, in which the values represent the lifetime histogram in that pixel. This does not require that the laser stay on each pixel for long enough to build up a histogram, rather the total acquisition time for each pixel over numerous successive scans is sufficient for histogram production.

Updates in FLIM technology have enabled one to now perform a variety of additional FLIM techniques – including mosaic FLIM in order to stitch together a larger scan area, Z-stack FLIM to build up a 3D image containing lifetime information, and temporal mosaic FLIM to measure changes in lifetime over increments of time.

Equally important as the instrumentation is the exponential decay analysis used for determining the lifetime for each pixel, as incorrect analysis can lead to false lifetime values. The difficulty of exponential decay analysis is compounded when multi-exponential decays are present. Being an experimental technique run in the real world and not just in theory, a vital part of calculating an appropriate lifetime is the determination of the instrument response function (IRF); the IRF width in-

dicates the temporal resolution of the system, limited by the timing error of the detectors and the non-zero width of the laser pulses. Timing error of the detectors occurs due to the variation in the trajectories of the photoelectrons within the PMT, with different trajectories leading to differences in travel time in a process known as 'transit spread time'.

In the Becker & Hickl SPCImage software, the IRF is automatically calculated from the raw data when it is loaded into the software. This automatic process assumes the IRF has a short width compared with the fluorescence lifetime, such that the rising edge of the fluorescence signal is close to the integral of the IRF. Therefore the IRF(t) is calculated as the differentiated function, d rise(t) / dt. The assumptions used for the automatic calculation of the IRF do not always hold true, in which case the IRF can be acquired manually. Whilst we did manually check the IRF at the beginning of this project, all FLIM analysis within this thesis relied on the automatic IRF calculation within the software.

FLIM, then, presents the perfect opportunity for measuring viscosity in biological systems. Increasingly we are realising that cells use phase transitions for a range of functions, sequestering certain molecules and proteins to protect them or to facilitate their interaction. In the following sections, I will outline some of the ways biological systems employ one such phase, hydrogels, for physiological purposes, and the role of hydrogels in pathological conditions. I hope these examples illustrate the manifold applications for a means of measuring microviscous environments in living cells with molecular rotors.

1.5 Biological hydrogels

Hydrogels are three-dimensional, cross-linked polymeric networks dispersed in water. The spaces in between the polymer chains are filled with water molecules, and the polymer chains constrain the water and maintain the gel shape whilst allowing passive diffusion of molecules depending on the pore size. The water content endows the hydrogel with its degree of flexibility. Both naturally occurring and synthetic polymers form hydrogels. The first synthetic hydrogel, crosslinked hydroxyethyl methacrylate, was developed half a century ago, spawning a sustained interest in the development of these gels for the biomedical applications such as drug delivery and regenerative medicine (Zhu & Marchant, 2014; Trappmann *et al.*, 2012; Deng *et al.*, 2010; Black *et al.*, 2015; Lei *et al.*, 2011; Ifkovitz

et al., 2010). However, given their biocompatibility and lack of immunogenicity, polypeptide based hydrogels have become preferred for this field (Peréz *et al.*, 2014).

Although not being universal as some amyloid polypeptides simply precipitate from solution, hydrogel formation has also been reported for a variety of amyloid forming polypeptides, both functional and disease associated (Rijkers *et al.*, 2002; Buell, 2014; Murakami *et al.*, 2015; Kato, 2012; Krysmann, 2008; Manno, 2010; Jean *et al.*, 2016; Cox, 2007; Bolisetty *et al.*, 2012; Yang *et al.*, 2012; Lepère, 2007; Lakshmanan *et al.*, 2013).

Gelation is the phase transition of polymers from liquid phase to gel. Here we do not refer as a gel a solute simply coming out of solution and precipitating. Traditionally, gels are defined as solid and fluid three-dimensional dilute cross-linked systems, which form networks and behave like solids due to the network inhibiting flow at steady-state (Ferry, 1980). Gels can exhibit a range of properties, from being weak to hard, and can expand in any fluid (e.g., water and oil). Gels with water as the dispersion medium are called hydrogels (Ferry, 1980; Chirani *et al.*, 2015). Although over the years, hydrogels have been defined in many ways, one of the common definitions is that water-swollen gels consisting of a cross-linked polymeric network originating from monomer polymerisation that would not dissolve in water, are called hydrogels (Ferry, 1980; Chirani *et al.*, 2015; Ahmed *et al.*, 2015). The voids between the polymer chains are filled with water and the polymer network holds the liquid together, while allowing free diffusion of solutes/molecules with various diffusion constants according to their size and shape. Hydrogel density is approximately that of water as they are highly hydrated and adsorbent polymeric networks (the mass fraction of water is greater than that of the polymer). This high water content confers them a high degree of flexibility and viscoelasticity. Macroscopically, hydrogels behave as a solid and microscopically as a liquid.

Hydrogel mechanical strength and physical integrity are provided by cross-linking, either physical or chemical (Zhu & Marchant, 2014). Physical hydrogels are cross-linked by cooperative, weak and reversible molecular interactions (e.g., hydrogen bonds and/or polymer entanglement), whereas chemical hydrogels use irreversible and stronger covalent bonds. In physical hydrogels, the nature of the cross-linking can create clusters or domains and consequently heterogeneity. Many physical hydrogels become fluid when agitated, but re-solidify when resting (i.e.,

they can 'heal' if they get broken as the non-covalent cross-linking breaks and reforms) (Winter & Mours, 1997). Any changes in cross-linking can alter the hydrogel mechanical properties, e.g., stiffness. Physical gelation implies connections between polymers, through physical mechanisms, to form large scale structures and this can be achieved in different ways: loss of polymer chain flexibility near glass transition temperature (i.e., the atoms or molecular conformations freeze in and arrest molecular motions), loss of molecular mobility for liquid crystalline polymers at their nematic to smectic transition, and polymer aggregation into sample spanning complexes (Winter & Mours, 1997).

Preceding hydrogelation, depending on the polymer concentration and solvent composition, liquid-liquid phase separation (LLPS) can occur. During LLPS, a homogenous polypeptide solution separates into a polypeptide-rich phase (also called droplets), formed through weak polypeptide-polypeptide interactions creating a network, and a dilute polypeptide-poor phase (Pappu *et al.*, 2008). The liquid droplets have a higher density than the solution. With time, droplets grow by stochastically coalescing together until the solution reaches equilibrium. In some cases of LLPS, the droplets percolate the whole system, leading to transition to a gel phase. Recently, a great deal of attention has been given to polypeptide LLPS as this process has been demonstrated to play a crucial role in the formation and maintenance of cellular membrane-less organelles (see Section 3.2.11). Indeed, studies of fused in sarcoma (FUS) demonstrated that its mutated low complexity region mediates a concentration-dependent LLPS leading to hydrogelation, with the hydrogel composed of polymerised amyloid-like fibrils (Kato *et al.*, 2012, Patel *et al.*, 2015). Similarly, it has been shown in vitro that the Phenylalanine-Glycine (FG) repeats of nucleoporins, forming the central channel of nuclear pore complexes, phase transition from liquid to hydrogel via amyloid-like interactions (see Chapter 4) (Frey & Görlich, 2007; Ader *et al.*, 2010). Thus, it is clear that a relationship between LLPS and hydrogelation, but also between LLPS and amyloid-like structure formation, exists. As for pathological amyloids, LLPS has been proposed to explain the hydrogelation heterogeneity of islet amyloid polypeptide, and aggregation into pathological amyloids of low-complexity polyglutamine tracts (as found in huntingtin protein involved in Huntington's disease) is thought to occur by LLPS (Jean *et al.*, 2016; Crick *et al.*, 2013).

1.5.1 Physiological hydrogels

1.5.1.1 Bacterial biofilms

In addition to the motile, planktonic state, bacteria are also capable of adhering to numerous surfaces they encounter in their aqueous environments, including teeth, industrial pipework, ships, and medical implants, to form sessile biofilms. The formation of these biofilms is a multi-stage process involving loose association between the surface and the bacteria's glycocalyx, followed by adhesion and the formation of aggregated microcolonies, and finally the development of these colonies into mature biofilms (Hall-Stoodley *et al.*, 2004; Costerton *et al.*, 1987). Biofilms are thought to confer numerous benefits on bacterial populations, including providing an environment suitable for complex signalling, differentiation of subpopulations for the division of labour of energetically taxing activities and the pooling of nutrients (Baty *et al.*, 2000; Stoodley *et al.*, 2010). Furthermore, biofilms are thought to provide protection from a raft of environmental hazards including ultraviolet exposure, desiccation, metal toxicity, and exposure to some antibiotics and antimicrobial agents (Espeland & Wetzel, 2001; Le Magrex-Debar *et al.*, 2000; Teitzel & Parsek, 2003; Fux *et al.*, 2005).

The extracellular polymeric substance that enmeshes bacteria in a biofilm has been subjected to rheological measurements demonstrating that biofilms exhibit the classic viscoelastic behaviour of a hydrogel (Klapper *et al.* 2002; Körstgens *et al.*, 2001; Towler *et al.*, 2010). The properties of a hydrogel are thought to confer many of the advantages of the sessile state. Most obviously, the viscoelastic properties of a hydrogel provide bacteria within the biofilm with a degree of protection from the rapidly changing current conditions they may experience in aqueous environments (Peterson *et al.*, 2015). Moreover, molecules experience a retarded diffusive motion in hydrogels compared to water, allowing for the concentration and retention of nutrients proximal to the cells (Lieleg *et al.*, 2011; Baty *et al.*, 2000). Beyond entrapping nutrients, the hydrogel is capable of blocking diffusion into the biofilm of other molecules through charge exclusion. Positively charged molecules, such as aminoglycoside antibiotics, show reduced diffusion through biofilms compared to neutral solutes, thought to be a product of the repulsive force produced by the negatively charged biofilm biopolymers, particularly the exopolysaccharides (Lieleg *et al.*, 2011; Shigeta *et al.*, 1997; Walters *et al.*, 2003).

1.5.1.2 Hydrophobins

Hydrophobins are a class of amphiphilic, low molecular weight proteins secreted by filamentous fungi, which have the ability to self-assemble into monolayers at hydrophobic-hydrophilic interfaces (Linder, 2009). Despite lacking sequence similarity, except for eight cysteine residues that form four disulphide bridges, these proteins form a common β-structured core which is involved in surface adhesion and self-assembly (Kwan *et al.*, 2006; Wang *et al.*, 2004).

Hydrophobins are separated into two classes. Class I hydrophobins are characterised by the formation of fibrillar 'rodlets', which requires a structural rearrangement, and can form membranes that are highly insoluble, requiring harsh acid treatments to be dissociated (Bayry *et al.*, 2012). The rodlets of SC3 and other class I hydrophobins are considered amyloid-like as they bind Congo Red and thioflavin T, and show an amyloid cross-β sheet structure (Mackay *et al.*, 2001; Butko *et al.*, 2001; Butko, Goodwin *et al.*, 2001; Wosten & de Vocht, 2000). The amyloid-like fibrils of SC3 form a semi-permeable protein film with a diffusion cut-off of 200 Da, which, in nature, would allow translocation of amino acids, a few fatty acids and monosaccharides, but not of oligomers of nucleic acids (Zampieri *et al.*, 2010). Class II hydrophobins, on the other hand, do not form such rodlet structures and can be dissociated with either ethanol, cooling, or the application of pressure (Wosten, 2001). The monolayers formed by hydrophobin self-assembly are not strictly speaking hydrogels, but one could imagine that this process represents the first stage in a hydrophobic–hydrophilic interface mediated gelation that subsequently extends into a third dimension, such as with IAPP (see Section 5.2.1).

The function that hydrophobins fulfil for filamentous fungi is directly related to their surfactant ability; they are some of the most surface-active molecules known (Wosten, 2001). The monolayer formation results in a lowered surface tension allowing the hyphae of fungi in aqueous environments to break through the air-water interface and produce aerial spore-laden conidiophore structures (Wang *et al.*, 2004). Moreover, the spores produced are coated in a layer of rodlet filaments, which are thought to convey protection from water by acting as a hydrophobic shield. In some species this layer is further covered in an ECM that facilitates binding of the spores to their host (Latge *et al.*, 1986). As with silk proteins, efforts have been made to utilise hydrophobins in drug delivery. Both foams and emulsions of hydrophobins have been used to envelop hydrophobic therapeutic

molecules, and it does appear that this coating confers protection from degradation (Valo *et al.*, 2010). This is attractive as a means of delivering therapies with slow release, as the hydrophobin coating would break down over longer periods.

1.5.2 Pathological amyloid hydrogels

1.5.2.1 IAPP and type II diabetes mellitus

Over 95% of cases of Type II Diabetes Mellitus are marked by the loss of pancreatic β-cells and the concurrent accumulation of amyloid aggregates of the 37aa peptide IAPP (Islet Amyloid Precursor Polypeptide; Abedini *et al.*, 2013). IAPP is usually co-expressed and secreted with insulin from β-cells, and the loss of these cells is correlated with the inability to maintain appropriate insulin levels in disease conditions (Westermark *et al.*, 1987; Clark & Nilsson, 2004). It has long been known that full-length and fragments of IAPP (aa20–29) have the ability to form hydrogels *in vitro* (Westermark *et al.*, 1990; Charge *et al.*, 1995) however it was only recently that our lab group characterised these gels both in the bulk and at the air water interface (AWI) (Jean *et al.*, 2016).

These 3D hydrogels were determined to comprise supramolecular fibrillar network and possessed classical viscoelastic properties with a storage modulus of 3.6 Pa for a 4 μM solution (Jean *et al.*, 2016). The gelation kinetics were complex, with two distinct kinetic regimes, one of which could be abolished in the presence of D_2O, showing the importance of solvation in this process. The presence of phospholipids accelerated this process, demonstrating that hydrophobic-hydrophilic interfaces, such as the cell membrane, could be catalysts for this kind of gelation.

A cytotoxic IAPP-derived hexapeptide (NFGAIL) was shown in another study to undergo hydrogelation with some phase separation of fibrils from the aqueous phase (Lakshmanan *et al.*, 2013). The gel formed in this experimental set up is obviously not physiological, but it is interesting that this behaviour is conserved in such a small fragment. The hexa-peptide adopted an α-helical conformation before entering the β-sheet organisation typical of amyloids.

1.5.2.2 Amyotrophic lateral sclerosis and frontotemporal dementia

There is increasing evidence linking diseases and dysfunction of RBPs. A range of RBPs form fibrillar cytoplasmic and nuclear deposits in neurons that characterise

neurodegenerative diseases, such as amyotrophic lateral sclerosis (ALS) and frontotemporal dementia (FTD) (Li *et al.*, 2013). Indeed, hnRNPA1 and TDP-43, along with FUS, hnRNPA2B, and TIA1, all have been identified to have mutations that drive inherited forms of neurodegenerative diseases by increasing the aggregation tendency (Li *et al.*, 2013; Johnson *et al.*, 2009; Kwiatowski *et al.*, 2009; Kim *et al.*, 2013; Hackman *et al.*, 2012). The two most well-characterised proteins associated with ALS and FTD are TDP-43 and FUS, two nuclear proteins that form cytoplasmic inclusions in disease states (though notably these inclusions are exclusive for one or the other protein) (Li *et al.*, 2013; Vance *et al.*, 2013; Vance *et al.* 2009). It has been proposed that formation of these pathological inclusions is driven by the failure of stress granules to disassemble and that pathology-associated mutant proteins interfere with normal stress granule dynamics. TDP-43 and FUS are normally involved in various aspects of mRNA metabolism and stress granule dynamics, and both contain prion-like domains at their C- and N-termini respectively (Cushman *et al.* 2010). Mutations within these domains are associated with disease states (Johnson *et al.*, 2009).

TDP-43 has been found to be a major component of ALS and FTD pathological inclusions (Arai *et al.*, 2006; Neumann *et al.*, 2006). Both the RNA recognition motif and the C-terminus prion-like domain mediate TDP-43 localisation to stress granules (Colombrita, 2009). TDP-43 is not required for stress granule formation, and appears to localise to stress granules in a cell-type and stressor dependent manner (Dewey *et al.*, 2012). However, TDP-43 does appear to play a role in modulating stress granule formation, as both the speed of assembly and the number of stress granules per cell are affected by TDP-43 knockdown and over-expression (McDonald *et al.*, 2011; Liu-Yesucevitz *et al.* 2011). ALS-associated mutations in TDP-43 were shown to increase the number and size of stress granules (Liu-Yesucevitz *et al.* 2011; Dewet *et al.*, 2011). Moreover, the wild-type prion-like domain was demonstrated to reversibly form a hydrogel, which was facilitated by interaction with single strand DNA (ssDNA) (Lim *et al.*, 2016). In contrast, interaction with ssDNA of the ALS-associated mutants, A315E, Q331K and M337V, triggered immediate and irreversible precipitation and aggregation, suggesting a loss of the dissociating capability of functional oligomers (i.e., reversibility). TDP-43 contains two highly fibrillogenic sequences within its C-terminus (Saini *et al.*, 2014). A tetra-(DLII) and a penta-peptide (NFGAF), from these two fibrillogenic sequences, form fibrillar hydrogels in water driven by hydrophobicity and β-sheet conformation. The hydrogel (formed after 15 days) of 3 mM NFGAF had a storage modulus G'

of 1870 Pa, and that of 2 mM DLII (formed after24 h) had a G' of 1690 Pa, both comparable to the hydrogel formed by 12 mM IAPP-derived NFGAIL at G' 2000 Pa (Lakshmanan, 2013).

Similarly to TDP-43, FUS is incorporated into stress granules upon exposure to certain stressors, RNA-binding is also required to mediate ALS mutant FUS toxicity, decreased FUS expression does not abolish stress granule formation, and FUS disease-associated mutations increase the size and number of stress granules (Daigle *et al.*, 2013; Aulas *et al.*, 2012; Baron *et al.*, 2013). In contrast to TDP-43, FUS localisation to stress granules only depends on the RNA recognition motif (Daigle *et al.*, 2013). Mutations within FUS often disrupt the nuclear localisation signal, resulting in cytoplasmic accumulation and increased recruitment to stress granules (Vance, 2013). Furthermore, ALS/FTD associated FUS mutations within the prion-like domain were shown to trigger liquid-liquid phase separation, and to increase irreversible fibrillar hydrogelation (Murakami *et al.*, 2015; Patel *et al.*, 2015). The irreversibility of hydrogelation was due to the mutations since wild-type FUS formed reversible fibrillar hydrogels (Murakami *et al.*, 2015; Kato *et al.*, 2012; Patel *et al.*, 2015). Patel *et al.* showed that the biophysical properties of the droplets formed by the ALS-associated FUS mutant, G156E, were different to those of wild-type, with slower droplet fusion followed by a complete loss of fusion and eventually to accelerated conversion into fibrils (Patel *et al.*, 2015). The N-terminal prion-like domain was shown to be responsible for the capability of FUS to phase transition into a hydrogel (Kato *et al.*, 2012; Patel *et al.*, 2015). The FUS mutant hydrogels were found to have a high viscosity (~15 kPa/s), to entrap other RBPs, to impair local neuronal granule function, and to decrease new RNA translation in axon terminals (Murakami *et al.*, 2015).

Summary and aims

In the following thesis, I will demonstrate the usefulness of a combination SNAP-tag technology and FLIM for making measurements of the microviscous environment in discrete cellular locations. This technique employs a novel BODIPY-based molecular rotor that is compatible with SNAP-tag. The introduction above has set out to highlight the importance of viscosity, phase separation, and hydrogelation in biological contexts, and the need for a probe that can be used universally to probe these *in vivo*.

Chapter 3 begins with our initial tests to ensure BG-BODIPY's properties make it appropriate for measuring viscosity in living cells. We demonstrate it is non-toxic, responds to viscosity in a fashion that allows for its calibration, and is not affected by pH. The rest of the chapter focuses on mapping the cell in terms of viscosity by targeting BG-BODIPY to various organelles and cellular compartments.This finishes with a demonstration of viscosity measurement on either side of a bilayer membrane in the living cell, in this case the inner mitochondrial membrane. This experiment shows that separate viscosities may be maintained in the matrix space and in the intermembrane space.

In Chapter 4, we attempt to reduce the scale even further and use BG-BODIPY to probe the large, rotationally symmetric protein structures that fenestrate the nuclear envelope. We attempt to target the probe to several different FG-nups that target to various points along the channel to measure the viscosity throughout the channel. We then disrupt nuclear transport in several ways in order to understand the phase of the central channel.

In Chapter 5 we turn to the use of our BODIPY fluorescent lifetime technique for viscosity measurement in whole organisms by addressing the issue of cryptobiosis, and especially anhydrobiosis. This chapter describes involves a series of experiments to examine desiccation resistant invertebrates with BG-BODIPY and monitoring their internal viscosity in response to desiccation. We show that the tardigrade *H. exemplaris* undergoes a process during its slow drying response that elicits a bizarre behaviour from BG-BODIPY, distinct from the response to acute desiccation.

Chapter 2

Materials & Methods

2.1 Buffer preparation

All buffers were prepared using standard laboratory reagents and recipes. Buffers were filtered through either a 0.22µM vacuum filter (Corning) or a 0.22µM Millex-GP syringe filter (Merck Millipore) prior to use and stored at room temperature.

2.2 Cell culture

HeLa, HCT-116, and U2OS cells were obtained from lab stocks originally traceable to ATCC and routinely cultured in Dulbecco's modified Eagle's medium (DMEM) supplemented with 10% heat-inactivated fetal bovine serum (FBS) and 1% penicillin/streptomycin and 1% non-essential amino acids (NEAA).

2.3 Plasmid DNA preparation and transfection

Plasmid DNA was purified from *E. coli* using a Monarch Plasmid Miniprep Kit (NEB) following the manufacturer's protocol. Plasmid DNA was mixed with Lipofectamine 2000 (Thermofisher) at an empirically determined ratio in serum-free DMEM which was then incubated with cells in normal DMEM overnight for transfection. Transfection occurred 24-48 hours prior to imaging, depending on the construct.

2.4 Immunofluorescence

Cells that had been grown on glass coverslips were fixed with 4% paraformaldehyde in PBS at room temperature and then quenched in 30mM glycine. The fixed cells were then permeabilised with 0.1% Triton X-100 and finally blocked in 0.5% fish skin gelatin (FSG) overnight. Cells were then labelled with primary antibodies at a concentration of 1:1000 in FSG for one hour at room temperature, washed three times for 10 minutes in PBS, stained with appropriate secondary antibodies also at 1:1000 in FSG, and washed once more in the same manner. Coverslips were finally mounted on glass slides using Vectashield (Vector Labs), sealed with colourless nail varnish.

2.5 Macrophage experiments

2.5.1 Macrophage preparation and culture

All of the following work was carried out by Agata Rumianek of the Grieves lab (Sir William Dunn School of Pathology, Oxford), as we do not have a license to carry out animal work. Hematopoietic stem cells were harvested from the marrow of mice femurs. All animal work was done with the ethical approval of Dunn School of Pathology Animal Welfare Ethical Review Board and in accordance with the United Kingdom Home Office regulations (Guidance on the Operation of Animals, Scientific Procedures Act, 1986). Balb/c mice were acquired from the Biomedical Sciences Unit (Oxford, UK) and placed in a 12-hour light/dark cycle with unrestricted access to food and water. Isolated bone marrow cells were differentiated into macrophages by culturing in 8mL DMEM supplemented with 10% head-inactivated FBS, 1% penicillin/streptomycin (P/S) and 10% supernatant derived from L929 mouse fibroblasts (L929-condition media) to provide macrophage colony-stimulating factor (M-CSF) in 100mm non-tissue culture treated Petri dishes (Thermo Fisher Scientific, Sterilin, UK).

2.5.2 Macrophage phagocytosis assay

Cells were plated at a density of 25,000 cells per well of a glass-bottomed 96-well plate (Corning) in high glucose DMEM and allowed to adhere to the bottom of the plate for 1 hour, during which time they were stained with 2.5µM BODIPY-C12. The cells were then exposed to red and blue 3µm diameter latex polystyrene beads that had been opsonized for for 1 hour in 10%v/v human serum (Sigma-Aldrich,

Gilligham, UK), which was gathered from human volunteers with ethical approval from the appropriate local ethics committee. The plate was then centrifuged for 1 minute at 400g to bring the beads into contact with the cells. Cells were then imaged on the FLIM system at various time points to observe the phagocytosis process.

2.6 Confocal microscopy

Samples were imaged on a Zeiss LSM880 with Airyscan using a Plan Apochromat 40x 1.3 NA oil immersion lens. For ratiometric imaging 16-bit images were acquired with Zen Black software. Channel registration was done using 0.1µm TetraSpeck™ Microspheres and images were corrected manually for translation, rotation and scaling.

2.7 Creation of the microfluidic chamber grids

An IsoCell printer was used to create 7 x 15 grid for the calibration of the BODIPY dyes. The bottom of a 60mm tissue polystyrene dish (Corning) was covered with DMEM + 10% FBS and the excess media removed. This was overplayed with a dense immiscible liquid, FC40 (Fluorinert™). At the microscale, gravitational and buoyant effects become negligible and the interfacial forces pin the aqueous phase under the FC40 to the plastic of the dish. The hydrophobic stylus with a conical tip made of polytetrafluoroethylene (Teflon) of the IsoCell printer was then lowered through both liquids until it makes contact with the dish. FC40 wets the Teflon tip better than water, and so as the stylus was dragged laterally, the DMEM was displaced by the FC40, which becomes pinned to the surface of the dish. A grid with 1.9mm x 1.9mm chambers was drawn in such a fashion and the DMEM was then removed from each grid chamber, pipetted out by the IsoCell, and replaced with a mixture containing 2.5µM BODIPY and varying concentrations of glycerol (0-95%) and 1 x MOPS buffers with pHs ranging from 4-10.

2.8 Viscosity probe calibration

The Förester-Hoffman equation (Equation 1.1)

$$\tau = \eta \frac{\partial v}{\partial y}$$

characterizes the power-law relationship of quantum yield and viscosity where Z and α are constants and Φ_f is the fluorescence quantum yield. The fluorescent quantum yield, and the other main parameter of fluorescence, the fluorescence lifetime, are defined by Equation 1.2

$$\Phi_f = Z\eta^{\alpha}$$

where k_r and k_{nr} are the radiative and non-radiative decay constants, respectively. It follows that a plot of $\log\Phi_f$ against $\log\eta$ yields a straight line with slope α (Kuimova, 2012). To determine the effects of pH and temperature on the BODIPY probes, we created a series of MOPS buffers with pH's that varied as integers from 4 to 10. These buffers were then each mixed with a series of glycerol volumes to create buffers ranging in viscosity ranging from 0% to 95% glycerol. These buffers with varying pH and glycerol concentration were pipetted into microfluidic chamber grids, as described below, using an Isocell, along with unbound BG-BODIPY at a concentration of 2.5µM. The contents of these chambers were then measured by FLIM.

2.9 Generation of SNAP-tag/mCherry cell lines by CRISPR/Cas9

2.9.1 Donor plasmid generation

mCherry-SNAP-Tag with the appropriate localisation signals and bGH poly(A) signal was inserted in the AAVS1 locus (GenBank accession AC010327.8 (7774 - 11429)) using a double-nicking strategy with the Cas9 D10A nickase mutant. The donor plasmid consisted of the insert enclosed in a 840 bp C term homology arm GenBank accession AC010327.8 (8372 - 9211) and a 809 bp N term homology arm GenBank accession AC010327.8 (9212 - 10021) between position 70 and 71 of the lacZa gene of pBluescript. The donor plasmids were assembled by isothermal assembly (NEBuilder® HiFi DNA Assembly) according to the manufacturer's instructions.

2.9.2 Localisations signals

Localisation signals were based on the protein localization signals database LocSigDB (Negi *et al.* 2015; Chertkova *et al.* 2017).

2.9.3 gRNA plasmid generation

gRNA and plasmid design were done following Ran *et al.* 2013 recommendations. Guides were designed with MIT design tool: `http://crispr.mit.edu/` and inserted into Addgene Plasmid #48141 pSpCas9n(BB)-2A-Puro (a gift from Feng Zhang). Guide RNAs were `5'GTCCCTAGTGGCCCCACTGT3'` and `5'GACAGAAAAGCCCCATCCTT3'` (Table 2.1).

2.9.4 Transfection and cell sorting

Plasmids containing the guides and donor templates were transfected into HeLa cells using Lipofectamine 200 following manufacturer recommendations. Cells were then left to recover and to express the fusion protein for a week before proceeding with cell sorting. Cell sorting was done on a BD FACS Aria III run with the Diva software version 8.0.2; positive cells were sorted if red fluorescence was 10^3 times brighter that control cells (excitation at 561nm 50mW, emission filter 610/20). Positive cells were single cell sorted in an optical 96 well plate containing preconditioned media and appropriate localisation of the tagged fusion protein was confirmed by confocal microscopy.

2.10 Generation of SNAP-tag/nucleoporin cell lines by CRISPR/Cas9

2.10.1 Donor plasmid generation

SNAP-Tag was inserted at the C-terminus of nup153, the C-terminus of nup214, and the N-terminus of nup98 using a version of SpCas9(1.1) that has been cloned into the pX459 plasmid and re-named it epX459(1.1). The donor plasmid consisted of the insert enclosed in 600bp homology arms either side of the insertion site for each of the probes.

2.10.2 gRNA plasmid generation

gRNA and plasmid design were performed by our inhouse CRISPR service. Guides were inserted into the epX459(1.1) vector and the protospacer target sequences were as follows:

nup98: `gAGATGTTTAACAAATCATT`
nup153: `gTGTTAGACGCAGGAAATAA`
nup214: `gCAGGGTTTTGGTGGCTGGC`

Cytoplasm	Consensus MAPKK-NES: NLVDLQKKLEELELDEQQ	C-terminus
Peroxisomes	SKL	C-terminus
Endoplasmic reticulum	Residues 1 to 17 of Calreticulin precursor: MLLSVPLLLGLLGLAVA	N-terminus
	KDEL	C-terminus
Lysosomes	Residues 1 to 26 of HsLAMP1: MAAPGARRPLLLLLLAGLAHSAPALF	N-terminus
	Residues 27 to 407 of HsLAMP1: EVKDNNGTACIMASFSASFLTTYEAGHVSK VSNMTLPASAEVLKNSSSCGEKNASEPTLA ITFGEGYLLKLTFTKNTTRYSVQHMYFTYN LSDTQFFPNASSKGPDTVDSTTDIKADINK TYRCVSDIRVYMKNVTIVLWDATIQAYLPS SNFSKEETRCPQDQPSPTTGPPSPSPPLVP TNPSVSKYNVTGDNGTCLLASMALQLNITY MKKDNTTVTRAFNINPSDKYSGTCGAQLVT LKVGNKSRVLELQFGMNATSSLFFLQGVQL NMTLPDAIEPTFSTSNYSLKALQASVGNSY KCNSEEHIFVSKALALNVFSVQVQAFRVES DRFGSVEECVQDGNNMLIPIAVGGALAGLV LIVLIAYLIGRKRSHAGYQTI	C-terminus
Mitochondria	Residues 1 to 29 of HsCOX8, 4 times: MSVLTPLLLRGLTGSARRLPVPRAKIHSLG DPMSVLTPLLLRGLTGSARRLPVPRAKIHS LGKLMSVLTPLLLRGLTGSARRLPVPRAKI HSLGDPMSVLTPLLLRGLTGSARRLPVPRA KIHSLG	N-terminus
Golgi apparatus	Residues 3131 to 3259 of HsGiantin: EPQQSFSEAQQQLCNTRQEVNELRKLLEEE RDQRVAAENALSVAEEQIRRLEHSEWDSSR TPIIGSCGTQEQALLIDLTSNSCRRTRSGV GWKRVLRSLCHSRTRVPLLAAIYFLMIHVL LILCFTGHL	N-terminus

Table 2.1: Peptide sequences for mCherry/SNAP-tag targetting moieties

2.11 SNAP-tag labelling for FLIM and confocal microscopy

Plated cells were treated with 2.5µM BG-BODIPY for 30 minutes. Cells labelled with SNAP-Cell TMR-Star were treated with a 1:1000 dilution of dye in media. Cells were then washed three times for 10 minutes with 5% BSA (Sigma-Aldrich, A1595) in DMEM in order to back extract the remaining free fluor. Following washing, cells were covered in Fluorobrite DMEM (ThermoFisher) media for imaging.

2.12 Fluorescence lifetime measurements

Fluorescence lifetime imaging microscopy (FLIM) was carried out on an Olympus FV 1000 with a Becker & Hickl SPC-150 Time-Correlated Single Photo Counting (TCSPC) module. A solid state 488nm laser pulsed at 80mHz was used as an excitation source. Fluorescence decays measurements collected using the Spcm software and analysed using the SPCM software provided by Becker & Hickl. A two exponential decay model was used for fitting the curves, denoted by the equation:

$$I(t) = \sum_{i=1}^{n} \alpha_i \exp \frac{-t}{\tau_i} \tag{2.1}$$

where $I(t)$ is the time-independent fluorescence intensity, $\boldsymbol{\tau}$ is the lifetime, and $\boldsymbol{\alpha}$ is the amplitude.

All images were acquired with a 60x objective to negate any polarization effects, as NA=1.4 oil-immersion microscope lenses are free of anisotropy (Becker, 2015). All measurements were performed at room temperature. Following multiexponential fitting, the raw lifetime data for each pixel was exported to FIJI, where regions of interest were selected to create more accurate lifetime histograms that were converted to cP using the equation in Figure 3.6b.

2.13 Tardigrade culture and staining

Hypsibius examplaris cultures suspended with algae for food were obtained from Robert McNuff at Sciento and were subcultured into petri dishes with distilled water. Tardigrades were pipetted into a well of a 96-well plate containing 200uL water and incubated with 2.5µM BG-BODIPY overnight before either desiccation

or control imaging. In order to immobilise tardigrades for long FLIM acquisitions, 1% chloroform was added just prior to imaging.

2.14 Tardigrade tun formation

For the slow drying condition, tardigrades suspended in 10µl of water were plated on Matek dishes coated in 2% agarose with holes for holding the droplets. The dishes were put in a humidified (>90% humidity) box, which was itself placed in an incubator set to 37°, overnight. For the fast drying condition, tardigrades in suspension were pipetted directly onto Matek dishes and dried at 37° for 30min.

Acute osmotic stress was applied by adding 20 or 90% Dulbecco's phosphate buffered saline (PBS) (Sigma, ~300 mOs/kg) to wells of an optical 96-well plate containing tardigrades. Tun formation occurred over the course of 10-30 minutes, at which point the tuns were imaged.

2.15 Rotifer culture and desiccation

A culture of *Philodina sp.* was obtained as a generous gift from the Barraclough lab (Department of Zoology, University of Oxford). The culture was originally isolated from activated sludge from Kujawy Wastewater Treatment Plant in Kraków, Poland, in 2010 November/December, by Edyta Fiałkowska. This culture was subcultured into a petri dish with spring water and fed the modified *E. coli* strain OP50 and baker's yeast. For FLIM measurement, rotifers were plated on an optical 96-well plate and stained overnight with 2.5µM BG-BODIPY and immobilised with 1% chloroform just prior to imaging. For desiccation, we followed the advice of the Barraclough lab and incubated stained rotifers at room temperature at >90% humidity for 24 hours, and then at 40% humidity for a further 48 hours. Constant 40% humidity was achieved by placing rotifers in a box with a saturated solution of water and NaI (Winston & Bates, 1960).

Chapter 3

Optimisation, calibration, and proof of principle of BG-BODIPY in human cells

3.1 Introduction

It is difficult to conceive of a development in the evolutionary history of life more dramatic and more impactful than the emergence of the eukaryote. Lane and Martin (2010) perfectly expressed the profundity of this revolution:

> Prokaryotic genome size is constrained by bioenergetics. The endosymbiosis that gave rise to mitochondria restructured the distribution of DNA in relation to bioenergetic membranes, permitting a remarkable 200,000-fold expansion in the number of genes expressed. This vast leap in genomic capacity was strictly dependent on mitochondrial power, and prerequisite to eukaryotic complexity…

Thus, the separation of the cell into discrete organelles is not simply a means division of labour, but this spatial reorganisation provides the biochemical conditions requisite for complex life. Of course, this assumes an account of prokaryotic evolution which we may never be able to verify with any certainty. However, once conceived of in this way, it is not difficult to think of other ways in which the spatial partitioning of the cell allows for increased complexity. For example, lysosomal enzyme function requires a low pH, but additionally changing the relative pH between lysosomes and the cytoplasm by lowering cytoplasmic pH also appears to alter lysosomal morphology (Heuser, 1989). Likewise, prohormone processing

requires a precise gradient of pH through the secretory pathway, with proteins encountering decreasing pH as they proceed from the endoplasmic reticulum (ER) to the Golgi apparatus to mature secretory granules (MSGs) (Wu *et al.*, 2001).

While a key feature of eukaryotes is to segregate functional domains by enclosure in semi-permeable phospholipid bilayer membranes, it is not a large leap to imagine that organelles similarly act to partition cells in terms of viscosity to provide disparate conditions for various enzymatic reactions within the cell. By regulating viscosity, and thus the rate of diffusion of molecules, organelles would be able to regulate enzyme kinetics not only in the spatial domain, but in the temporal domain, as well. This notion is not pure speculation; the idea that enzyme kinetics are subject to influence from organelle viscosity (often metonymically referred to in terms of molecular crowding or organelle volume) is well noted in the literature (e.g. Lizana *et al.*, 2008; Olveczky & Verkman, 1998; Dieteren *et al.*, 2011).

That being said, the research into this particular area is sparse, reflective of our inability hitherto to accurately measure microviscosity in vivo. Most attempts at measuring microviscosity in living cells have relied primarily upon a class of synthetic fluorescent molecules that respond to the local viscous environment, termed molecular rotors (Haidekker and Theodorakis, 2007). Boron-dipyrrin (BODIPY) is one of the most commonly used molecular rotors. Bodipy belongs to the TICT class of molecular rotors, and is therefore a viscosity reporter in that its de-excitation after absorbing a photon occurs through a competition between fluorescence and non-radiative decay through intramolecular rotation (M. K. Kuimova *et al.*, J. Am. Chem. Soc., 2008, 130, 6672-6673; M. A. Haidekker and E. A. Theodorakis, Org Biomol Chem, 2007, 5, 1669-1678). BODIPY molecular rotors have a number of attractive traits, such as their strong UV absorbance, their stability in physiological conditions, and their tunability with small chemical modifications (A. Loudet and K. Burgess, Chem. Rev., 2007, 107, 4891-4932; J. A. Levitt, M. K. Kuimova, G. Yahioglu, P.-H. Chung, K. Suhling D. Phillips, J. Phys. Chem. C, 2009, 113, 11634-11642).

Recently, there has been a spate of efforts to map eukaryotic cells in terms of viscosity. Kuimova *et al.* (2008) loaded SK- OV-3c cells with meso-substituted 4,4'-difluoro-4-bora-3a,4a-diaza-*s*-indacene not conjugated to any targeting molecule, measuring the viscosity in various subcellular localisations. Levitt *et al.* (2009) used two meso-substituted BODIPY based fluors conjugated to hydrophobic groups designed to drive indiscriminate incorporation into the hydrophobic interior of

non-aqueous cellular membranes, and discovered that the intracellular environment contains a wide range of viscosities. Several groups have targeted borondipyrrin (BODIPY) modified by the addition of triphenylphosphonium to target the dye to the mitochondria with varying degrees of success (Song *et al.*, 2016; Su *et al.*, 2016).

What is lacking is a universal means of measuring microviscosity at various subcellular locations; the picture thus far is piecemeal, and the validity of direct comparisons between the measurements made with different probes is uncertain. The driving force behind this thesis has been to redress this through developing a BODIPY-based fluorescent probe that is compatible with SNAP-tag technology. SNAP-tag utilises an *O*6-alkylguanine-DNA alkyltransferase enzyme expressed either through transient expression or CRISPR knock-in. This modified enzyme binds a benzylguanine group to produce a covalent adduct that cannot be resolved, so that the enzyme becomes covalently linked to this substrate.

Unfortunately, we were not the only group to identify this need, and several years into my project, Chambers *et al.* (2018) published a very similar technique to that which we have developed. They developed a BODIPY based fluor with a chloroalkane linker that allows for it to be used with the HaloTag system as opposed to SNAP-tag, but the principle is much the same. They then went on to target this probe to U2OS cells transiently expressing the HaloTag enzyme in the mitochondrial lumen and the endoplasmic reticulum ER, as well as an untargeted construct that labelled the cytosol and nucleoplasm. Probe targeting was validated at the light microscope level only, and the level of targeted HaloTag varied widely from cell to cell because expression relied upon transiently transfected plasmids. They made viscosity measurements for each of these compartments and then altered the viscosity with extracellular osmotic stress. Finally, they demonstrated they could alter the microviscous environment of the mitochondria with ionomycin.

This was obviously a disheartening development. That being said, while the HaloTag and SNAP-tag systems are fairly redundant, we felt that we could justify continuing our research by showing BG-BODIPY's usefulness in a range of biological systems and making viscosity measurements of mammalian cells without overexpressing the SNAP-tag enzyme. I believe the research we present here surpasses that presented in the Chambers paper for a number of reasons, chiefly that we use a low level of expression so as to not perturb the system, introduce a second

viscosity-insensitive fluor to allow for ratiometric measurements, and that long term imaging is possible in our system because the bound probe is not lost by turnover of transiently expressed fusion protein.

In this chapter, I outline the experiments we performed to verify that our novel probe BG-BODIPY is suitable for use in labelling living cells, and that it can be calibrated to make measurements of microviscosity. I then show that BG-BODIPY can be targeted to discrete subcellular compartments to make viscosity measurements in the various organelles. Finally, I show that BG-BODIPY can be targeted to membraneless organelles by expressing the SNAP-tag enzyme attached to a protein involved in the phase separation process. This system presents many possibilities, as it can be combined with any number of target sequences or proteins, and can accommodate numerous sensors (for example for calcium ion concentration, pH, and redox potential (Martineau *et al.*, 2017; Ruggiu *et al.*, 2010; Bannwarth *et al.*, 2009)) so long as they can be conjugated to a benzylguanine group and exhibit cell-penetrant properties. Further, the ability to measure viscosity either by quantitating the intensity of the fluorophore signal or the variations of its lifetime confers upon this technique an improved degree of flexibility, with each complementary method making up for the limitations of the other.

3.2 Results

3.2.1 BODIPY-C12 can detect phagocytosis in macrophages

To date, the majority of work with BODIPY probes attached to fatty acid chains has been to study lipid membranes *in vitro*, such as in giant unilamellar vesicles (GUVs) (e.g. Vyšniauskas *et al.*, 2016; Dent *et al.*, 2015). However, there have been some attempts to use these probes in more complex biological settings. For example, BODIPY-C12 was used to measure membrane viscosity in hippocampal neurons to demonstrate that cholesterol depletion through treatment with methyl-β-cyclodextrin (MβCD) results in decreased ligand binding to the serotonin1A receptor (Pal *et al.*, 2016). We were interested in further showcasing the ability of BODIPY-C12 to detect changes in microviscosity at the membrane in biological processes.

To do this, we decided to follow macrophage phagocytosis to see if there were detectable changes in viscosity at the membrane during this process. Macrophages were differentiated from mouse femur stem cells derived from Balb/c mice. These

macrophages were plated on optical 96-well plates (Corning), stained with 5µM BODIPY-C12 and allowed to rest for one hour. Opsonised blue 3 µm diameter latex polystyrene beads (Sigma-Aldrich, Gilligham, UK) were then introduced into the wells such that there were multiple beads per cell, and then the plate was spun to evenly spread the beads on top of the macrophages.

We then made a time course of phase contrast images and FLIM images to see if we could detect changes in viscosity around the beads as they were phagocytosed. After just 30 minutes we could already see beads that had been taken up by the macrophages, and indeed it appears there is a decrease in the lifetime of BODIPY-C12 at points within the cell corresponding to the engulfed beads (Figure 3.1). These low viscosity points become more numerous at later time points as more beads are phagocytosed.

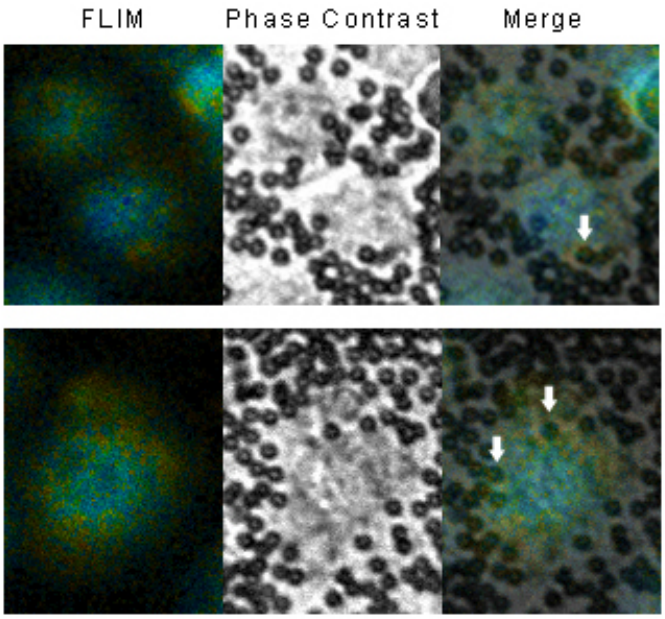

Figure 3.1: **Pockets of low lifetime around phagocytosed beads.** Macrophages labelled with BODIPY-C12 and introduced to opsonized beads. Once they were phagocytosed, we observed spots of high lifetime in the exact position of the beads, surrounded by pockets of low lifetime. Arrows indicate better examples.

When the lifetime histograms for images of numerous macrophages at the different timepoints are overlaid, it becomes clear that there is a downward shift in lifetime throughout the cells over time (Figure 3.2). After 26 hours the entire population of BODIPY-C12 was reporting a very short lifetime. It seems unlikely that this reflects the true microviscous environment for the entire cell, although I suppose

it is possible. More likely, this is probably an artefact caused by BODIPY-C12 being degraded within the phagosomes after prolonged exposure.

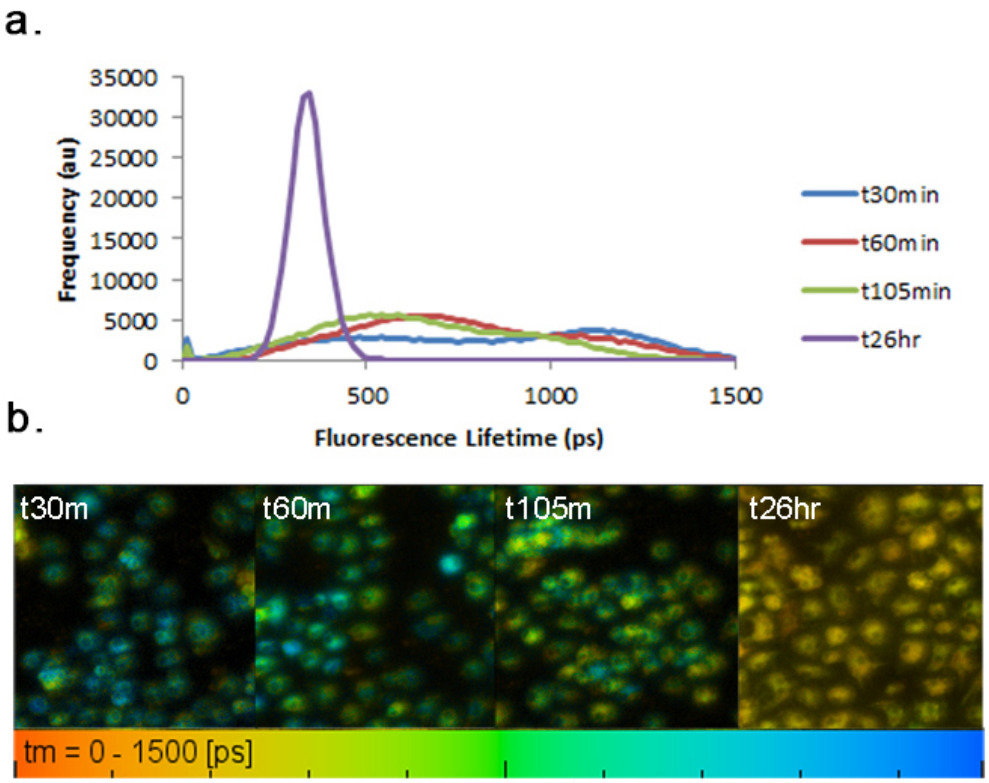

Figure 3.2: **BODIPY-C12 reports changes in internal viscosity of macrophages during phagocytosis.** a. Lifetime histograms and b. FLIM images of macrophages at different time points following the introduction of opsonized beads.

3.2.2 Synthesis of BG-BODIPY and its longer linker derivatives

Prior to the beginning of my degree, our lab partnered with Professor Tim Donohoe's lab (Department of Chemistry, University of Oxford) to synthesise and analyse a novel BODIPY based fluorophore that was compatible with SNAP-tag technology. They began by synthesising a mesosubstituted BODIPY fluorophore with a fatty-acid tail that incorporated the probe into membranes, as previously described in Levitt *et al.* (2009), and here referred to as BODIPY-C12. The new probe comprised a BODIPY molecular rotor conjugated via a linker to a benzylguanine group, a substrate for the modified *O*6-alkyguanine-DNA alkyltransferase (AGT) employed by SNAP-tag, altered such that upon trying to cleave its substrate, the two become covalently linked (Keppler, 2013). A former DPhil student

in our lab, Helder Carmen, tested the spectral properties and viscosity response of BG-BODIPY and several intermediates along the synthesis pathway to ensure this molecule retained its viscometric properties. He measured the fluorescence lifetime of BG-BODIPY and its intermediates in glycerol-methanol mixtures of varying concentrations and compared them to that of BODIPY-C12.

An early concern with this approach was the possibility that the appropriately immobilised BODIPY probe would report steric rotational inhibition from interaction with the protein it was conjugated to, as opposed to the 'real microviscosity.' While recognising this possibility, we felt it to be of limited significance, not least because the BG-BODIPY probe would always be in the same immediate molecular environment by virtue of its attachment to the common SNAPtag enzyme, whatever the globular protein to which it was in turn tethered. Thus, the fluor and the protein of interest would always be separated by the SNAP-tag enzyme. Further, the microviscosity of a hydrogel, such as the putative one that fills the central channel of the NPC, would somewhat definitionally be a product of steric hindrance by the crosslinked FG-Nups. However, partially to address this criticism, but also because they would allow us to answer other questions, we partnered with the Donohoe lab once more to create BG-BODIPY derived probes with linkers that were twice and three times the length of the original (Figure 3.3).

3.2.3 Fluorescence spectra of BG-BODIPY, 2-linker BG-BODIPY, and 3-linker BG-BODIPY

We measured the excitation and emission spectra of the original BG-BODIPY, and those of the longer linker versions in order to establish they would be compatible with our pulsed 488 laser, as we no longer had a tunable laser in the department. While BG-BODIPY had excitation and emission spectra that mirrored one another around 506nm (Figure 3.4a), the 2-linker and 3-linker probes appeared to have different emission and excitation spectra depending on whether they were excited at 430 or 470nm, or monitored at 530 or 570nm, respectively (Figure 3.4b).

This gave us pause, as, although we would be able to excite both the 2- and 3-linker probes with the pulsed 488, they were exhibiting a complex behaviour and we were unsure how this would affect their viscosity response. We wanted to see whether this behaviour persisted at high viscosities, so we repeated measuring the emission spectra of the probes in 100% glycerol. While the values were slightly

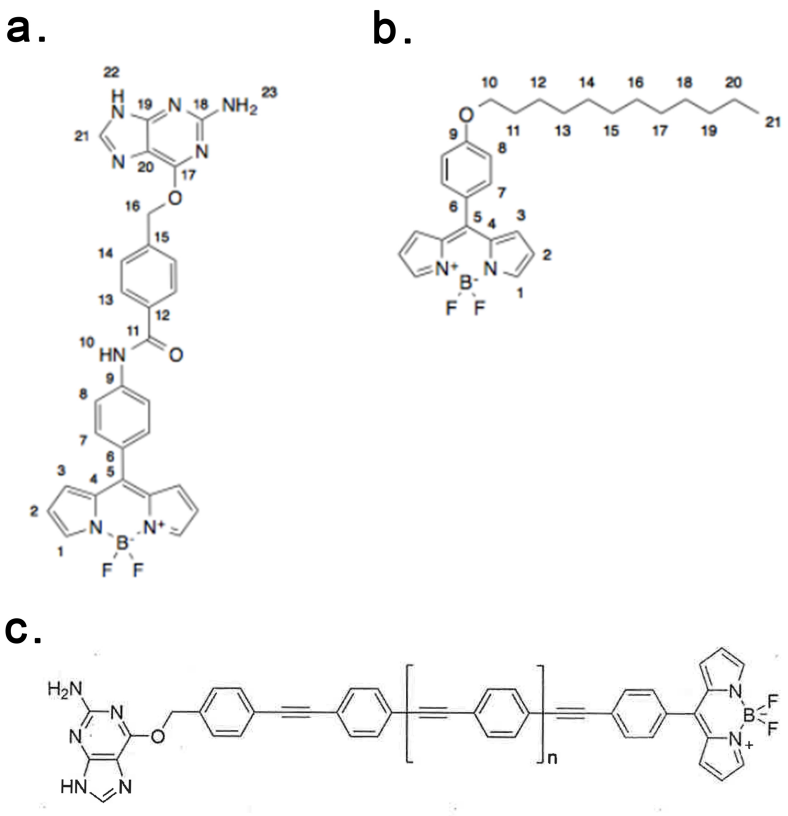

Figure 3.3: **Chemical structures of molecular rotors used in this thesis.** a. BG-BODIPY b. BODIPY-C12 c. The longer linker versions of BG-BODIPY where the portion in brackets indicates the rigid phenyl-acetylene linker moiety that is repeated n times, either twice or three times in the 2-linker and 3-linker probes.

downshifted, these spectra now greatly resembled those of the original probe in water (Figure 3.4c).

Clearly this shows that the addition of the linker is having an effect on the fluorescence behaviour of the probes, and in the absence of a full explanation, we were reluctant to use these dyes for experiments. This behaviour could possibly be explained by the flexible regions at either end of the linker region, which could allow movement of the BODIPY and benzylguanine groups in low viscosity environments.

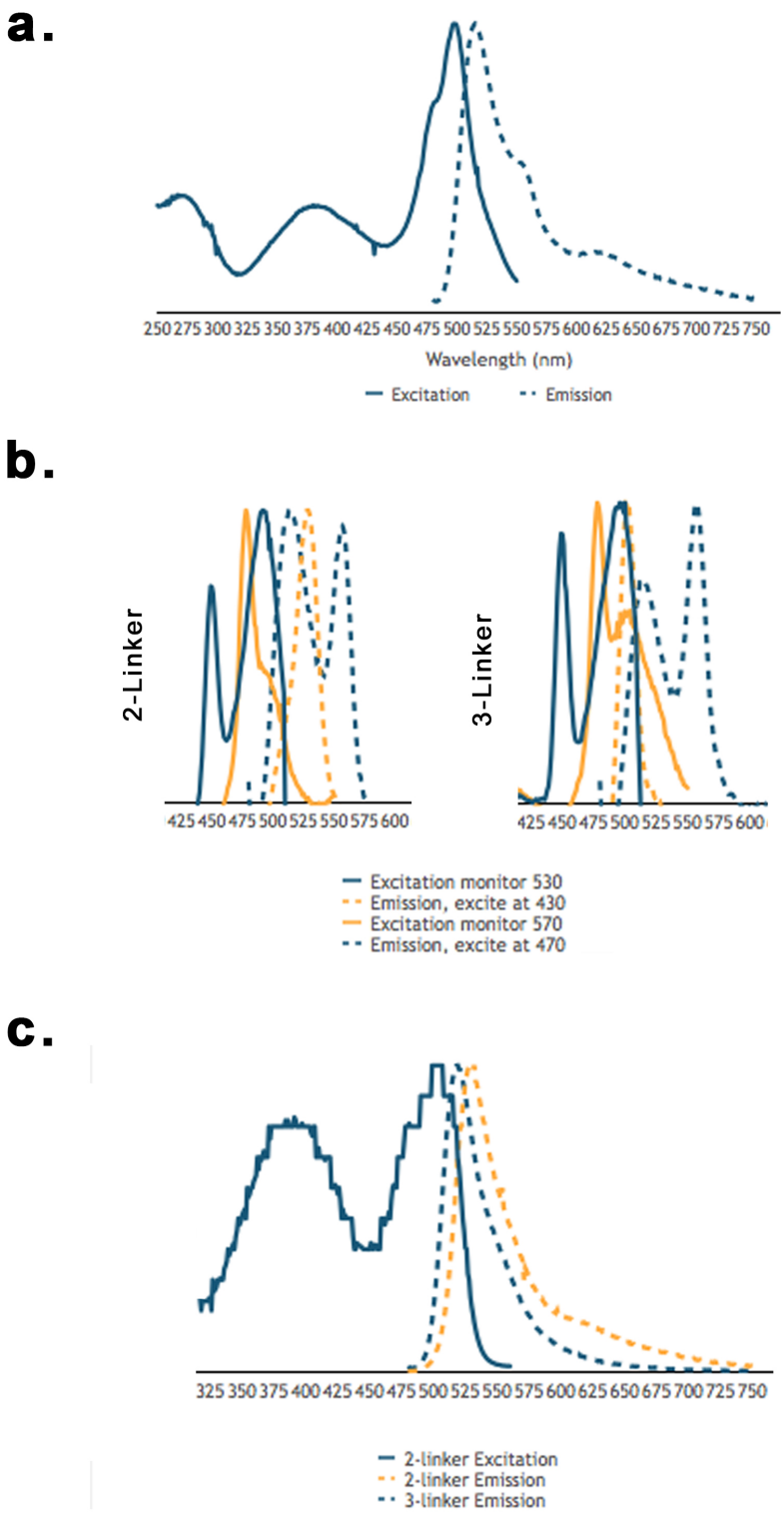

Figure 3.4: Fluorescence spectra of BG-BODIPY and its longer linker derivatives.

3.2.4 BG-BODIPY is sensitive to viscosity in the lifetime and intensity domains

An early concern we had with using BG-BODIPY in mammalian cells was the potential confounding effect the variation in local pH within different organelles might have on the probe's lifetime. In order to demonstrate these probes were sensitive to viscosity but relatively insensitive to pH, we needed to create highly accurate glycerol mixtures of varying concentrations and pH. This was achieved by using an IsoCell microfluidics printer (Soitu *et al.*, 2018) (Figure 3.5) to create grids of 2 mm fluid cells, partitioned with a water-immiscible fluid (FC-40), and containing varying percentages (vol/vol) of glycerol (0 to 95%) and MOPS buffer at 7 different integer pH values (4 to 10). Initially we had attempted to hand pipette these mixtures into qPCR plates and measure the fluorescence intensity of the probes in response to the changes in viscosity and pH in a real-time PCR system, which would also facilitate experiments at a wide range of temperatures. However the manual pipetting errors associated with high (and varying) viscosity solutions and small volumes proved to be significant enough to render these measurements largely useless. The IsoCell printer allowed us to make highly accurate mixtures in small volumes.

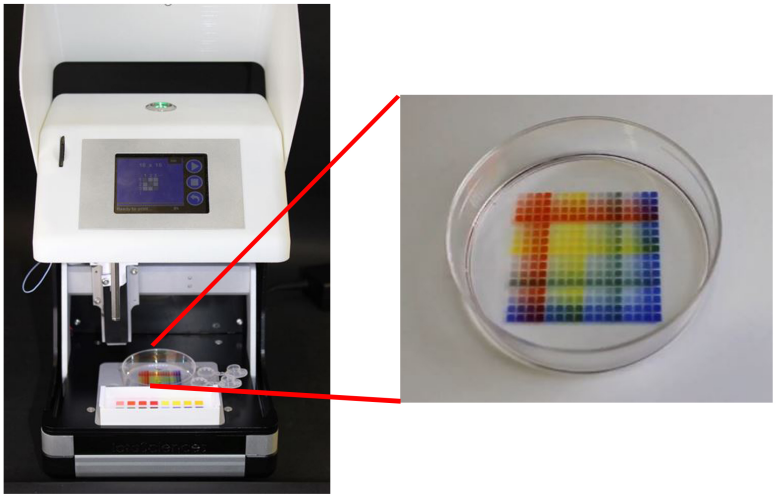

Figure 3.5: **The Isocell microfluidics printer.** Inset shows an example of a grid printed by the Isocell under FC40.

These grids, despite being partitioned by fluid walls, are remarkably sturdy, and we were able to make both fluorescence lifetime and intensity measurements across a range of viscosities and pH's for all three dyes.

We found that the pH did not have a significant effect on either the measured lifetime or intensity of BG-BODIPY across the whole range of viscosities (Figure 3.6a). The intensity domain measurements showed slightly more variation, particularly at high viscosity (Figure 3.6c), but we attributed this to positional variations of the grid squares in the field of view due to the grid not being perfectly level. However, these did not appear to have an effect in the lifetime domain. At each pH, we plotted the $\log \Phi_f$ against $\log \eta$ and determined that the ratio followed a linear relationship (Figure 3.6b).

We were interested to see how the lifetime behaviour of the probe varied, if any, from its intensity. For each pH and viscosity data point, we divided the lifetime by the fluorescence intensity and plotted all of the points as a surface plot as before. The surface plot was almost entirely flat, indicating that the lifetime and intensity of BG-BODIPY is very tightly correlated over a wide range of pH and viscosity (Figure 3.6d). As was expected, this relationship was more variable at the lower viscosities where BG-BODIPY's emission intensity is much lower, and thus more subject to interference from background signals.

3.2.5 BG-BODIPY is non-toxic to mammalian cells

Many of the experiments we designed over the course of this thesis occurred over the course of several hours. It was crucial, therefore to demonstrate that BG-BODIPY was non-toxic to cells and that the labelling process would not negatively impact cell viability. To test this, we stained and washed wild type HCT-116 cells and all of the mCherry/SNAP-tag CRISPR knock in lines we make in SECTION? 3.2.8 according to the optimised protocol we outline below and imaged the cells with an Incucyte live cell analysis system for 18 hr (Figure 3.7). Cells continued to proliferate as usual regardless of the subcellular location of the targeted probe after labelling, indicating BG-BODIPY is non-toxic to cells.

This finding is important as BODIPY based probes have shown in the past that apoptosis has a dramatic effect on the microviscous environment of the cell (Gupta *et al.*, 2016; Zhu *et al.*, 2014). Having ruled out any such effects from our probe on mammalian cells, we were able to stain cells and make measurements with confidence.

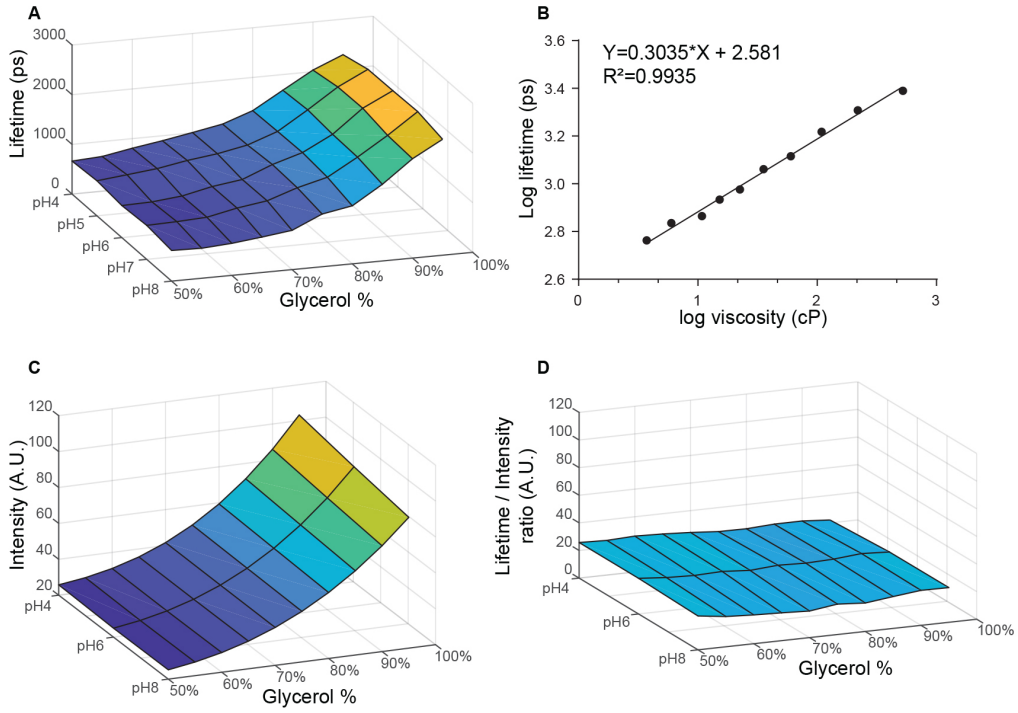

Figure 3.6: **BG-BODIPY reports microviscosity in both the lifetime and intensity domains and is pH insensitive.** Calibration of BG-BODIPY. a. The lifetime of BG-BODIPY in picoseconds (z-axis) measured at various pH values (y-axis) and glycerol concentrations (x-axis). b. The log plot of fluorescence lifetime as a function of the log viscosity for BG-BODIPY in pH 7 MOPS buffer. The function is linear, expressed by the equation $Y = 0.3035X + 2.581$. c. The intensity of BG-BODIPY fluorescence measured at various pH values (y-axis) and glycerol concentrations (x-axis). d. The ratio of lifetime over intensity at various pH values (y-axis) and glycerol concentrations (x-axis).

3.2.6 BG-BODIPY targets specifically to SNAP-tags expressed in various cellular locations

Having shown that BG-BODIPY staining is tolerated well by live cells, we needed to demonstrate that it was capable of being targeted to SNAP-tag enzyme expressed in live cells. Hitherto, Helder had been unable to see a specific BG-BODIPY labelling, and there was some concern it was not able to act as a substrate for the modified AGT.

To test the hypothesis that a specific SNAP-tag targeted signal was being obscured by persistent unbound probe, we examined methods to improve the removal of all probe except that covalently attached to SNAP-tag. We began with longer and more numerous washes, at a range of temperatures, without much improvement.

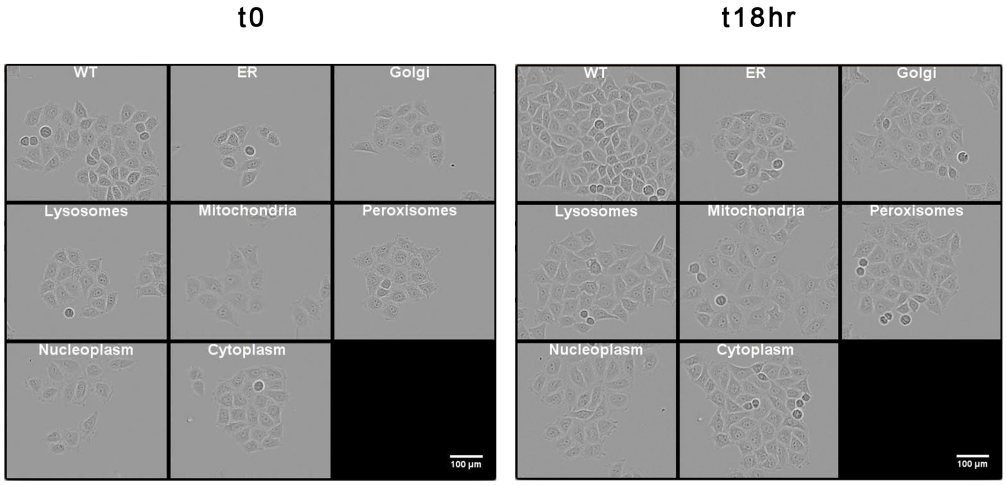

Figure 3.7: **BG-BODIPY does not affect cell viability.** Cells were treated with BG-BODIPY as described in the methods and were imaged in an Incucyte for 18h every 5 minutes. From left to right, top to bottom: WT, ER, Golgi apparatus, Lysosomes, Peroxisomes, Mitochondria, Nucleoplasm, Cytoplasm mCherry-SNAP-Tag tagged cells lines. We show here the beginning and ending timepoints, demonstrating continued cell division.

Recalling methods to improve removal of unbound but relatively hydrophobic molecules during washing in other contexts, we considered the possibility of introducing a molecular sink to facilitate back extraction of the probe. To achieve this, the DMEM-based washing solutions were augmented with a high concentration of delipidated bovine serum albumen (BSA). We optimised the washing conditions and found that 3 x 10min washes with 5% BSA was sufficient to reduce the levels of unbound BG-BODIPY to that of background signal in unstained cells (Figure 3.8).

New England Bioscience's SNAP-Cell Starter Kit includes two control plasmids, a modified Beta-2 adrenergic receptor (ADR) that targets the SNAP-tag probe to the extracellular face of the plasma membrane, and pSnapf-COX8A, a modified subunit of the cytochrome c oxidase that targets the SNAP ligand to the intermembrane space of the mitochondria. To test whether the back extraction protocol revealed a real signal of properly targeted BG-BODIPY, we expressed pSnapf-COX8A in HeLa cells and co-labelled cells with BG-BODIPY (30 minute labelling followed by 3 x 10 minute washes with 5% BSA DMEM) and Mitotracker Red (ThermoFisher, M22425) according to the manufacturer's protocol. We then measured the colocalisation of the two with the a Zeiss LSM880 in Airyscan mode

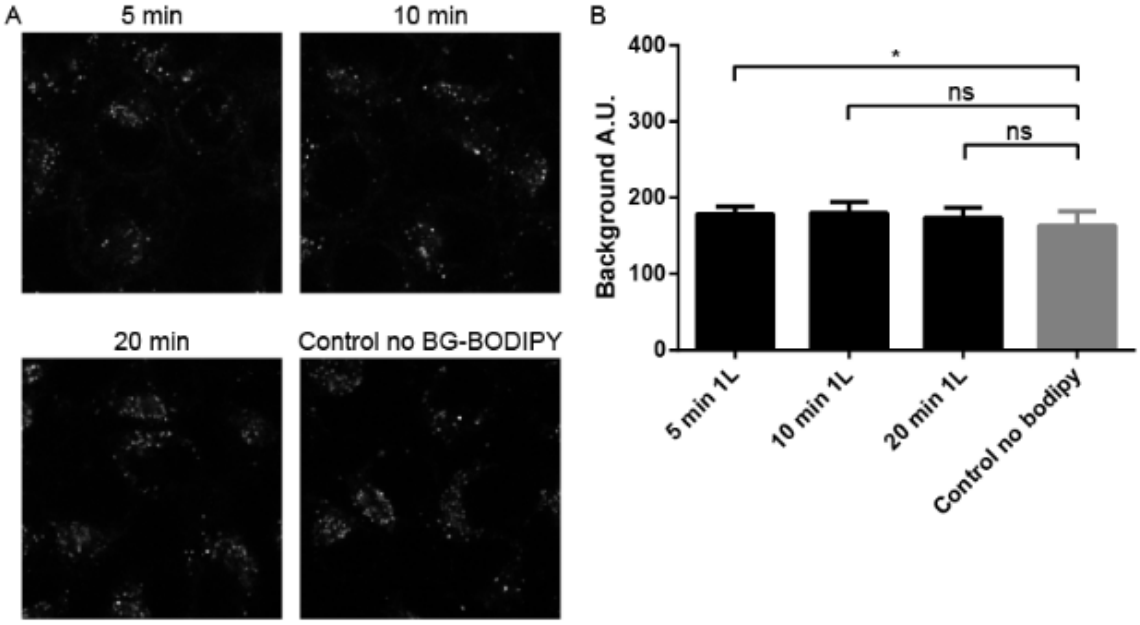

Figure 3.8: **Unspecific bound BG-BODIPY can be removed with fatty acid free BSA containing DMEM washes.** a. Green channel fluorescence images of cells stained with BG-BODIPY and washed with 5% BSA for 3 x 5 minutes, 3 x 10 minutes, or 3 x 20 minutes compared with cells that had not been stained at all. b. A graphic depiction of the relative fluorescence intensities of the various washing conditions compared with the unstained cells. Only the 5 minute washes are significantly brighter than the control.

(Figure 3.9) and found a highly significant amount of overlap (Overlap Coefficient=0.986 r^2= 0.971), indicating that BG-BODIPY can target to discrete organelles with a high degree of specificity.

3.2.7 BG-BODIPY reports distinct lifetimes at various cellular locations

Next, we wanted to see if BG-BODIPY's lifetime varied depending on where it was targeted to within the cell. We transfected HeLa cells with the two control plasmids provided by the NEB SNAP-Cell Starter Kit, pSnapf-ADR and pSnapf-COX8, and labelled them with 2.5µM BG-BODIPY for an hour, followed by the optimised washing protocol outlined above (3 x 10 minute washes in DMEM with 5% delipidated BSA at room temperature).

BG-BODIPY targeted appropriately to both the plasma membrane and the mitochondria, with pSnapf-ADR showing some labelling in the endoplasmic reticu-

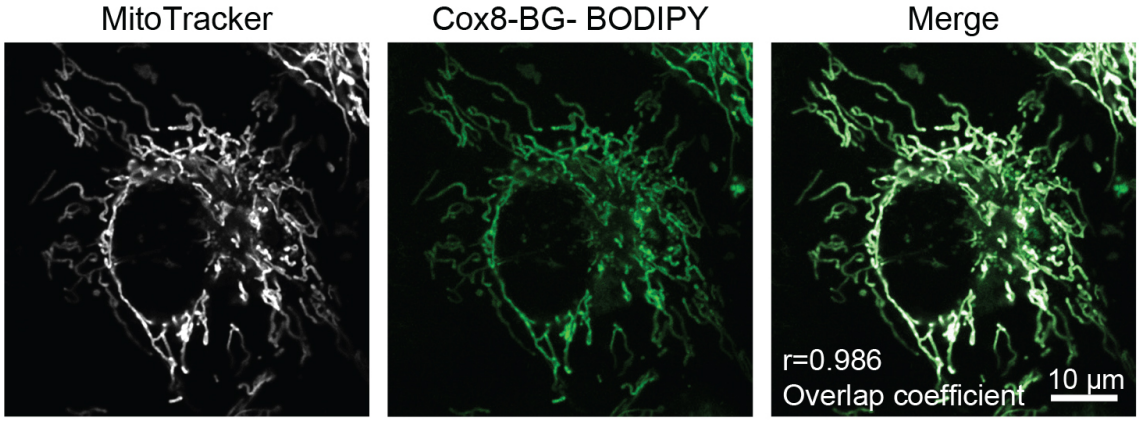

Figure 3.9: **BG-BODIPY targets specifically to subcellular compartments.** Colocalization of Mitotracker with transient expression of a Cox8/SNAP-tag fusion protein (Overlap Coefficient=0.986 rs^2= 0.971).

lum (ER), as well. FLIM was performed on both, and the images were analysed in SPCImage analysis software from Becker & Hickel. As can be seen in Figure 3.10, the lifetime histograms of BG-BODIPY targeted to the PM and mitochondria vary greatly. At the PM, BG-BODIPY reported a wide range of lifetimes centered around 1900ps. BG-BODIPY targeted to the mitochondria reported a much narrower peak at around 2500ps, indicating a higher local viscosity.

These relative lifetimes make *prima facie* sense. One would expect that BG-BODIPY constrained within the tightly-packed mitochondrial matrix would experience a higher relative microviscosity than that targeted to the outer surface of the cell, where it would be restricted in rotation only by the dilute extracellular medium and the molecular environment at the plasma membrane.

We had initially hoped at one point, rather foolishly in retrospect, to perform a lifetime calibration on BG-BODIPY while bound to the outside of the PM in order to see if it differed any to the curves made from the dye free in solution. Initial experiments showed that the PM-immobilised probe still reported viscosity changes, but began at a much higher baseline level even in normal medium. We hypothesised that the ADR-SNAPtag attached the BG-BODIPY probe very close to the plasma membrane surface, such that the glycocalyx became a significant player in the reported viscosity. However, we were foiled by the presence of the glycocalyx and the not insignificant microviscosity experienced by the probe. However, attempts to confirm this explanation by removal of the glycocalyx by proteolytic cleavage with pngaseF did not manage to significantly reduce the microviscosity.

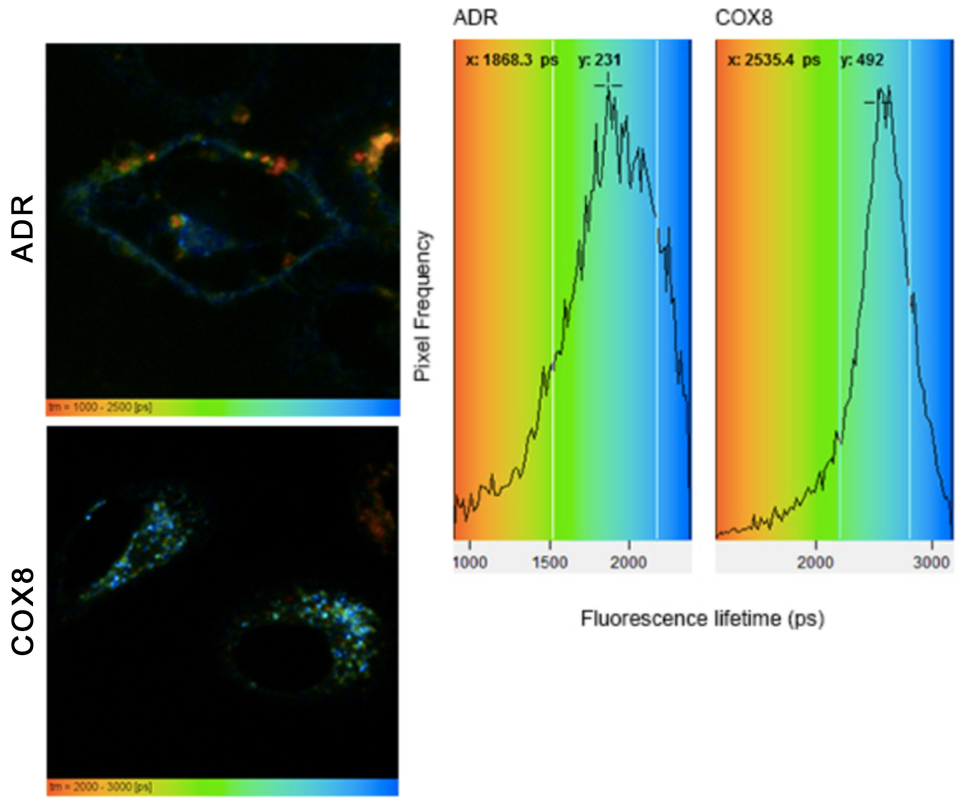

Figure 3.10: **BG-BODIPY targeted to different cellular environments reports different fluorescent lifetimes.** FLIM images and lifetime histograms for BG-BODIPY labelling of cells expressing the pSnapf-ADR and pSnapf-COX8A plasmids.

3.2.8 Mapping cellular viscosity using BG-BODIPY in both the intensity and lifetime domains

FLIM analysis, though an incredibly powerful and informative technique, is limited by the fluorescence yield required, the time needed for acquisition (on the order of minutes), and the resolution of the images generated. In order to work around these limitations, and to demonstrate BG-BODIPY's versatility as a probe, we wanted to test the ability of the probe to deliver ratiometric viscosity measurements. Ratiometric viscosity measurements sidestep the confounding problem of concentration effects by pairing molecular rotors 1:1 with a fluorescent dye that is insensitive to viscosity.

To this end, Lior Pytowski generated a series of HeLa cell lines, inserting the DNA encoding a complex fusion protein of SNAP-tag enzyme, an mCherry fluorophore,

and a subcellular localisation signal (see Table 2.1) into the AAVS1 safe-harbour locus (GenBank accession AC010327.8 (7774 - 11429)) using a double-nicking strategy with the Cas9 D10A nickase mutant. Insertion into the AAVS1 insertion site results in constitutive low-level expression of the encoded fusion protein without interrupting other gene expression behaviour. Seven lines were generated, targeting the mCherry/SNAP-tag fusion protein to the endoplasmic reticulum (ER), Golgi apparatus, lysosomes, peroxisomes, mitochondria, nucleoplasm, and cytoplasm.

We compared the targeting of BG-BODIPY in the mitchondria targetting line to cells expressing the pSNAPf-COX8 construct by staining the mitochondria line with Mitotracker and BG-BODIPY. Again, we found a significant colocalisation of the two dyes (Figure 3.11) (Overlap Coefficient=0.986 r^2= 0.971), demonstrating that BG-BODIPY is able to target to SNAP-tag enzyme expressed at the AAVS1 site, as well as by a CMV promoter.

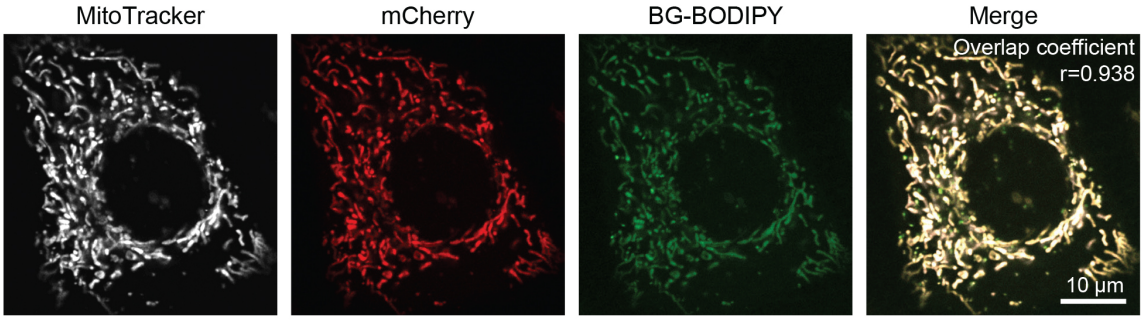

Figure 3.11: **BG-BODIPY targets to organelles expressing SNAP-tag with targeting sequences from the AAVS1 site.** Colocalization of Mitotracker with A. mCherry and BG-BODIPY targeted to the mitochondria via residues 1 to 29 of HsCOX8 (Overlap Coefficient=0.938 r^2=0.879).

Next, we labelled all seven knock-in lines with BG-BODIPY and made ratiometric measurements on the Zeiss LSM880 with Airyscan by comparing the relative intensity of the BG-BODIPY signal to the mCherry signal (Figure 3.12). This assumes a 1:1 proportion of mCherry to BG-BODIPY, which we felt was reasonable given the ability of our backwashing protocol to reduce unincorporated BG-BODIPY levels to that of unlabelled cells. All of the cell lines were labelled and washed as discussed previously prior to imaging.

We observed reported ratios (and thus viscosities) that vary significantly between the various membrane-bound organelles. For instance, the mean ratio value in-

creased from the ER (1.67) to the Golgi (1.76) ($p<0.001$), but the range of the ratio values broadened considerably. The second highest mean ratio, after the Golgi, was in the mitochondrial matrix (1.70). The lowest of the viscosities reported was in the nucleoplasm (1.45) which was significantly lower than the cytoplasm (1.56) ($p<0.001$). Lysosomes had a mean lifetime slightly less than that of the cytoplasm (1.52), while peroxisomes had an intermediate mean lifetime (1.62), but exhibited by far the largest variance.

These measurements gave us the relative viscosities of the organelles, however we wanted to make absolute measurements of the viscosity in each organelle. This proved significantly more challenging. In order to make a calibration of the ratio, we would need to isolate the mCherry fusion proteins, tag them with BG-BODIPY and introduce the composite bound fluors to glycerol solutions of varying concentration. In order to achieve this, we attempted to lyse the cytoplasmic mCherry knock-in line, both before and after BG-BODIPY labelling, in order to make ratiometric measurements. Unfortunately, the low expression level, so advantageous in not perturbing the behaviour of the living cell, made it impossible to achieve concentrations of the fusion protein in the lysate sufficient to make measurements. Attempting to remedy this, we coated magnetic beads in a polyclonal anti-mCherry antibody (Abcam) and attempted to immuno-isolate a high enough concentration of the fusion protein to image by introducing the beads to the lysate. While this approach delivered a modest enrichment of the labelled fusion protein, it was still insufficient for accurate measurement, especially of the FLIM signal.

3.2.9 mCherry lifetime dominates BG-BODIPY in FLIM images

In order to make absolute viscosity measurements in the organelles, we attempted to make FLIM images of BG-BODIPY targeted to the various organelles in the mCherry/SNAP-tag lines. When we analysed the images, however, we found that all of the lifetime histograms were nearly identical, with a bimodal distribution with peaks at ~700ps and ~1600ps. We began to believe mCherry was being excited by the pulsed 488 laser such that its emission dominated the lifetime histogram.

To test this, we bleached the mCherry signal with the 559 laser prior to labelling with BG-BODIPY and then made further FLIM measurements. While there was some recovery of the mCherry signal following bleaching (Figure 3.13), likely due to de novo synthesis or folding of nascent fusion proteins after the photobleach,

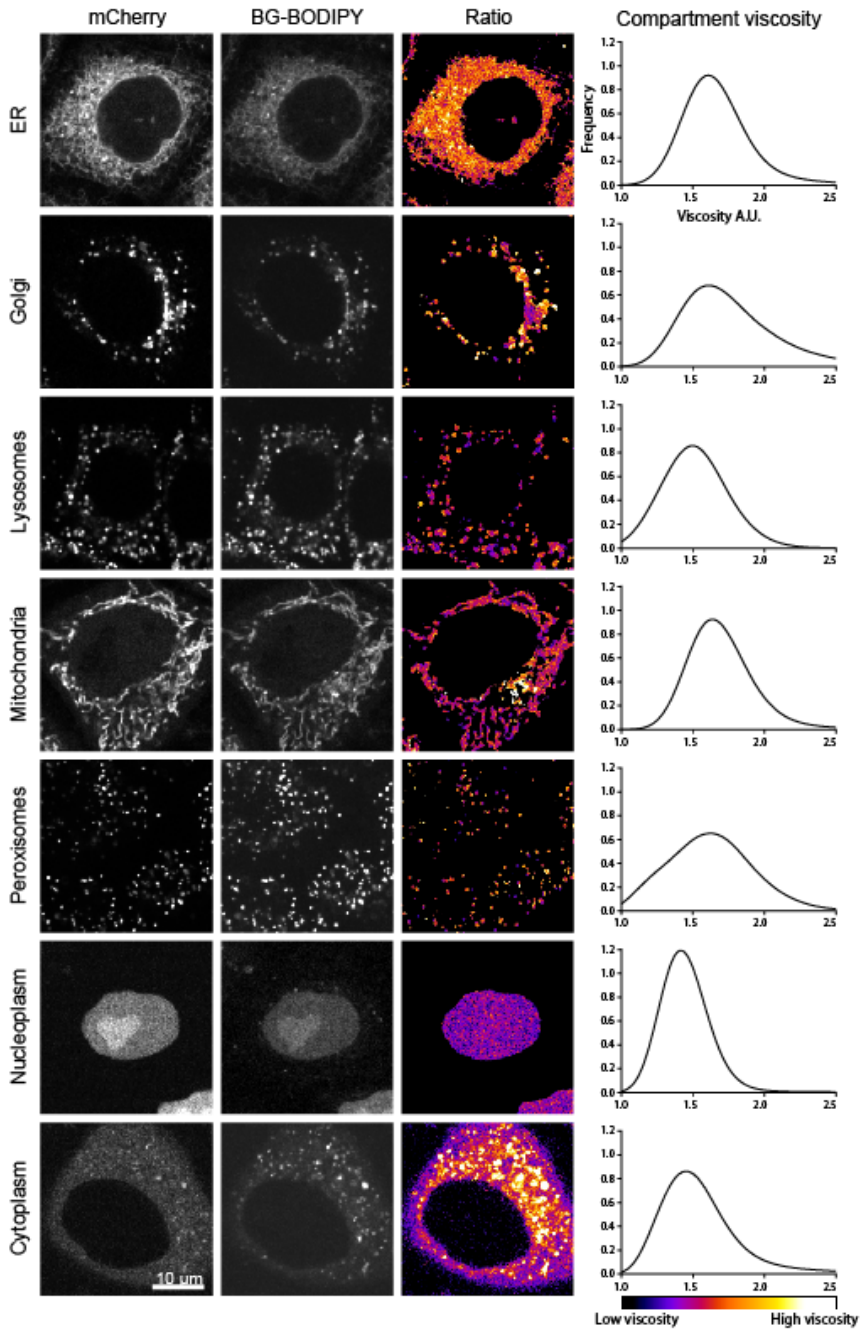

Figure 3.12: **mCherry-BG-BODIPY can be targeted to all cellular compartments and reports relative microviscosity.** The viscosity is highly variable in different cellular compartments. The mCherry-SNAP-Tag fusion protein targeted to distinct cellular compartments was constitutively expressed from the AAVS1 locus and and tagged with BG-BODIPY by subsequent incubation with the probe. Ratiometric analysis of the fluorescence intensity of mCherry and BODIPY enabled us to assess the compartment viscosity. The analysis shown is based on 3 experimental replicates of approximately 40 to 50 cells each.

the bleaching appeared to ameliorate the constant lifetime (Figure 3.14). We then made FLIM measurements once more for each of the cell lines. Unfortunately, as it turns out, in some of the lines, particularly the plasma membrane and nucleoplasm, the levels of expression meant the BG-BODIPY signal was too dim to collect enough photons to make FLIM measurements with any confidence.

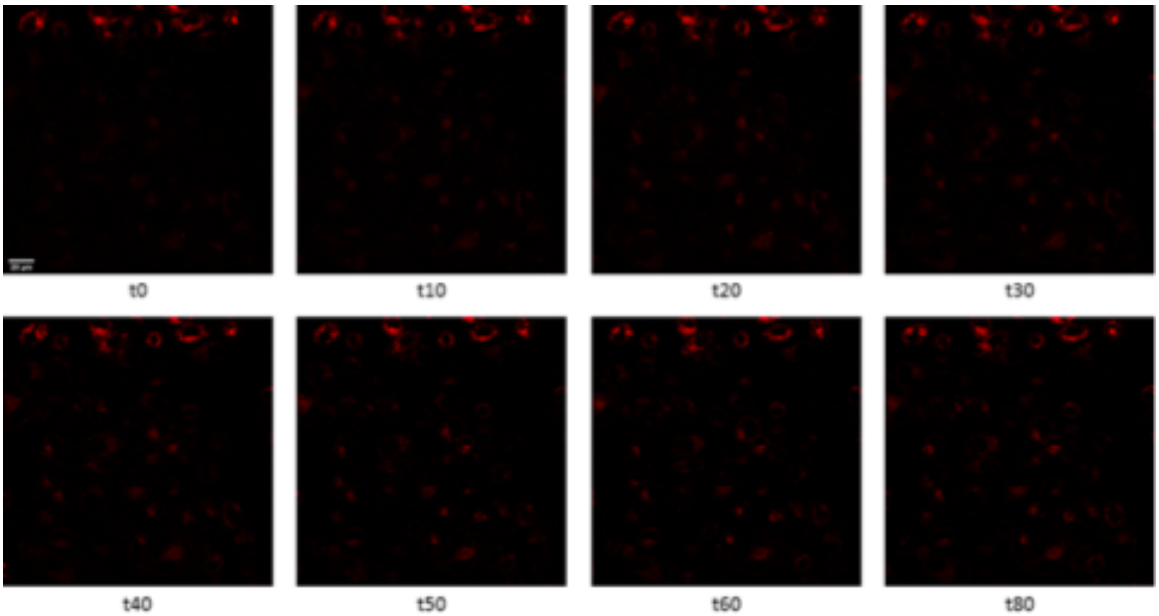

Figure 3.13: **Fluorescence recovery of mCherry after bleaching.** Images show a time course of the mCherry/SNAP-tag line that targets to the ER. A large square area in the bottom portion of each field of view has been bleached by the 559 laser, while a strip at the top has been left unbleached for reference. Recovery was measured for 80 minutes, or roughly the amount of time it took to stain cells with BG-BODIPY following bleaching and set them up on the Olympus for imaging.

3.2.10 BG-BODIPY can discriminate microviscosities in different sub-compartments of the same organelle

We became aware after having made our FLIM measurements of the mCherry/SNAP-tag fusion mitochondria targeting line that this line and the COX8/SNAP-tag construct target BG-BODIPY to distinct locations within the mitochondria. Whereas the mitochondrial localisation signal in the mCherry line targets SNAP-tag to the mitochondrial matrix, the COX8 construct results in SNAP-tag localisation to the intermembrane space (Figure 3.15a).

To confirm this, we drew linear regions of interest across the Airyscan images of

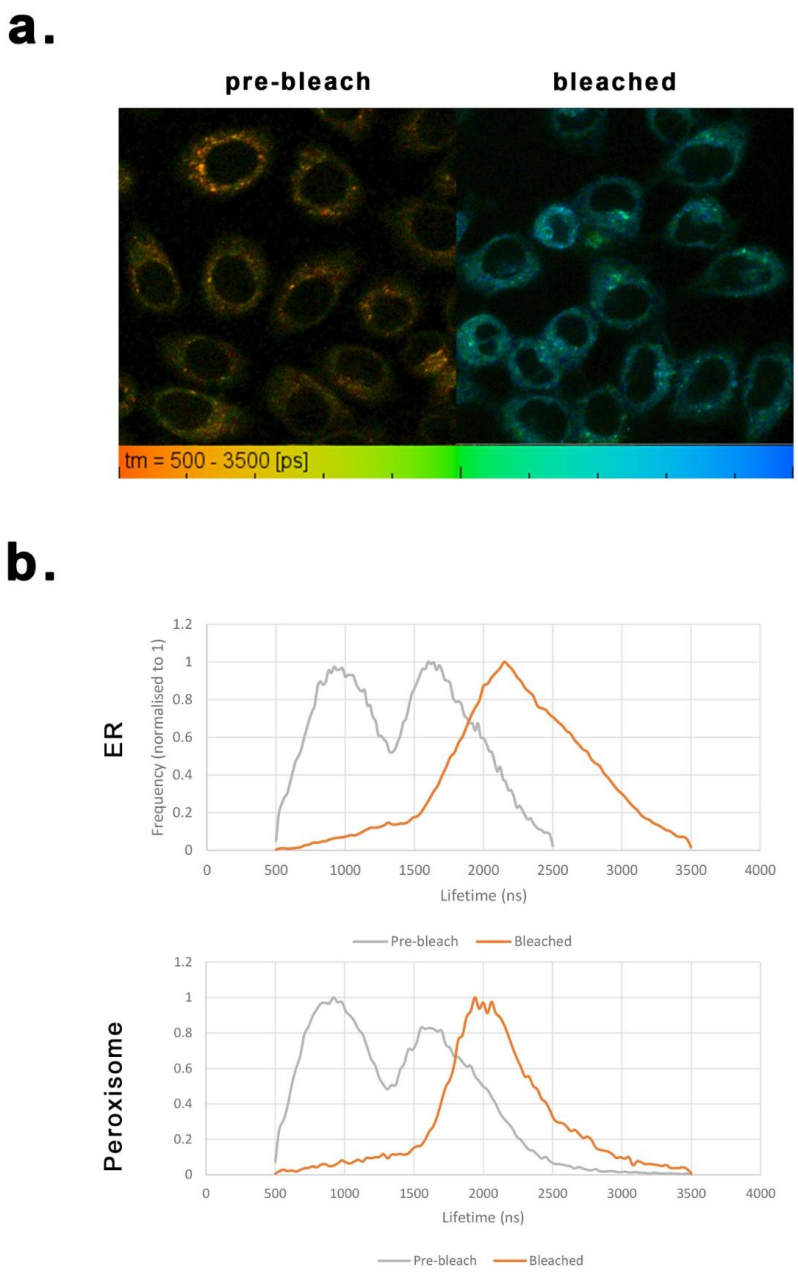

Figure 3.14: **Effect of bleaching of mCherry on the BG-BODIPY lifetime.** a. FLIM images of mCherry/SNAP-tag targeted to the ER labelled with BG-BODIPY. The left hand image was taken without the mCherry having been bleach while the right hand image was acquired post bleaching. b. A comparioson of the lifetime histogram of cells targeting mCherry and BG-BODIPY to the ER and peroxisomes prior to and after bleaching.

BG-BODIPY signal in mitochondria expressing either of the fusion proteins (Figure 3.15b) and analysed the lines' intensity profiles. Consistent with our predictions, the COX8/SNAP-tag construct showed two peaks of intensity along the line, whereas the mitochondrial localisation signal cell line showed a single peak. This is in line with the former localising BG-BODIPY to the intermembrane space of the mitochondria and the latter localising it to the matrix in the centre of the organelle.

The next obvious question was to determine whether we could detect differences in the reported microviscosity between these two compartments. We compared the reported viscosity histograms derived from FLIM images made for both the cell line and HeLa cells expressing the COX8/SNAP-tag construct, aware that we were comparing two disparate expression systems. While FLIM allows us to ignore any difference in concentration of BG-BODIPY, we cannot rule out the possibility that transient overexpression of COX8/SNAP-tag somehow alters the microviscous environment of the intermembrane space. We found that the BG-BODIPY targeted within the mitochondrial matrix reported a much higher viscosity than that targeted to the intermembrane space by transient expression (Figure 3.15c).

3.2.11 BG-BODIPY can target to and measure viscosity in membraneless organelles

Up to this point we have focused primarily on membrane-bound organelles, however there is a growing body of work on nontraditional, membraneless organelles. One such organelle, stress granules, comprises inducible, cytoplasmic granules composed of an mRNA scaffold and RNA binding proteins (RBPs). Stress granules have become of particular interest due to their relationship with disease (Li *et al.*, 2013). Normally, stress granules form through a process of liquid-liquid phase separation, and sequester untranslated mRNAs in order to selectively stop translation during periods of stress (Protter & Parker, 2016). Many of the same RBPs that comprise stress granules have, in addition to an RNA-recognition motif (RRM), a prion-like domain, the former allowing them to bind mRNA while the latter gives them the ability to rapidly self-associate into fibrillar structures in order to form stress granule hydrogels (Li *et al.*, 2013). However, rapid self-templated assembly is a double edged sword and its misregulation is associated with numerous disease states.

Recent work by Richard Wheeler in the Dunn School has focused on finding compounds to modulate the physical chemistry involved in stress granule formation

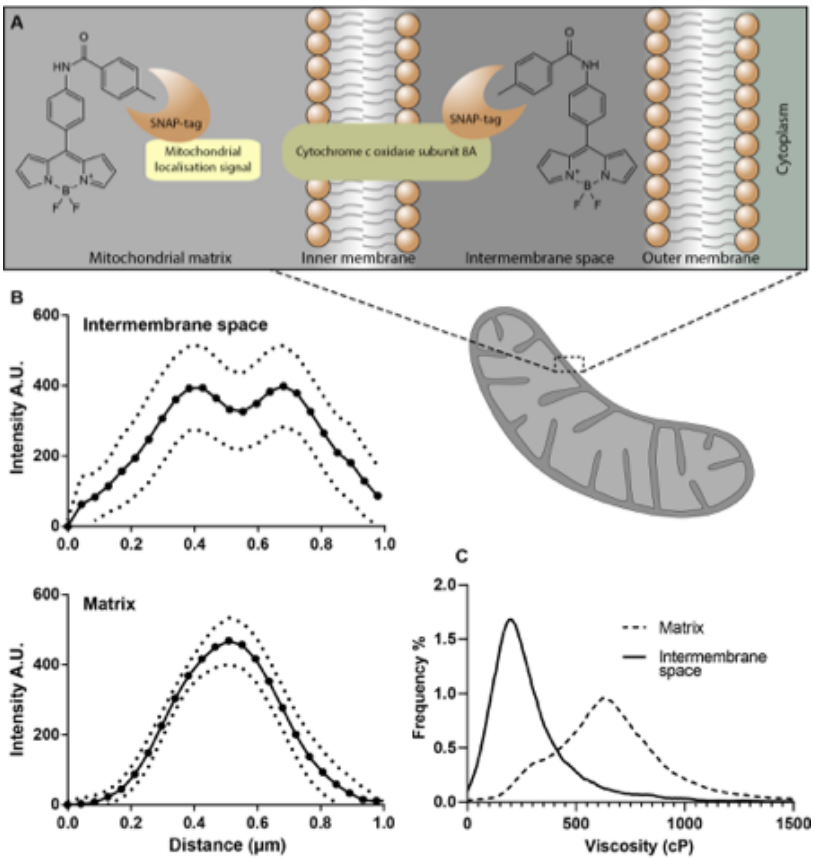

Figure 3.15: **BG-BODIPY reports microviscosity in sub cellular compartments.** a. Diagram of BG-BODIPY localisation in the mitochondrial matrix and mitochondrial intermembrane space. b. Intensity profiles orthogonal to mitochondrial edges showing the single and double peaks of intensity confirming the correct localisation of BG-BODIPY. c. A histogram showing the viscosities reported from FLIM analysis of BG-BODIPY bound to the Cox8/SNAP-tag fusion protein or in the mitochondrial matrix. Mean viscosity for intermembrane space and matrix are respectively 309 cP and 600 cP.

(Wheeler & Hyman, 2018; Wheeler *et al.*, 2019). In an impressive screen, 1600 medical compounds were tested to see if they impacted FUS-GFP localisation to stress granules in HeLa cells stressed with sodium arsenate (Wheeler *et al.*, 2019). From this screen they discovered three classes of compounds that affected FUS-GFP localisation in stressed cells and in droplets formed *in vitro*: heterotri- and tetracyclic compounds, surfactants and lipoamide. Of these, they decided to compare lipoamide and its closely related compound lipoic acid with the more broadly active heterotricyclic compound mitoxantrone. They found lipoamide both reduced stress granule formation in cells and promoted FUS's return to the nucleus, reduced FUS aggregation in cells and animal models, and reduced the pathological

phenotype of neurons and animals expressing mutant FUS. In contrast with mitoxantrone, lipoamide had a specific effect on stress granules and not other membraneless organelles.

TDP-43 is something of a pet interest for me; my initial project in the Dunn School before I switched lab groups was meant to be on TDP-43 and R-loops. So when we decided to test BG-BODIPY's ability to investigate membraneless organelles, my mind immediately jumped to TDP-43 and stress granules. To achieve this, we generated a construct containing SNAP-tag fused to a C-terminal fragment of the TAR DNA-binding protein 43 (TDP-43) that lacks the RRM domains and is not itself prone to aggregation in physiological circumstances. We expressed this construct in HeLa cells and labelled these cells with 2.5µM BG-BODIPY. BG-BODIPY was primarily localised to the nucleus, where we would expect to find TDP-43 under physiological conditions. When the lifetime of BG-BODIPY in the nucleus was measured by FLIM, we found the mean viscosity to be 185cP (equivalent to the viscosity of 87.7% glycerol) (Figure 3.16a).

$ZnCl_2$ has been shown to induce the formation of TDP-43 inclusions in the cytoplasm, and has been used to model pathological aggregation of the protein (Caragounis *et al.*, 2010). Therefore, we used $ZnCl_2$ to induce stress granules in HeLa cells expressing the TDP-43/SNAP-tag fusion protein. When cells were treated with 100µM $ZnCl_2$ overnight, a treatment shown to elicit robust TDP-43 aggregation, we observed distinct populations of foci in the cytoplasm, demonstrating that the truncated TDP-43 is sequestered to stress granules upon oxidative stress (Figure 3.16b). There was wide variation in the viscosities reported from within the stress granules, however we found that the mean viscosity was ~500cP, a large increase from TDP-43's nucleoplasmic microviscous environment.

To ensure these puncta were indeed stress granules, we expressed the C-terminal TDP-43 fragment tagged with GFP in HeLa cells. We once again treated cells overnight with 100µM $ZnCl_2$ and observed the same cytoplasmic puncta. We then treated these cells with 10µM mitoxantrone and 10µM lipoamide to see if they reduced the number of size of the puncta. We observed that mitoxantrone treatment led to a near complete reduction of stress granules after an hour and a half (Figure 3.17).

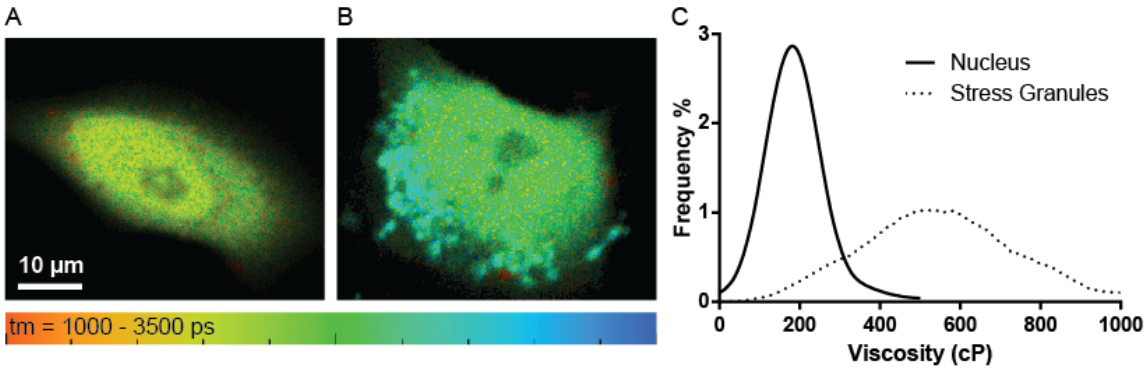

Figure 3.16: **BG-BODIPY targets to and measure viscosity in membraneless organelles.** a. C-terminal fragment of TDP43 labelled with BG-BODIPY targets to the nucleoplasm plus a diffuse cytoplasmic signal. b. In the presence of $ZnCl_2$ TDP43 forms cytoplasmic condensates. c. the microviscosity of stress granules is significantly higher to the nucleoplasm and cytoplasm.

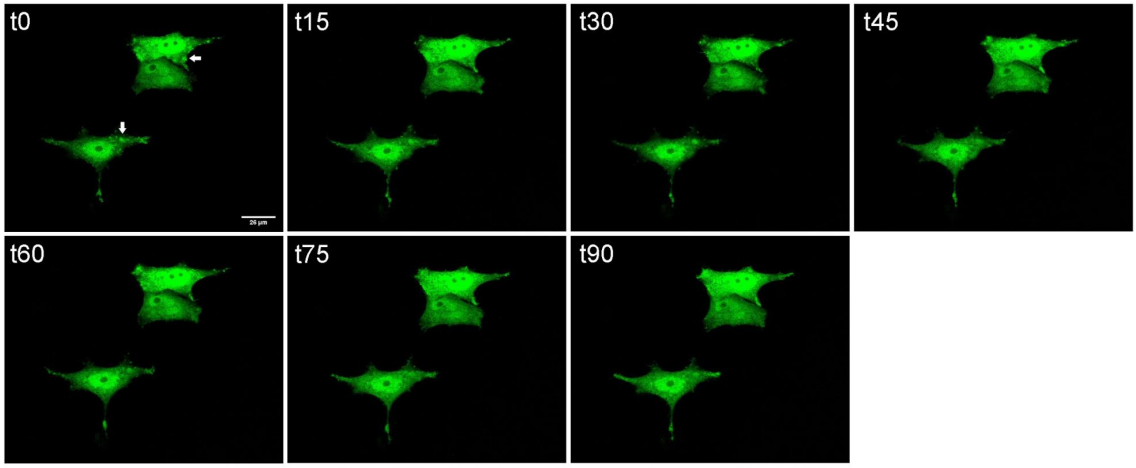

Figure 3.17: **Mitoxantrone dissolves TDP-43/GFP containing cellular condensates.** Cells that had been treated overnight with $ZnCl_2$ induce the formation of TDP-43/GFP positive cytoplasmic condensates (large examples are highlighted with white arrows), were treated with mitoxantrone. Condensates have nearly disappeared after 90 minutes of treatment.

3.3 Discussion

In this chapter, we have shown that BG-BODIPY is a suitable molecular rotor probe for measuring microviscosity within living cells. BG-BODIPY is responsive in both fluorescence yield and lifetime to changes in viscosity and has wide enough dynamic range to make meaningful viscosity measurements in a cellular. Further, the fluorescence lifetime is pH insensitive, indicating that it can accurately report

microviscosity across the range of cellular pHs it might encounter.

We then demonstrated the usefulness of a pair of complementary techniques for measuring viscosity of discrete subcellular locations in living cells. Whilst numerous previous attempts to target molecular rotors in living cells have relied on exploiting the unique properties of given organelles (e.g. Song *et al.*, 2016; Su *et al.*, 2016), our work represents one of the first attempts at using a common mechanism to target BODIPY to every organelle. We measured the relative viscosities of a host of organelles, as well as showcasing the BG-BODIPY's prospects for measuring absolute viscosity in both membrane-bound and membraneless organelles. We did so by CRISPR-Cas9 engineering the AAVS1 genomic locus in human cells to express the mCherry/SNAP-tag fusion protein targeted to multiple subcellular locations.

FLIM is a powerful technique that provides measurements of molecular rotor fluorescence lifetime, and thus microviscosity, that are independent of probe concentration, but it has several practical limitations. Acquisition of FLIM images occurs over the order of minutes, with weaker signals requiring the longest acquisition periods. This precludes the use of FLIM for capturing fast changes in viscosity. FLIM is also limited in most experimental systems to conventional confocal resolution, or at best two photon microscope resolution. This issue may be experimentally ameliorated by the selective targeting of the reporter via expression of organelle-specific fusion proteins bearing the SNAP-Tag enzyme. Further, FLIM requires specialised, expensive equipment not available to most labs. In contrast, using BG-BODIPY with the ratiometric CRISPR cell lines allows us to visualise viscosity changes at high resolution and over short periods, and can be measured using standard confocal microscopes, however it has its own limitations. For instance, the ratiometric technique thus far can only give relative viscosities, not absolute values, although this can be overcome by appropriate calibration experiments, which we suspect should work as the graph surface of FLIM lifetime/intensity ratio is flat for a wide range of pH and viscosity values. Thus, these two approaches represent complementary techniques that we offer together as additions to researchers' toolkits, each to be used situationally.

By using BG-BODIPY in these two methods, we were able to demonstrate its usefulness in probing the microviscous environments of the living cell. We showed that there is significant variation in both the mean and the range of the viscosities seen within various cellular organelles. Of particular note is the change as one

moves along the secretory pathway. Not only does the mean ratio between BG-BODIPY and mCherry increase from the ER to the Golgi apparatus, but there is also a progressively wider range of viscosities reported as one proceeds along the secretory pathway. We interpret this to mean that the microviscous environment becomes more varied later in the secretory pathway. Whilst the cause of this variation within an organelle later in the secretory pathway is unclear, it is tempting to consider whether this may be related to the formation of subdomains within later secretory organelles that facilitate separation of cargo with different destinations (secretory granule, constitutive secretion, shuttle vesicle to endocytic pathway). This represents a potential physiological role for liquid liquid phase separation in cargo sorting in the secretory pathway would offer a novel paradigm in molecular cell biology.

In addition, we have been able to compare the viscosity values reported here with those obtained in other labs, especially those using widely distributed molecular rotors, or those targeted by over-expression to a limited range of organelles. Our viscosity ratios were in keeping with Chambers *et al.* (2018), with the mitochondria having significantly higher mean viscosity than all organelles other than the Golgi apparatus, which they did not measure. By using FLIM we were able to determine that the absolute viscosity within the mitochondrial lumen was 309 cP. Chambers *et al.* (2018) found the viscosity within the mitochondrial lumen to be 325cP, so our viscosity values are concordant, highlighting the replicability of this technique. However, our viscosity ratios in the cytoplasm and nucleoplasm were not in concurrence with their measurements, as our probe reported a lower viscosity in the nucleoplasm than the cytoplasm. To account for this, we note that previous attempts have relied upon an untargeted probe that was allowed to spread throughout the cell, whereas our probe was targeted to the nucleus or cytoplasm via either an NLS or and NES, respectively.

Beyond membrane-bound organelles, we demonstrated that by targeting BG-BODIPY to proteins involved in forming membraneless organelles we could make measurements of the change in viscosity as these organelles formed through LLPS. We chose to examine TDP-43 positive stress granules because they represent a pathologically relevant instance of liquid-liquid phase separation. It is thought that the concentration of TDP-43 into stress granules can lead to mis-aggregation of the protein, as seen in numerous neurodegenerative diseases (Parker *et al.*, 2012). The

ability to measure the microviscous environment of TDP-43 in a variety of physiological and disease conditions could lead to important discoveries as to how to prevent its cellular toxicity. What is more, by applying this technique to proteins involved in other membraneless organelles, we could potentially gain key insight into how cells organise themselves through phase separation.

Chapter 4

Using BG-BODIPY to probe the nuclear pore complex

4.1 Introduction

4.1.1 The nuclear pored complex: structure and function

Despite the explosion of complexity the compartmentalisation of the eukaryotic cell allowed, as I've covered in Section 3.1, this partitioning led to its own series of challenges that had to be overcome by the cell. In particular, how does the eukaryotic cell move substrates, metabolic intermediates, nascent structural components, or transduce signals between organelles in a specific and efficient manner?

The defining feature of eukaryotic cells is the presence of a nuclear envelope (NE): two concentric membranes (the outer and inner nuclear membranes (ONM and INM)) that envelop the nucleus, the outermost being contiguous with the membrane of the lumen of the endoplasmic reticulum (ER). The NE acts to segregate nuclear and cytoplasmic material, and yet vital cell processes require extensive nuclear-cytoplasm trafficking and, thus, the constant but controlled breach of this barrier. The selective permeability of the NE is exclusively mediated by the nuclear pore complex (NPC), a massive glycoprotein complex - ~125 MDa in vertebrates (Reichelt *et al.*, 1990) - that spans the NE and creates an aqueous channel that bridges the cytoplasm and the nucleoplasm. The NPC allows for the passive transfer of small molecules (<40 kDa), but larger molecules (both protein and RNA) must be selected for and actively transferred between the nucleoplasm and cytoplasm and vice versa (Peters, 2009). This unique property of the NPC is reflected in its structure.

Though they differ in size and area density in the NE, NPCs are conserved over a vast array of eukaryotes, sharing, broadly, the same structure (Grossman, Medalia & Zwerger, 2012), and were likely to be present in the last eukaryotic common ancestor (LECA) (Neumann, Lundin, & Poole, 2010). The vertebrate NPC grossly resembles a cylinder ~125 nm across and 70 nm high with eight-fold symmetry around eight asymmetric 'spokes' that extend into the centre of the cylinder to form a central channel with a diameter of ~50 nm (Peters, 2009). At the centre of the cylinder is a 12 MDa 'central plug,' of low electron density and contentious composition (Riechelt *et al.*, 1990). Despite the enormous size of the complex, it is composed of multiple copies of relatively few proteins (~30), which are collectively termed the nucleoporins (nups) and are widely conserved across the eukaryotic taxon (Neumann, Lundin, & Poole, 2010).

Reflecting the eight-fold symmetry of the complex, each nup is repeated in the structure 8, 16, 32, or 48 times (Cronshaw *et al.*, 2002). There is a surprising economy of secondary structures represented in the structure of the nups. Of the total nup amino acids, 38% are devoted to α-solenoid folds, 29% to FG- repeats, and 16% to β-propellor folds, with no other fold type representing more than 5% of the remaining amino acids (Devos *et al.*, 2006). The nups can be classified based on their structure and location within the NPC into five distinct groups (Devos *et al.*, 2006), the proposed collective functions of which have shed light on the workings of the NPC on the whole. These are the membrane nups, which use their transmembrane domains to anchor the complex to the NE; the scaffold nups, responsible for giving the NPC its shape and linking the membrane nups to the barrier nups; the barrier nups that mediate the selective barrier function of the NPC; and the cytoplasmic filament and nuclear basket nups that form filamentous structures at the cytoplasmic and nuclear poles of the NPC, respectively, and provide docking sites for transport complexes (Grossman *et al.*, 2012).

4.1.2 Barrier nucleoporins

Of particular importance to the selectivity barrier function of the NPC are the nucleoporins that contain 'FG domains,' defined by the presence of multiple repeats of Phe-Gly motifs containing the amino acid sequence GLFG, FxFG, SxFG, or PxFG (where x is any residue) (reviewed in Grossman *et al.*, 2012), which form intrinsically disordered regions (IDRs) - regions that fail to form stable secondary structures but can still perform biological functions (Oldfield & Dunker, 2014). Verte-

brate NPCs contain ~11 FG nups, which vary primarily by their anchoring points in the NPC and the surrounding sequences of their FG motifs (Schmidt & Görlich, 2016). Collectively, they are distributed throughout the entirety of the NPC channel and at the ends, primarily anchored to the inner ring scaffold structure of the NPC or to the linker nups (Alber *et al.*, 2007). However, individually their localisation in the NPC is variable. For example, the yeast nup145 has an autoproteolytic function that produces two proteins, nup145N (hnup98) and nup145C (hnup96), the former of which is found mostly at the nuclear end of the NPC whereas the latter is bound evenly along the channel (Teixeira, Fabre, & Dujon, 1999).

The evidence that FG domain containing Nups are the molecular basis of the NPC's selectivity barrier is rather robust. Knock out studies have demonstrated that FG domains are either lethal (Strawn *et al.*, 2004) or result in a significant reduction in the permeability barrier in both S. cerevisiae (Patel *et al.*, 2007) and Xenopus eggs Hülsmann *et al.*, 2012). Infection with poliovirus, which proteolytically cleaves three FG domain-containing nups - nup98, nup153, and nup62 -, results in disrupted nuclear trafficking and leakage of nuclear proteins into the cytoplasm (Park *et al.*, 2008). Further, FG domains directly bind to nuclear transport receptors (NTRs) (e.g., Iovine, Watkins, & Wente, 1995), a fact that has greatly shaped the development of models of transport through the NPC (more below).

This FG domain binding interactions with NTRs are relatively weak (Bayliss *et al.*, 1999; Chaillan- Huntington *et al.*, 2000; Ribbeck & Görlich, 2001), but are essential for the translocation of NTRs through the NPC. A given NTR is capable of binding to multiple FG Nups, but will have a strong preference for a small number of the Nups (Grossman *et al.*, 2012). This is thought to limit the competition for occupancy between NTRs, allowing for multiple NTRs to bind simultaneously. There are roughly 160 NTR binding sites in each NPC (Ryan & Wente, 2000), and NPCs have been shown to be capable of facilitating export and import simultaneously (Dowretzky, Landford, & Feldherr, 1988).

4.1.3 Models of NPC selective barrier function

How, then, does the NPC function to facilitate transport of certain proteins larger than 40kDa but not others? Any answer must take into account the behaviour of the FG Nups, particularly their interactions with NTRs and themselves described above. Many models have arisen to explain this selectivity, though many are deeply flawed. For the sake of brevity, this review will consider the two most

plausible models of transport selectivity, the selective phase model and the virtual gate model.

The virtual gate model asserts that translocation through the NPC is precluded for inert molecules due to an entropic barrier created by the physical constraints placed on a molecule entering a constricted space (Rout *et al.*, 2003) (Figure 4.1) In this model, the FG Nups extend into the centre of the channel to formed a polymer brush. The FG Nup chains could be displaced, but this would be energetically unfavourable, adding to the entropic barrier. The model states that in order to cross this barrier a molecule needs to enter a 'transition state,' which in this case would be achieved through binding to the FG domains. In this sense, the model considers the NPC a 'translocation enzyme.' It has been shown that high density polymer brushes are capable of repelling macromolecules (Piehler *et al.*, 2000), but the model has several glaring flaws. Firstly, the model relies on the assumption that cohesive domains are nonessential for selectivity, however reconstituted NPCs containing Nup98 with only non-cohesive FG domains show a drastic loss of selectivity (Hülsmann *et al.*, 2012). Furthermore, the flexibility of the peptides would ensure that they were only effective barriers near to their sites of attachment (<1 nm away), rendering the centre of the channel highly permeable (Schmidt & Görlich, 2016).

The selectivity phase model posits that the identity of the central plug is a homogenous, semi-liquid phase comprising a meshwork of FG Nups held together by the weak interactions between their Phe-rich domains (Ribbeck & Görlich, 2001). NTR binding to FG domains then disrupts their homotypic interactions, endowing NTRs (and their associated proteins) with an increased solubility in the phase compared to molecules incapable of FG domain binding, and allowing for their translocation through the plug. Molecules small enough to intercalate the gaps in the FG Nup network would be capable of passing through the central plug via passive diffusion, in accordance with observed behaviour. Beyond just a physical barrier, the meshwork could also prevent certain molecules from entering due to their hydrophilic nature. The concentration of FG domains, which are hydrophobic, in the central plug is estimated to be around 50 mM (Bayliss *et al.*, 1999), which would force the local water molecules into a more ordered state. According to the model, this would make it energetically unfavourable for molecules without hydrophobic surface like those found in NTRs to enter the pore (Ribbeck & Görlich, 2001).

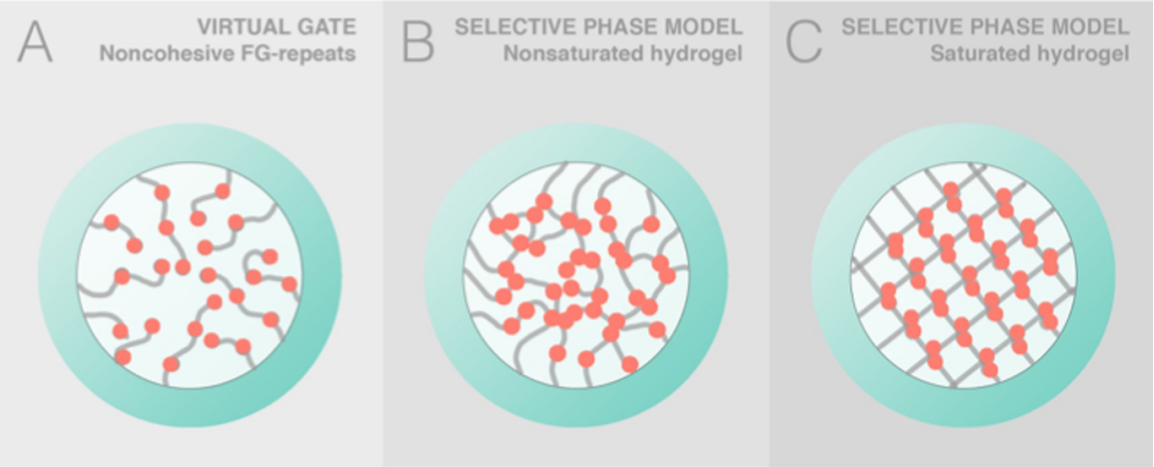

Figure 4.1: **Models of NPC selective permeability barriers.** a. The virtual gate model, in which FG-nups act purely as an entropic barrier. b. And c. show variations on the selective phase model in which the hydrogel is nonsaturated and saturated, respectively.

This model makes sense given the translocation kinetics of various molecules through the NPC. Nuclear transport factor 2 (NTF2), which mediates the nuclear import of Ran, is capable of passing through the NPC 120 times faster than an inert reference molecule (GTP), yet still translocates at a speed four times slower than what is projected for a molecule assuming the central channel is filled with simply an aqueous solution (Ribbeck & Görlich, 2001). This would make sense in the context of translocation being facilitated by a transient binding interaction. These predicted cohesive FG domain interactions have been verified with the bead halo assay, in which affinity-tagged proteins are immobilised on beads and introduced to solutions containing fluorescent macromolecules to see if they interact (Patel *et al.*, 2007), and it has proved possible to construct monolayer films of FG domains that mimic the behaviour of an FG domain mesh (Eisele *et al.*, 2010). Finally, and perhaps most convincing, it has been demonstrated in numerous studies that isolated FG domain proteins and derived peptides, both from yeast and vertebrates, can be reconstituted *in vitro* to form hydrogels with selective permeabilities similar to those of the pore *in vivo* (Frey & Görlich, 2007; Frey & Görlich, 2009; Milles & Lemke, 2011; Labokha *et al.*, 2013), excluding molecules as small as mCherry (28.8 kDa).

Several other models exist to explain the role of FG domains in mediating selectivity of the NPCs, including the Kap-centric model and the ring cycle model (reviewed in Schmidt & Görlich, 2016), but all suffer from inconsistencies. Thus,

whilst far from confirmed, the selectivity phase model seems most in line with the evidence for the moment.

In this chapter, we saw an opportunity to utilise BG-BODIPY to probe the NPC and determine what phase the proteins occupying the central channel exist in. This was meant to be the central thrust of my thesis; in fact, BG-BODIPY was created with the intention of answering this particular question. As you have probably gathered from the structure of this thesis, this proved to be less than straightforward.

4.2 Results

4.2.1 BG-BODIPY detects changes in microviscosity during IAPP gelation

It occurred to us early on in this project that, although it would be easy enough to calibrate BG-BODIPY's viscosity response, it would be very difficult to determine what lifetime was representative of the microviscous environment of a hydrogel. Short of recreating an FG-Nup hydrogel with the precise relative concentrations and spatial arrangement of the different FG-Nup proteins in the NPC, it was difficult to conceive of what sort of baseline we would be able to compare to our measurements *in vivo*.

Whatever comparison we made would likely be imperfect. Knowing this, we decided to take advantage of some convergent research being done by a postdoc in the lab, Letitia Jean. Letitia's recent work has focused on the kinetics of islet amyloid polypeptide (IAPP) aggregation and gelation, and the role of air-water interfaces (AWIs) in these processes. IAPP is a 37-amino acid hormone secreted along with insulin by the β-cells of the islets of Langerhans, and its misfolding and aggregation has been associated with the loss of pancreatic β-cells in non-insulin dependent diabetes mellitus type II (NIDDM) (Abedini & Schmidt, 2013). Previous work of hers has shown that IAPP monomers undergo assembly into fibrils and then undergo a solid to gel transition at the AWI, following detailed characterisation of these gels (Jean *et al.*, 2016).

Letitia wanted to use BG-BODIPY to monitor phase separation in this system and make microviscosity measurements of the gels formed in the gelation process she had previously characterised over a large scale. I was looking for another biological

hydrogel in which to test BG-BODIPY, and this seemed to be a convenient means to do so.

In order to observe the AWI in 96-well plates on the Olympus FV 1000, a new experimental set up had to be devised, as the AWI of the solution at 10x was too far from the objective. To adjust for this, we filled the well with more solution so that the AWI was close to the top of the well, and then the well was sealed with silicone vacuum grease and a borosilicate glass coverslip (24x50 mm, thickness No 1) so that after incubation, we could invert the plate and image the AWI from upside down.

We were uncertain as to whether BG-BODIPY would even associate with IAPP in order to monitor its assembly. 3.6 mM IAPP was incubated with 0.4 mM bIAPP-0.08 mM avidin D Texas red, and with either 5.56 mM BG-BODIPY or green fluorescent beads, and z-stacks were collected of the AWI for 18 hours (Figure 4.2). BG-BODIPY clustres (green) overlapped significantly with the IAPP clusters (red) (overlap coefficient = 0.748), with 97.4% of BG-BODIPY colocalising with bIAPP. However, only 49.5% of bIAPP colocalised with BG-BODIPY. The green beads also colocalised with the IAPP (overlap coefficient = 0.821), however double-labelled structures were frequently found to have single-labelled features, and only 33.7% of beads colocalised with bIAPP, and 23.8% of bIAPP colocalised with beads. We took this to mean BG-BODIPY and the beads were reporting from distinct parts of the gelled network, possibly due to variations in the mesh size.

Because in this experimental setup we are unable to wash off the 'excess' BG-BODIPY that had not been incorporated into the gel, we were concerned that the fluorescence lifetime of the free BG-BODIPY would interfere with our measurements. However, we performed FLIM on BG-BODIPY in the nonviscous solution and found no significant lifetime signal, consistent with the lack of signal in the intensity domain. Further, it is possible for BODIPY fluorescence to be quenched by molar concentration of aromatic residues within proteins, particularly Trp and Tyr, but we felt this was unlikely to be an issue with mM IAPP, which possessed only two Phe and one Tyr.

IAPP reactions were incubated with BG-BODIPY for either 5 or 21 hours, in H_2O or D_2O and then the AWI was imaged with FLIM (Figure 4.3). By 5 hours, the gel layer at the AWI should have formed but not matured, while by 21 hours the reaction should have reached equilibrium. Consistent with these macroscopic changes,

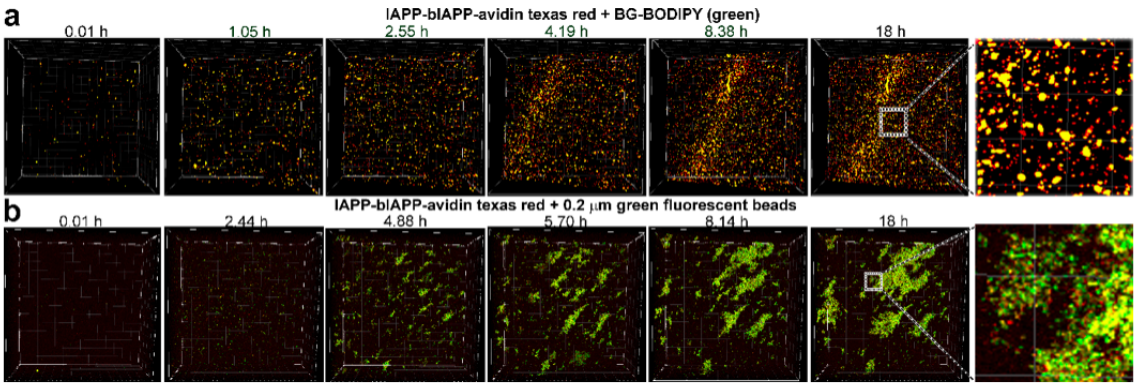

Figure 4.2: **At the AWI, BG-BODIPY or 0.2µm fluoresbrite carboxylate YG beads colocalise with IAPP.** 3.6µM IAPP was incubated with 0.4µM bIAPP-0.08µM avidin D Texas red, and with 5.56µM BG-BODIPY (green fluorescence) (a) or 9.5±0.4x105 0.2µm green fluorescent beads (b) in PBS and H_2O in a well of a 96-well plate. Z-stacks that encompassed the AWI and an area spanning 1417x1417µm^2 were collected for at least 18 h. 3D projections were then visualised with the AWI at the front facing the experimentalist and the bulk solution behind it. Images are snapshots at various time points. The right hand side images are higher mag images of the inset areas at the 18 h time points.

the lifetimes collected from the AWI increased with time. At 5 hours, the peak lifetime in H_2O was ~364 ps and ~383 ps in D_2O (this corresponds to 14.3 and 15.7 cP respectively), while at 21 hours the largest lifetime peak had shifted to ~1498 ps in H_2O and ~2082 ps in D_2O (184.9 and 335.7 cP). The gelation process also resulted in a much narrower range of lifetimes, particularly in the D_2O condition. In every condition, we noticed that the FLIM images reported viscous conditions, not only at the AWI, but extending well into the bulk and sometimes along the edge of the well, suggesting that the gel grew into the solution.

Comparing these values with the viscosity reported in the stress granules from Section 3.2.11, which were much higher (500cP compared with 184.9 and 335.7cP), indicating that hydrogels can vary considerably in the microviscous environment that BG-BODIPY experiences. This makes sense, given that these hydrogels were formed by completely different structures – stress granules comprising a meshwork of RBPs bound to RNA molecules, and IAPP gels being made of fibrils of aggregated protein – and likely having disparate mesh sizes.

There is likely no such thing as a characteristic hydrogel on the microviscous level. There may likely be upper and lower bounds, but it seems there is no BG-BODIPY

lifetime threshold above which the probe is bound up in a gel as opposed to a liquid state.

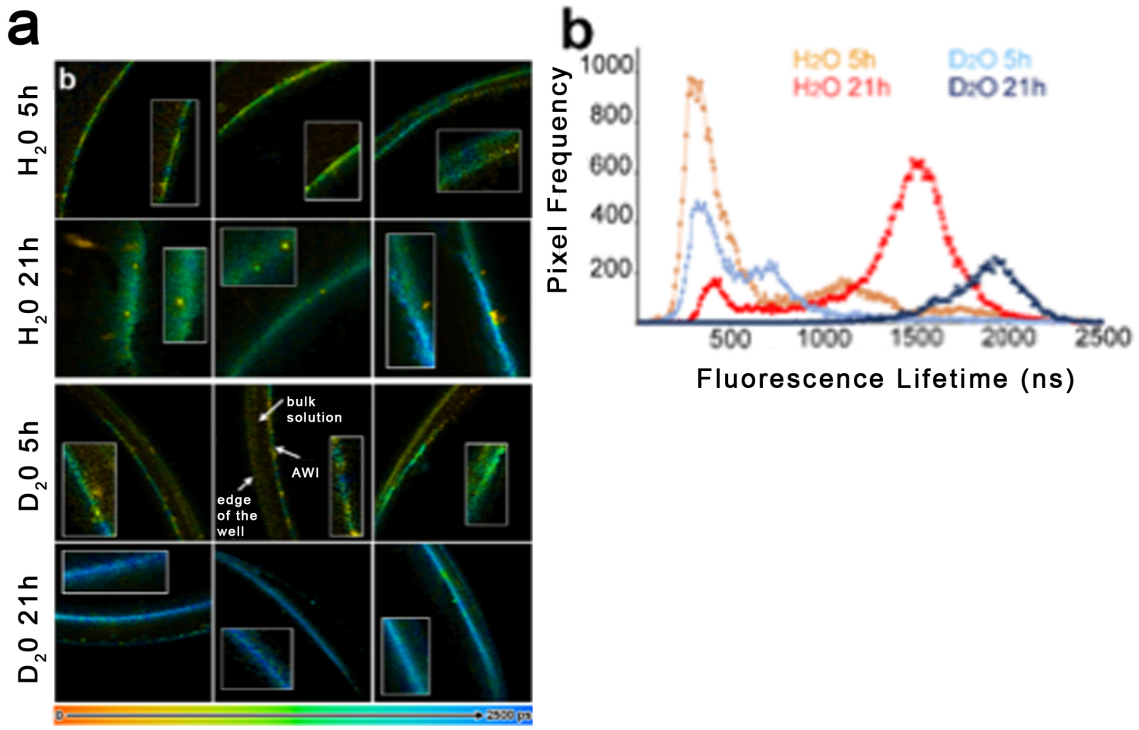

Figure 4.3: **FLIM measurements of IAPP gelation.** a. FLIM images of the AWI region of a 4µM IAPP-5.56µM BG-BODIPY solution, in H_2O or D_2O, at 25°C and 5 or 21 h. Shown in each row are images of three independent replicates per incubation condition. The insets are zoomed in snapshots of the full FLIM images (with the brightness having been increased), which depict representative regions of the AWI that contain several fluorescence lifetime values. The lookup table shows the colour assigned for each fluorescence lifetime value, from red (short lifetime) to blue (long lifetime). b. Fluorescence lifetime histograms of BG-BODIPY in H_2O and D_2O at 5 and 21 hrs.

4.2.2 BG-BODIPY can target to NPCs

The first matter at hand in this set of experiments was demonstrating that BG-BODIPY can penetrate the permeability barrier in order to gain access to the nucleoporin proteins. We weren't seriously concerned this would be an issue, as we had already shown (at least in the chronology I'm presenting in this thesis) that BG-BODIPY can target to the nucleus in the first chapter. However, that was in the presence of a SNAP-enzyme attached to a nuclear localisation signal, so we could not be certain that the probe on its own would gain access to the pore.

In order to initiate this work we were generously provided with two nup/SNAP-tag plasmids from the lab of Ulrich Kubitscheck at the University of Bonn. The group had not published any work with the plasmids because, in their words:

> We planned to visualize the NUP dynamics on the single-molecule level but we encountered several problems. First, transient overexpression of these SNAP-NUPs often resulted in mislocalisation and irregular cellular localisation, e.g. huge nuclear aggregates. Second, the commercial SNAP tag dyes available at that time were far away from usable for single molecule detection. Since we had to use membrane permeable dyes we could not use far-red fluorescence which we usually use to avoid autofluorescence.

Upon transfecting HeLa cells with these constructs it became abundantly clear what they meant. Whilst we were able to label cells expressing nup214/SNAP-tag with BG-BODIPY (Figure 4.4) when we imaged these cells on the Zeiss LSM880 with Airyscan, there were large cytoplasmic fluorescent aggregates, and we were unable to see any expression from the nup153/SNAP-tag construct. Despite this, we were able to clearly see the characteristic punctate nuclear rim pattern indicative of NPCs in the labelled nup214/SNAP-tag expressing cells. We were particularly interested in whether we could resolve individual NPCs, as we were initially going to attempt to determine whether or not individual NPCs varied in their viscosity. As it would transpire, this would not be achievable, as the resolution of the Olympus FV 1000 that the FLIM system is connected to is significantly lower than that of the Zeiss, but grazing images of the top of the nucleus did show individual NPCs (Figure 4.4).

4.2.3 FLIM of transiently expressed FG-nups

We next made FLIM measurements of HeLa cells expressing the nup214/SNAP-tag construct. Because of our inability to observe targeting of BG-BODIPY to the nup153 construct, we did not attempt to make FLIM measurements of this construct. Cells were transfected and allowed to recover for 48 hours before being labelled with BG-BODIPY and washed as previously described. We then we collected FLIM images for >180 seconds. We found that BG-BODIPY reported a peak lifetime of just under 2.3ns, or roughly 366.8 cP (Figure 4.5).

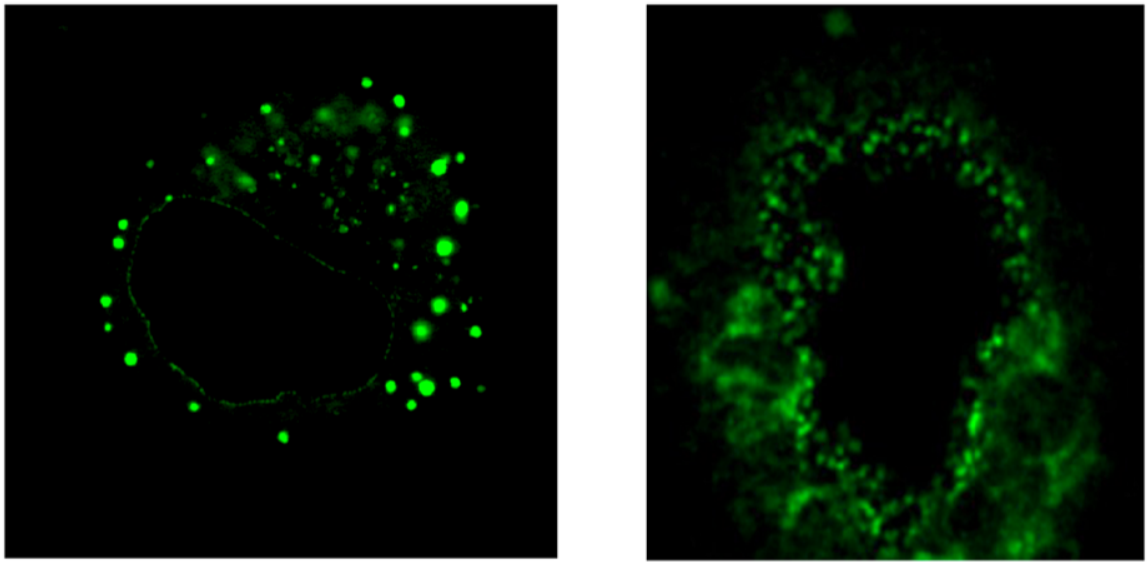

Figure 4.4: **BG-BODIPY targets to transiently expressed nup214.** Two airyscan images of BG-BODIPY labelling in HeLa cells expressing a nup214/SNAP-tag construct. The left hand image is a crosssection of the cell showing the punctate ring pattern typical of NPCs, as well as large cytoplasmic aggregates. The right hand image is a grazing section of the top of the nucleus, showing individual NPCs from above.

(As a brief aside, it is of interest that the aggregates are virtually identical in lifetime to the NPCs at the nuclear envelope. Unfortunately, we do not know enough about the nature of these aggregates to extrapolate much from this. That being said, it is tempting to contemplate the possibility that the overexpression of nup214 leads to an excess of the protein in the cytoplasm that, due to the same properties that allow it to gelate *in vitro*, undergoes LLPS and possibly even gelation within the cytoplasm.)

This suggests that the microviscous environment encountered by the probe attached to nup214 at the cytoplasmic face of the NPC is rather high, higher than either of those of the hydrogels we had attempted to characterise thus far. We were conscious of the fact, however, that this was an overexpression experiment, and we couldn't rule out the possibility that the extra copies of nup214 were hindering rotation of the probe in a non-physiological manner.

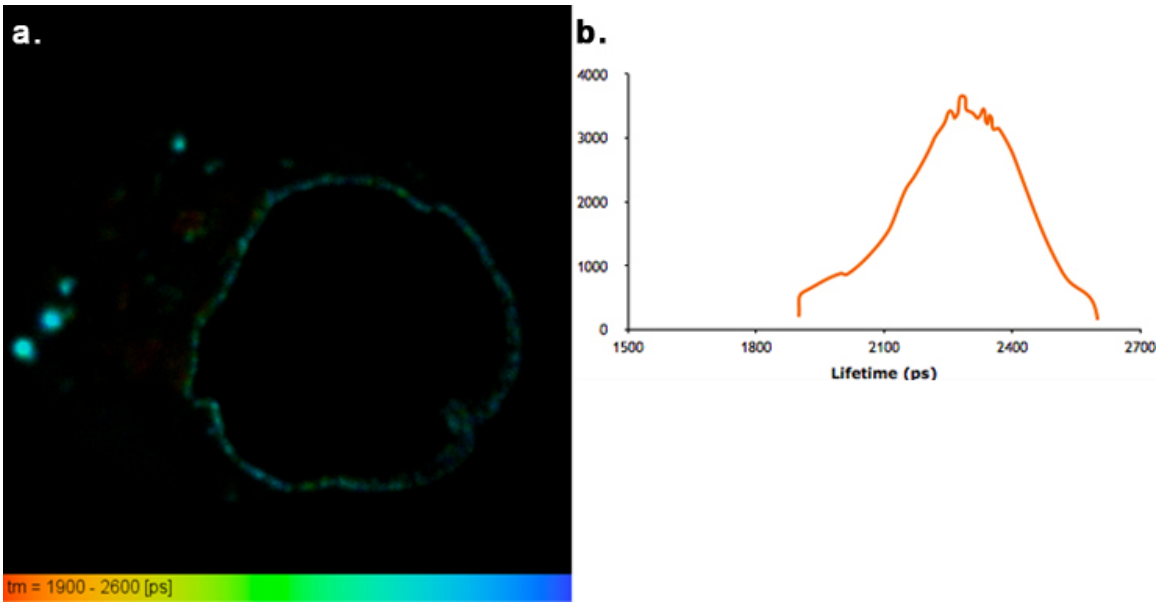

Figure 4.5: **FLIM of cells transiently expressing nup214/SNAP-tag.** a. A FLIM image of a crosssection of a HeLa cell showing the lifetime of BG-BODIPY targeted to nup214 in the NPC, as well as several cytoplasmic inclusions. b. A lifetime histogram of BG-BODIPY targeted to nup214 (peak value = 2287.2).

4.2.4 Mitoxantrone alters the microviscous environment of transiently expressed nup214

Given that it seemed unlikely we would be able to compare the lifetime measurements within the NPC to those of known hydrogels to determine the phase within the pore, we decided to attempt to disrupt the permeability barrier to understand its nature. We expected mitoxantrone to have a broad effect on phase separation within the cell, including a putative hydrogel within the NPC.

We subjected cells expressing the nup214/SNAP-tag construct to incubation with 10µM mitoxantrone, the same concentration used in the TDP-43 experiments. We then made FLIM measurements after 1.5 hours treatment. After performing decay curve analysis for each image, we selected a region of interest that corresponded to the NE for individual cells, and compared the lifetime peak with that of untreated cells. Surprisingly, there were two peaks in the histograms of these cells, both of which were significantly downshifted from the lifetime in control cells. These peaks roughly correspond to ~600ps and ~1600ps, both massive drops from the average for control cells (Figure 4.6), however, typically one of these peaks dominated for an individual cell.

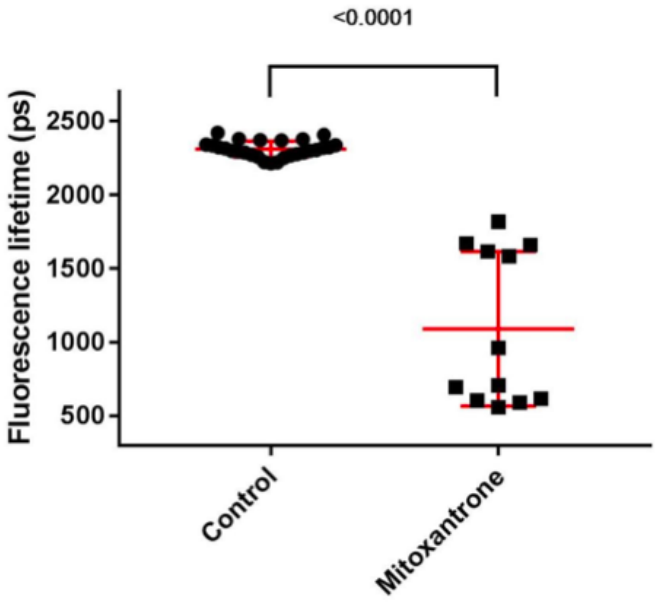

Figure 4.6: **Mitoxantrone reduces reported lifetime from within NPCs labelled with BG-BODIPY.** Regions of interest were drawn around the NEs of cells expressing nup214/SNAP-tag either treated with 10µM mitoxantrone or not, and the peak fluorescence was recorded. Mitoxantrone treatment resulted in a significant ($p<0.001$) decrease in the peak lifetime.

That mitoxantrone treatment results in two distinct peaks was puzzling. If this was an artefact of mitoxantrone's interaction with BG-BODIPY, we should have seen it in the TDP-43 experiments. We were left to contemplate the possibility that dissolving the gel-phase these proteins typically inhabit exposed them to two different microviscous environment. What these may look like is difficult to say without further experimentation. We can speculate, however, that this might reflect that in the absence of the weak binding interactions between the FG-motifs, disrupted by mitoxantrone, nup214 is free to experience the free cytosol or may continue to experience restriction by the other FG-nups but without binding.

As intriguing as these findings were, we were much more interested in making lifetime measurements in cells without transient overexpression, as we were concerned that overexpression would alter the number of FG-nups within the central channel, and thus the relative density of these nups, which would in turn affect the microviscous environment. CRISPR knock-in seemed like the best way to introduce the SNAP-tag enzyme while maintaining a physiological copy number of FG-nups within the channel. This would prove far more challenging than antici-

pated, as explained below.

4.2.5 Generation of cell lines

We employed the department's CRISPR service to assist us in the generation of three CRISPR knock-in cell lines, adding the SNAP-tag enzyme to three FG-nups – nup98, nup214, and nup153 – at the endogenous locus. This line was chosen because these cells are well suited to transfection, and have a karyotype that is much closer to diploid than HeLa cells. We aimed to insert the SNAP-tag enzyme at the C-terminus of nup153 after the XFXFG repeats, the C-terminus of nup214 after its FG repeats, and the N-terminus of nup98 just before the FG repeats so not to block its interaction with Nup96. The CRISPR service generated guide RNAs appropriate for targeting the cas9 enzyme to create double strand breaks at the desired locations. The service also provided us with the eSpCas9(1.1) enzyme, a mutated form of the enzyme designed to have fewer off-target effects (Slaymaker *et al.*, 2016) that had been cloned into the original pX459 plasmid and re-named it epX459(1.1).

These were transfected alongside template sequences containing the SNAP-tag enzyme sequence between 600bp homology arms in the pUC57 vector, generated by Genewiz. After transfection, we waited for the cells to recover, labelled them with BG-BODIPY, and sorted them using FACS. Very few cells were 'positive,' on the order of a couple dozen in several million. These cells were isolated into 96-well plate wells and allowed to grow into clonal colonies. For each of the nucleoporins we selected clonal colonies that had the brightest nuclear rim signal.

To confirm the localisation of the SNAP-enzyme to the appropriate location, we fixed and permeabilised cells from each of these lines and co-labelled them with mab414 and a polyclonal anti-SNAP-tag antibody (NEB) (Figure 4.7). This latter antibody is only recommended for use in Western Blotting, and frankly it's obvious why. Despite attempts at optimisation, using this antibody for immunofluorescence resulted in a considerable amount of background signal. However, despite this issue, there is an evident punctate nuclear rim signal and a high degree of co-localistion in all three of the cell lines (Figure 4.7), confirming the presence of SNAP-tag in the NPC.

Despite the above evidence that we had successfully incorporated the SNAP-tag enzyme into the NPC attached to various FG-nups, I was never able to confirm this

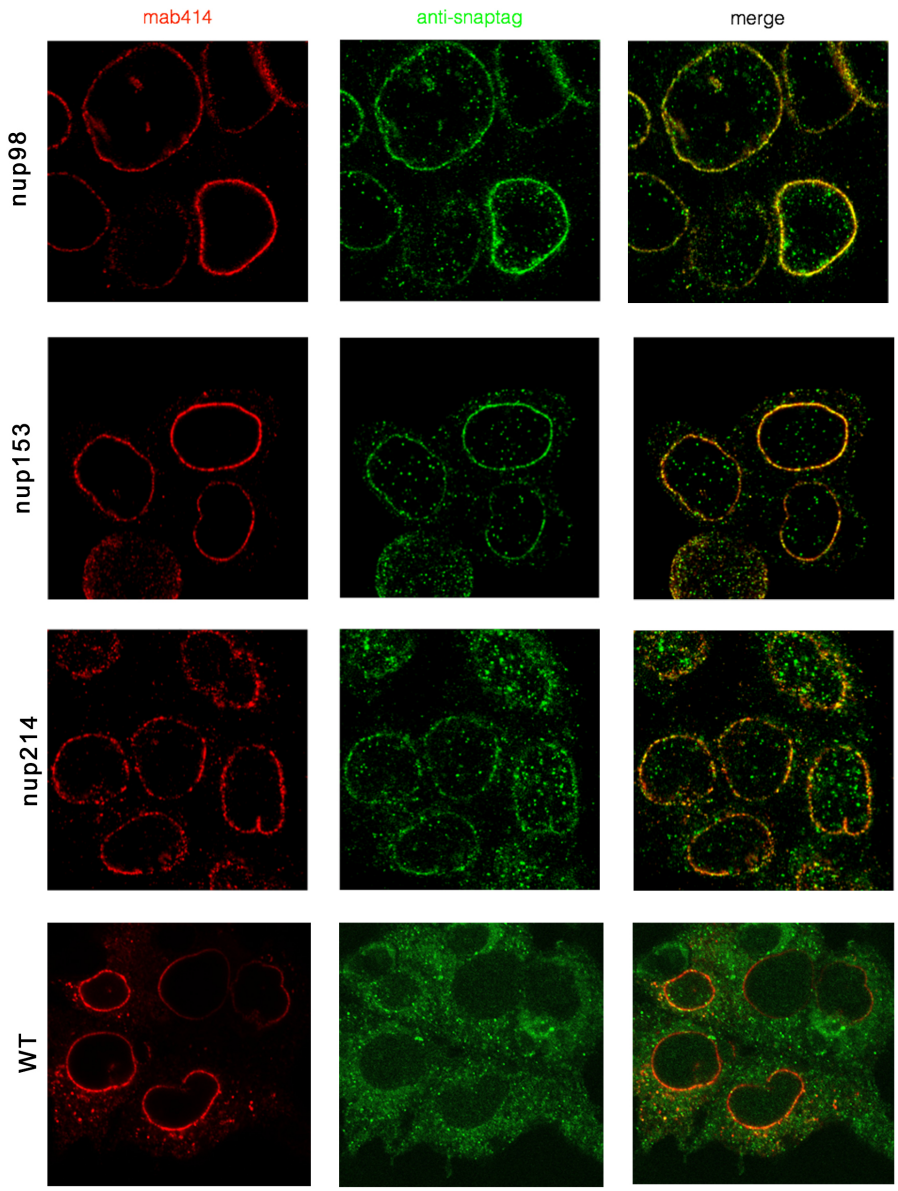

Figure 4.7: **Confirmation of the presence of SNAP-tag at the NPC in CRISPR'd cell lines through IF.** mab414 was labelled with donkey anti-mouse IgG Alexa Fluor 594, while anti-SNAP-tag was labelled with goat anit-rabbit IgG Alexa Fluor 488. There is clearly colocalisation with mab414 for all three CRISPR lines despite the high background, but there is very little colocalisation in wild type cells.

incorporation by sequencing. This was particularly concerning given the design of our CRISPR experiment; we only knocked in the SNAP-tag enzyme without any other tag or selection marker, and so our only means of selecting positive cells was the BG-BODIPY signal. Thus, all of the following results are presented with this major caveat in mind.

Because of this, we also attempted to generate nup/SNAP-tag lines using the CRISPR-Cas12a PCR-tagging system in an attempt to create lines with a puromycin selection marker (Fueller *et al.*, 2019). After following the protocol and transfecting HCT-116 cells with the Cas12a construct and templates for generating nup62, nup153, and nup214 knock-ins, we selected with 5µg/ml puromycin for two weeks. Despite generating a handful of resistant colonies for each line, when we labelled these cells with BG-BODIPY, none of them presented with a positive phenotype. Having spoken to colleagues about their experiences with puromycin selection, selection without insertion does not seem to be an uncommon occurrence. As my final year was rapidly coming to a close by this point, it was decided that we would go ahead and use the cell lines already generated.

4.2.6 FLIM measurements of tagged FG-Nups

Upon attempting to label the CRISPR knock-in cell lines with BG-BODIPY, we became aware of a significant hurdle in our efforts to make FLIM measurements of the tagged protein at endogenous levels. The fluorescence labelling was so weak in these cells that FLIM acquisition took many minutes to build up an adequate signal, even with the pinhole wide open. This meant we would be unable to investigate processes that occurred on short time scales, such as transport events. Further, because we needed to open the pinhole significantly during image acquisition, we would not be able to resolve individual NPCs to see if there were variations between the individual pores.

This is likely due to the low copy number of each of these nups in a given NPC. Some work has suggested that there are as few as 8 copies of nup153 in a given pore (Li *et al.*, 2019), meaning there would be around 8,000 copies distributed across the whole of the nuclear envelope. It is likely that only a fraction of these are being labelled in a given cell, so the signal from a single pixel could be extremely low. However, this, if anything, emphasises the risks in using an overexpression system.

Despite these setbacks, we were able to gather FLIM images of all three cell lines with a discernible (if rather blurry) nuclear rim. The three nucleoporins we chose to tag all localise to different regions within the NPC. Nup214 localises entirely to the cytoplasmic face of the NPC, just proximal to the filaments that extend into the cytoplasm (Kraemer *et al.*, 1994). Meanwhile, nup153 appears to be exclusively localised to the nuclear face of the NPC, and plays a role in anchoring elements of the nuclear basket (Krull *et al.*, 2004; Rahanala & Nandicoori, 2012). Nup98

localises to both faces of the NPC (Griffis *et al.*, 2003), possibly attaching to the subcomplexes that contain both nup214 and nup153 (Krull *et al.*, 214).

We figured, then, that we could potentially detect any differences in viscosity that might exist between opposite faces of the NPC. We collected FLIM images of all three cell lines labelled with BG-BODIPY and drew ROIs around the NE of individual cells, and recorded the mode lifetime for each cell. While there was considerable overlap between the lifetimes reported for cells in each line, a picture emerged in which nup214 tagged cells had a significantly higher lifetime than nup153 tagged cells ($p = 0.0002$) (Figure 4.8). Nup98 cells on average reported lifetimes somewhere in between, still significantly different to nup214 ($p = 0.008$) highlighting the fact that nup98 localises to both faces of the NPC.

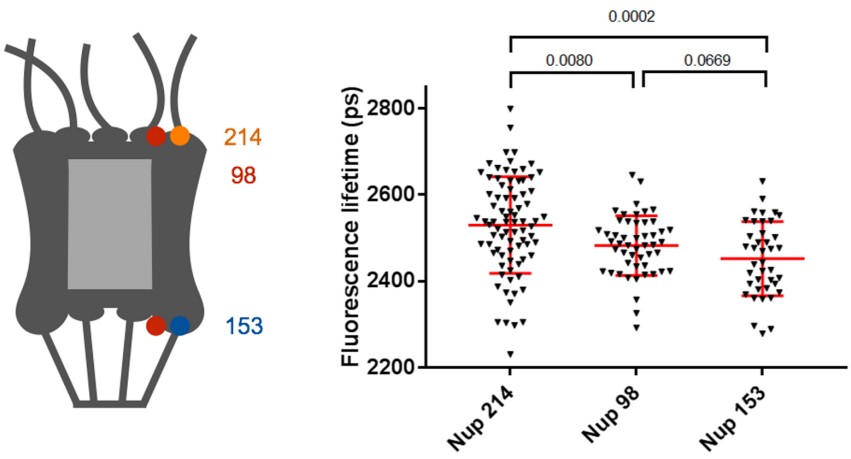

Figure 4.8: **HCT-116 cells expressing SNAP-tag at endogenous levels at different faces of the NPC have disparate average lifetimes.** ROIs were drawn around the NEs of cells expressing the SNAP-tag enzyme attached to either nup214, nup98, or nup153 and labelled with BG-BODIPY. The peak lifetime values of the histograms within these ROIs were then measured for individual cells of each line and plotted. We found there was a significant difference between nup214 and nup153 ($p = 0.0002$), and nup214 and nup98 ($p = 0.008$), but not nup98 and nup153. The schematic to the left shows the positions of the individual nups within the pore complex with the cytoplasm at the top and the nucleoplasm at the bottom.

4.2.7 Disrupting the NPC permeability barrier to investigate its phase

Having established that we could potentially disrupt the formation of a putative hydrogel within the NPC through treatment with mitoxantrone in cells overex-

pressing nup214/SNAP-tag, we next sought to repeat this in cells expressing an endogenous level of nucleoporin proteins. As a negative control, we used lipoamide in the same concentrations, as it has been shown to have a much narrower effect, melting FUS-positive stress granules, but not other cytoplasmic condensates, so it stood to reason that it would not affect NPC barrier function.

To test this, we treated the NLS/mCherry fusion expressing HeLa cell lines with 10µM of mitoxantrone to monitor its effects on the localisation of mCherry to the nucleus. We found that mitoxantrone did in fact lead to leakage of the NLS/mCherry fusion proteins from the nucleus (Figure 4.9a). Leakage occurred over a time course of two hours, by which point the fraction of nuclear to cytoplasmic mCherry had changed significantly ($p<0.001$) (Figure 4.9b) while a DMSO control showed no such leakage (Figure 4.9c). This supports the idea that mitoxantrone treatment is altering the properties of the central channel of the NPC.

We next treated the three cell lines we had generated with 10µM mitoxantrone or 10µM lipoamide and measured the fluorescence lifetime of BG-BODIPY in each line for each condition. The lipoamide treatment resulted in a modest reduction in lifetime in nup214, or had no effect at all (Figure 4.10). The cells treated with lipoamide all reported a fairly uniform lifetime distribution. Cells treated with mitoxantrone from each line all reported greatly reduced lifetimes with bimodal distributions, or, in the case of nup153, a trimodal distribution. The relative weight of these distributions varies in each cell line, and we remain in the dark as to the cause of their appearance. While there was a slight reduction in the lifetime across the board from when we first made these measurements in Figure 4.10, the relative difference between the two faces of the NPC was maintained.

4.2.8 Ac5SGlcNAc treatment did not disrupt the permeability barrier

Loss of *O*-GlcNAcylation of several FG-nups through inhibition *O*-GlcNAc transferase (OGT) with the sugar Ac5SGlcNAc has been shown to cause the degradation of these nups through ubiquitination, resulting in the break down of the selective permeability barrier (Zhu *et al.*, 2016). We reasoned that the removal of these nups would have a significant impact on the crosslinking of the putative hydrogel within the NPC central channel, and potentially alter the lifetime of BG-BODIPY targeted there. We first sought to recreate those previous demonstrations of Ac5SGlcNAc's

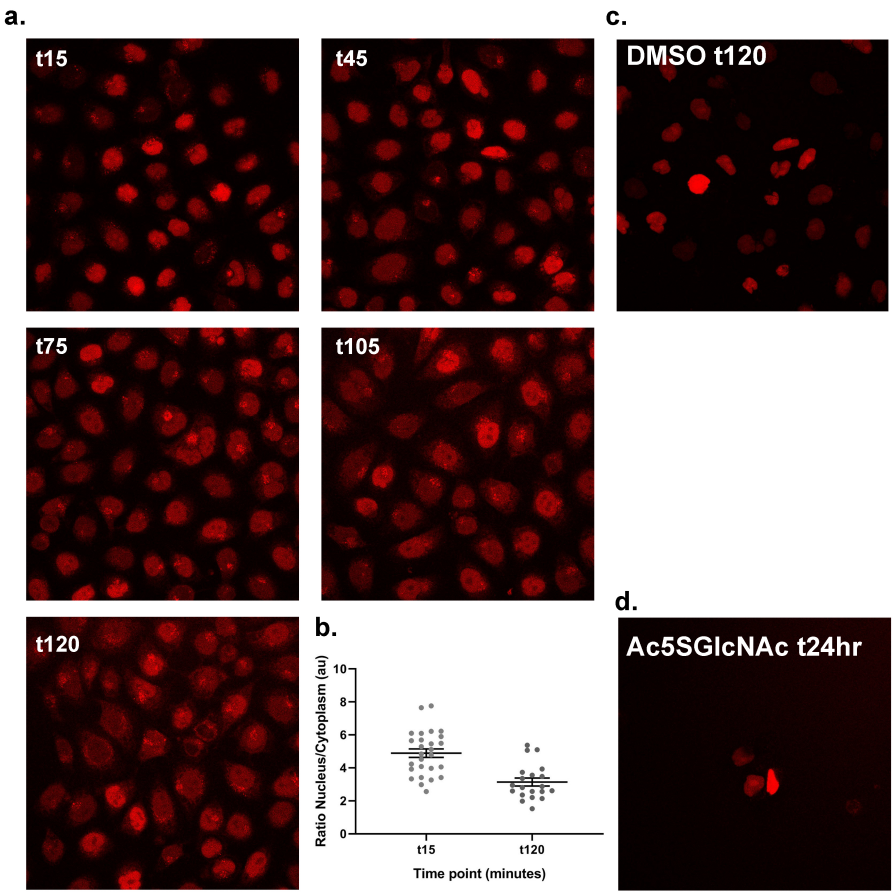

Figure 4.9: **Mitoxantrone disrupts the selective permeability function of NPCs.** a. Timecourse of mCherry-NLS following treatment with 10µM mitoxantrone. The signal becomes increasingly diffuse and cytoplasmic as time passes. b. Ratio of nuclear to cytoplasmic mCherry signal at the beginning and ending time points in a. c. DMSO treatment of cells for the equivalent time does not result in leakage of mCherry from the nucleus. d. 24 hour treatment with Ac5SGlcNAc did not result in the breakdown of the selective permeability barrier as has been shown previously (see Section 4.2.8).

deleterious impact on the permeability barrier by treating the mCherry/SNAP-tag/NLS cell line with Ac5SGlcNAc overnight. However, we did not find any leakage of mCherry from the nucleus (Figure 4.9d). While the Ac5SGlcNAc was properly stored after we received it, it was some time afterwards that we actually performed the experiments, and it is possible the stock had degraded.

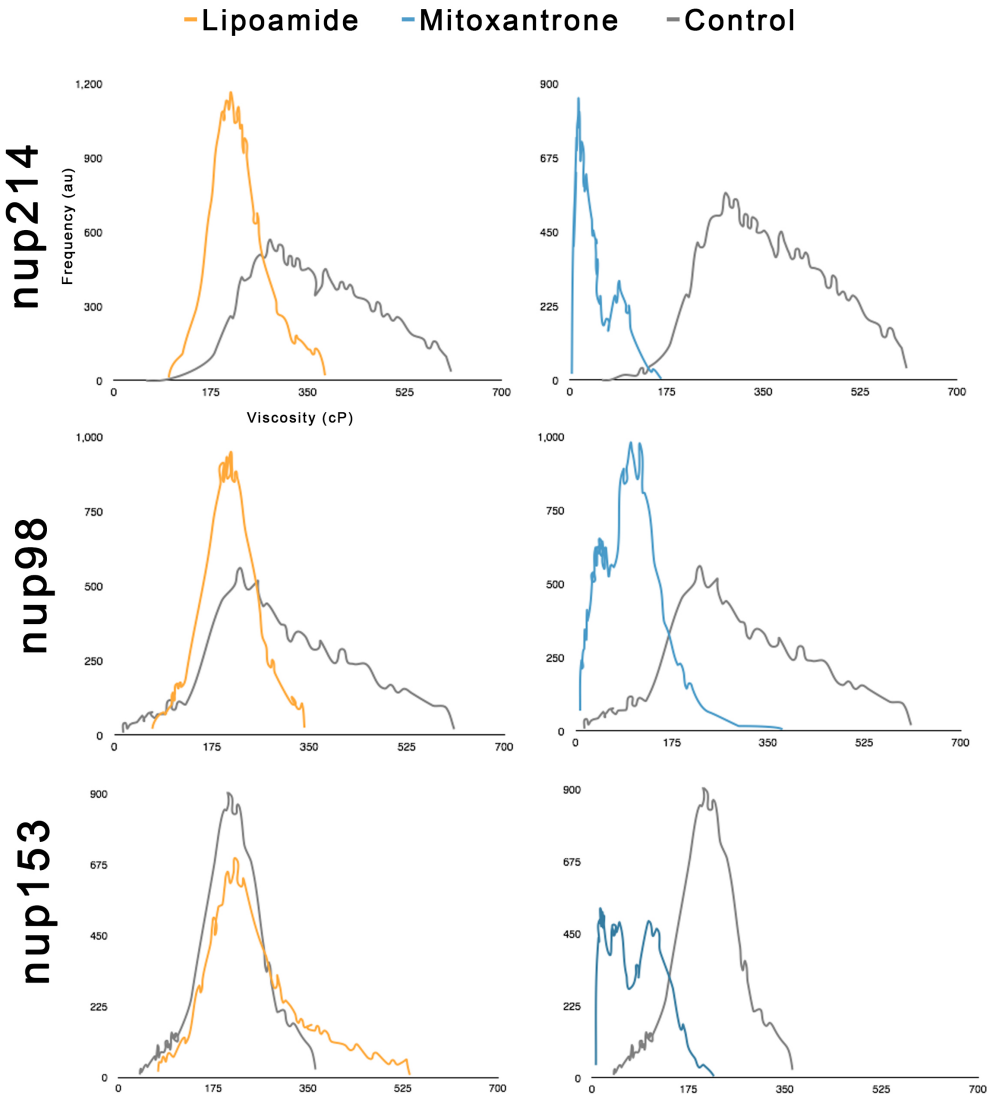

Figure 4.10: **Mitoxantrone reduces the viscosity within the NPC at nups 214, 98, and 153, while lipoamide does not.** The left hand column shows the comparative viscosity histograms for untreated cells and cells (n=~20) treated with 10µM lipoamide for all three cell lines. The x-axis represents the viscosity in cP, while the y-axis is frequency in arbitrary units. The right hand column depicts the same control viscosities for each of the cell lines compared with the reported viscosity in cells treated with 10µM mitoxantrone.

4.2.9 A note on the picture from the perspective of nuclear transport factors

The results presented here so far offer a picture of the viscosity associated with NUPs, the molecular machinery that controls selective transport via the NPC.

An alternative approach would be to attach a BODIPY viscosity probe to a cargo molecule or an NTF in order to measure the local microviscosity it experiences during its passage through the NPC. This approach could confirm that these client transport complexes are experiencing the same environment as the FG-nups they have to pass through.

In order to achieve this, I cloned importin subunit α5 into the pSNAPf vector and expressed it in HCT116 cells. The expression was not impressive, and of the handful of cells that appeared to be labelled with BG-BODIPY, only a couple looked to have a signal phenotype that looked comparable to what one would expect with expression of this protein.

FLIM analysis of these two cells revealed somewhat disparate lifetime values, but both histograms were well within the range of values we had previously observed for BG-BODIPY targeted to nucleoporins. This is encouraging, as at least these preliminary results indicate cargo passing through the NE experiences the same microviscous environment as the proteins within the pores they pass through. Obviously these results are less than complete and this experiment will need to be taken with a grain of salt until we are able to optimise the transfection and have the chance to replicate the study.

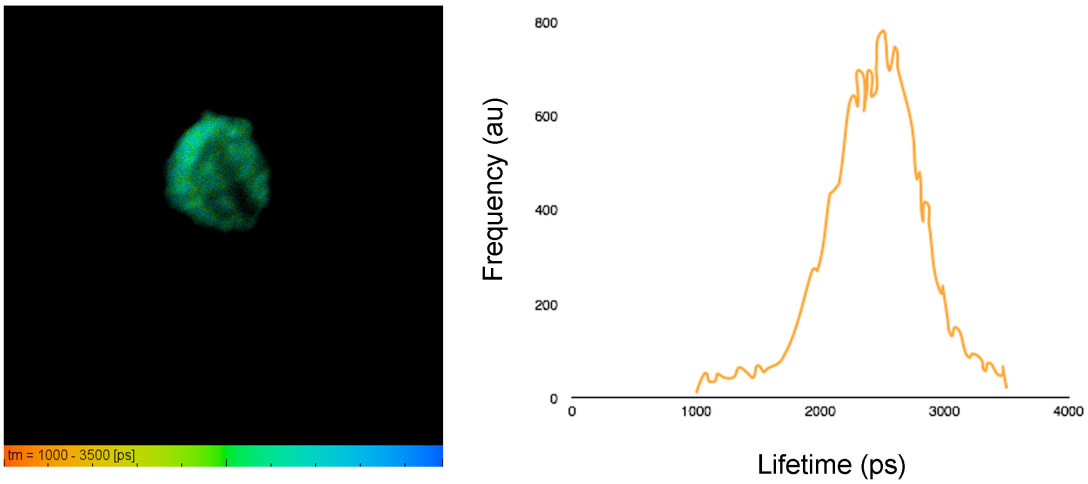

Figure 4.11: **BG-BODIPY targeted to transiently expressed Importin5α reports similar lifetimes to those of the NPC.** A FLIM image and its lifetime histogram (peak at ~2500ps) of BG-BODIPY targeted to Importin5α.

4.3 Discussion

In this chapter we have shown that it is possible to use BG-BODIPY to analyse viscosity in structures smaller in scope than whole organelles. BG-BODIPY can be targeted to FG-nucleoporin proteins to make viscosity measurements at a series of positions along the NPC. We can use BG-BODIPY to monitor changes in the internal viscosity of the central channel upon treatment with drugs to disrupt the interactions of the FG-nups.

The biggest problem we faced in this chapter was the low copy number of the tagged proteins of interest, which made collecting enough photons to build up FLIM images a challenge. This meant we were unable to build up the detailed FLIM images of individual NPCs we had originally hoped to create in order to measure responses of the individual pores. The images we were able to take, while sufficient for making measurements of whole NEs, were far too blurred to make inferences about individual pores. We could likely have increased the resolution of our FLIM images, our system was set to collect images with 512 x 512 pixels, but the Becker & Hickl system can collect images with pixel dimensions of 2048 x 2048 without compromising temporal resolution. However, this would not have solved the issue of low signal.

Despite this, we were still able to collect a good deal of data that brings us closer to understanding the phase within the central channel of NPCs under physiological conditions in living cells. There was already good evidence that mitoxantrone had a negative impact on nuclear transport: Wheeler *et al.* (2019) noted that lipoamide treatment not only reduced stress granule numbers, but also restored FUS to the nucleus, while mitoxantrone had the inverse effect on nuclear/cytoplasmic distribution of FUS. They also demonstrated that mitoxantrone has a much broader effect, impacting a range of other condensates, including RNA processing bodies, Cajal bodies, and nucleolus proteins. Until now, however, there was no evidence that mitoxantrone exerts its effect at directly at the NPC. We have shown corresponding changes to the microviscous environment within the NPC at multiple positions within the channel upon mitoxantrone treatment, while lipoamide treatment had little to no effect.

The modest reduction in lifetime NPCs appear to have experienced upon lipoamide treatment suggests that there is a degree of flexibility to the central channel's properties. Perhaps lipoamide is able to perturb the system slightly without disrupting

the selective permeability function. The uniformity of the lifetime distributions between the different cell lines is certainly suggestive of lipoamide having some effect.

That there is a connection between nuclear transport and LLPS processes elsewhere in the cell is beginning to gain purchase elsewhere. While here we have shown a compound that dissolves SGs also modulates NPC behaviour, Guo *et al.* (2019) have recently shown that nuclear import receptors are capable of dissolving both physiological and pathological aggregates, including those produced by the RBPs FUS and TDP43. They posit that these NTFs play a role in shaping and regulating cytoplasmic membraneless organelles, and may have a role in preventing dangerous aggregation of RBPs with prion-like domains. This, combined with our research presented here, certainly lends credence to the notion that the central channel of the NPC represents a distinct phase from the nucleoplasm and cytoplasm, and that the FG-nups do not function as merely an entropic barrier.

Chapter 5

Investigating invertebrate cryptobiosis with BG-BODIPY

5.1 Introduction

The 100th episode of The Simpsons (Season 5, Episode 19, *Sweet Seymour Skinner's Baadasssss Song*) begins with Bart Simpson deciding what to bring to show and tell at school in lieu of home videos. His mother, Marge, suggests he take a potato she's holding as, 'it's pretty big.' Bart comments that she is always trying to give him potatoes and asks, 'What is it with you?' to which she responds, characteristically, 'I just think they're neat.' The throwaway joke is meant to be a demonstration of Marge's wilful naivete – both a coping mechanism for, and a symptom of the emptiness of her life as a housewife – as a foil for Lisa's liberal cynicism. (If you, the viewer, identify with any character from the golden age of The Simpsons other than Lisa, it is likely that the show was written *about* you rather than *for* you.) However, the scene has always stuck with me as a heartwarming example of finding wonder in the quotidian that we should all aspire to.

The longer I spend in science, the more progress seminars and departmental symposiums I sit through, the more I find myself returning to Marge and her potato. The impact of capitalism and the advent of biomedical research as an industry on academic science cannot be understated. Much has been written on the shift to the university as a business model and the tremendous pressure to 'publish or perish'. The most sinister change, in my opinion, has been in how scientists justify their research. Academics now must pitch their research in terms of use value; it often feels as though research that cannot be easily commodified as a medical treatment

or a novel research tool is seen as a fool's errand. And so I cannot help but feel as I watch another glassy-eyed student rattle off the potential therapeutics that could be developed from their research into an enzyme they have little interest in that we are missing something as a field. Imagine a world in which students and PIs chose research subjects not because they were trendy and likely to secure grant funding, but because, like Marge and her potatoes, they believed they were neat. How much more inspiring would conferences be if every presentation was on research that needed no further justification than, 'We wanted to know.' But perhaps my own wilful naivete is showing.

When I presented some of the findings in the following chapter at a progress seminar in our department, an iminent figure in our department asked, 'Not to be confrontational, but what's the point?' Ignoring what they say about everything that comes before the 'but,' I was a bit surprised by the question. Tardigrades have become the pinnacle of 'neat' science, and their prominence in popular science shows that they have captured the wider public's imagination. Since I began telling my friends and family that I was working on tardigrades, not a month has gone by where someone hasn't sent me a news article on them or introduced me at a party as someone who 'works on tardigrades.' And yet, upon showcasing what I consider some of my most interesting and novel findings to the department, I was met with mostly baffled stares, as though I had presented an actual potato.

The question filled me with indignance: We had discovered something hitherto unknown, what further justification was needed? Of course, there is a 'point,' in the sense he meant; the use value of tardigrades and their remarkable survival abilities is becoming increasingly apparent. It has been reported that the US military's Defence Advanced Research Projects Agency (DARPA) is currently researching tardigrades in hopes of developing a cryptobiotic technology to place wounded soldiers in stasis until they can receive treatment. That I should need to invoke this though, threatened to cheapen the research in my view.

Tardigrades, colloquially known as 'water-bears,' are a phylum of aquatic and semi-aquatic invertebrates belonging to the superphylum Panarthropoda, which comprises, Arthropoda, Onychophora, and Tardigrada. First identified in 1773 by Johann Goeze (Goeze, 1773), Tardigrades have been largely neglected despite their ubiquity and the over 1000 species that have been identified thus far (Degma *et al.*, 2010). They are easily identifiable by their unique morphology; tardigrades possess a head, three body segments with a pair of legs each, and a final caudal

segment with one more pair of legs. Analysis of tardigrade *Hox* genes has revealed that this simple, compact body plan is the result of the loss of several *Hox* genes, resulting in the loss of a region homologous to nearly the entire thorax and abdomen of insects (Smith *et al.*, 2016).

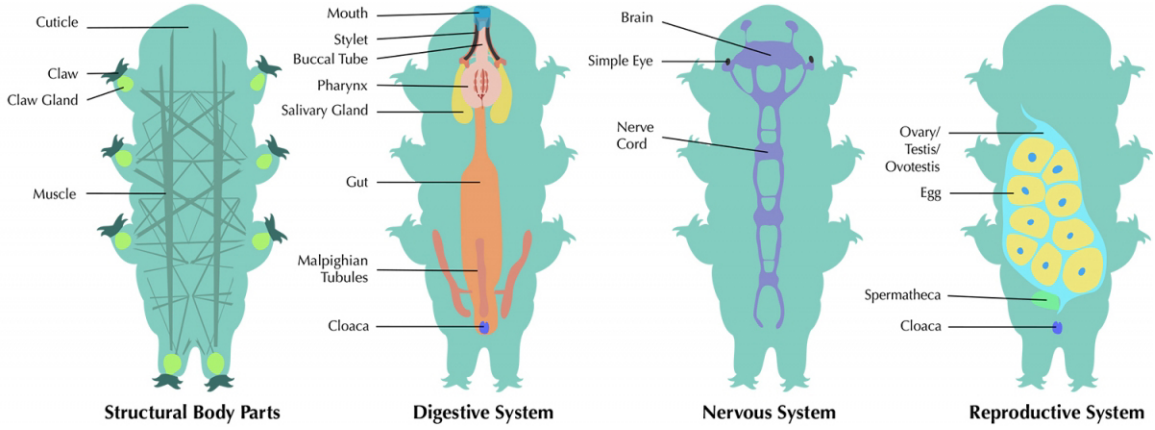

Figure 5.1: Tardigrade anatomy. Taken from Bespalova, 2019.

Their recent rise in popularity with the general public seems to be a result of the combination of the 'cuteness' of their truncated morphology and a fascination with their (fairly overblown) ability to survive a wide range of hostile conditions. It is now possible to buy everything from tardigrade plush toys, to towels and shirts depicting tardigrades flying through space, to tardigrade slippers on Amazon.

Tardigrades are able to enter dormancy states of both diapause and cryptobiosis, the former being a process under endogenous control that sometimes correlates with cyclic environmental changes, whilst the latter is a quiessence response to environmental factors that results in a reduction of metabolic processes to a standstill which can be reversed when environmental conditions become favourable once more (Guidetti *et al.*, 2011). Tardigrades have been shown to enter a cryptobiotic state in response to desiccation (anhydrobiosis), freezing (cryobiosis), and possibly lack of oxygen (anoxybiosis) (Guidetti *et al.*, 2011; Guidetti, Altiero, *et al.*, 2011). There is also some evidence that tardigrades become quiescent in response to osmotic stress (osmobiosis) (Heidemann *et al.*, 2016), though the existence of this response has been doubted and is little studied (Guidetti *et al.*, 2011).

Successful anhydrobiosis in tardigrades is marked by a morphological change that results in the formation of a 'tun,' whereby they retract their legs and curl up to reduce the surface area of the more permeable regions of the cuticle that are exposed

to the air in order to reduce the rate of desiccation (Wright, 1989a, Wright 1989b). Once in the tun state, tardigrades can survive for years (Guidetti & Jönsson, 2002; Rebecchi *et al.*, 2006), and can tolerate considerable abiotic stressors, such as extreme temperatures, high pressure, and even the vacuum of space (Ribecchi *et al.*, 2007; Hengherr *et al.*, 2009a; Hengherr *et al.*, 2009b; Horikawa *et al.*, 2009; Jönsson *et al.*, 2008). Upon resuspension in water, tardigrades experience no shortening of their lifespan for having been in the cryptobiotic state (Hengherr *et al.*, 2008a).

It is only recently that the molecular underpinnings of this remarkable survival ability have begun to be investigated. Multiple tardigrade species have an orthologous protein called Dsup that is able to protect chromatin from damage from hydroxyl radicals generated by ionising radiation or hydrogen peroxide treatment (Hashimoto *et al.*, 2016; Hashimoto and Kunieda, 2017; Chavez *et al.*, 2019). Dsup confers protection by binding nucleosomes and blocking hydroxyl radicals from accessing the hydrogen atoms in the minor groove of DNA. Dsup expressed in human cells is able to transfer this protective ability to a smaller degree.

Tardigrade desiccation survival is dependent on the drying occurring at a sufficiently slow pace (Wright, 1989), reflecting their need for *de novo* transcription and translation to survive this process (Kondo *et al.*, 2015). *H. exemplaris* (formerly known as *H. dujardini*) expresses three families of intrinsically disordered proteins (IDPs) – Cytoplasmic Abundant Heat Soluble proteins (CAHS), Secretory Abundant Heat Soluble proteins (SAHS), and Mitochondria Abundant Heat Soluble Proteins (MAHS) – that are specific to tardigrades and are either constitutively expressed at high levels or enriched upon desiccation (Tanaka *et al.*, 2015; Yamaguchi *et al.*, 2012; Boothby *et al.*, 2017). Other desiccation resistant organisms, such as certain nematodes and arthropods, the disaccharide trehalose is produced in large amounts and vitrifies the organism, which is thought to confer protection by preserving the homogeneity and compactness of lipid acyl chains, and by reducing the aggregation of prion-like proteins upon desiccation (Erkut *et al.* 2011; Tapia & Koshland, 2014). Tardigrades vitrify upon desiccation as well, but this appears to be mediated by these IDPs rather than a disaccharide, in an interesting case of convergent evolution.

5.2 Results

5.2.1 Uptake and distribution of BG-BODIPY in whole eukaryotic organisms

Our first question was whether BG-BODIPY would penetrate the various organelles of tardigrades. We imagined that the only way BG-BODIPY would bypass the chitinous cuticle of tardigrades was through their digestive tract, however it was unclear whether this would penetrate to their other organs.

To test this, we incubated *H. exemplaris* with 2.5µM BG-BODIPY in water overnight in a 96-well plate and imaged them the following day. To immobilise the tardigrades for imaging, we tried several strategies, including trapping them in 2% agarose, however, we discovered that the most effective means was the addition of 1% chloroform, which rendered the tardigrades immobile for 30-60 minutes. After this period, the tardigrades appeared to recover.

We were pleasantly surprised to discover that BG-BODIPY appeared to permeate the entirety of the organism (Figure 5.2). The whole of the digestive tract was labelled, from the mouth with its piercing stylets, to the sucking pharynx, to the midgut. The ventral nerve ganglia and muscle fibres were also clearly visible. We were also able to see the storage cells that float freely throughout the body of the tardigrades. The gonads were also labeled, along with the brain, and the salivary gland and foot glands.

I am aware of the irony that the preceding chapters have been devoted to demonstrating the specificity of BG-BODIPY's interaction with the SNAP-tag enzyme while in this chapter we use it to stain whole organisms indiscriminately. However, I feel this demonstrates the versatility of BG-BODIPY as a viscometer and in no way undermines its uses as a SNAP-tag label outlined in the above.

5.2.2 Viscosity measurements of tardigrades in physiological conditions

Having demonstrated that BG-BODIPY permeates the entirety of the organism, we were able to begin making viscosity measurements. Tardigrades were stained and immobilised in the same manner as described above, but this time were imaged using FLIM. FLIM imaging proved somewhat challenging at 60x magnification, given the size of the organisms. Some tardigrades can grow to 0.5mm in size,

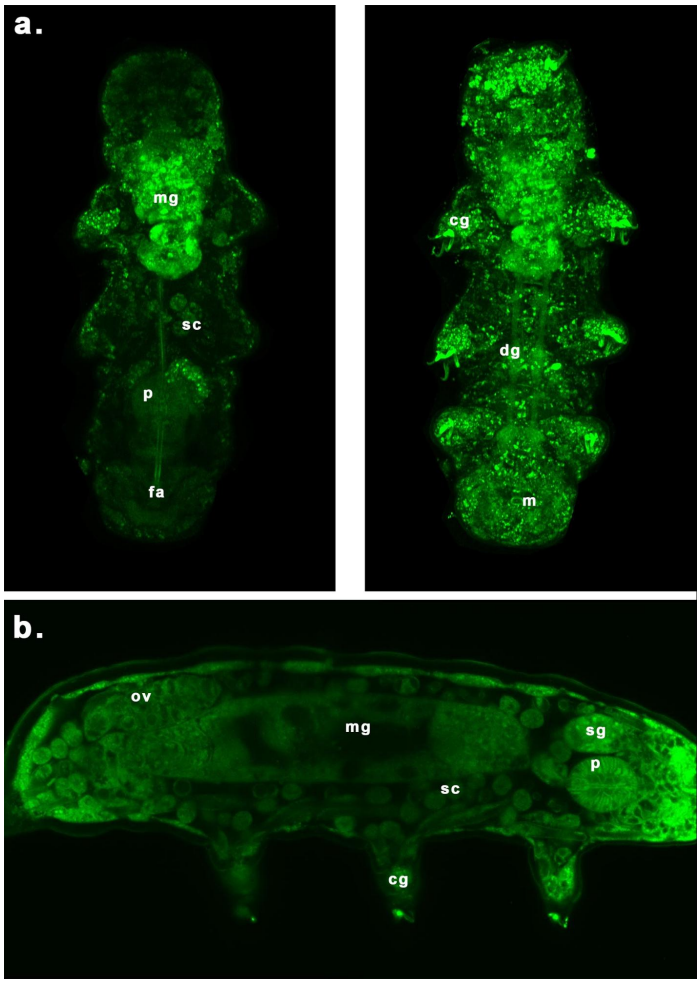

Figure 5.2: **BG-BODIPY staining of tardigrades.** Airyscan images of a. two frontal planes of a tardigrade showcasing staining of the midgut (mg), storage cells (sc), pharynx (p), feeding apparatus (fa), mouth (m), dorsal nerve ganglion (dg), claw glands (cg) and b. a sagittal plane section showing the ovary (ov) and salivary gland (sg).

however there were plenty of individuals small enough to image in a single frame. Growth in tardigrades occurs through hypertrophy as opposed to cell division, so individual organisms have the same number of cells irrespective of size.

A range of viscosities were reported by BG-BODIPY, spanning from 0 cP to ~600 cP, with a peak at around 180 cP (Figure 5.3). For comparison, maple syrup has a bulk viscosity of ~150-200 cP. The lowest viscosities were reported in the midgut, but this is likely due to the presence of algae in the midgut that produces its own short lifetime. The next lowest viscosities were reported from the claws and the 'teeth' or apophyses of the pharynx and the piercing stylets. These structures are

rigid and chitinous, making it likely that BG-BODIPY has simply become stuck to their surfaces and is reporting the low viscosity of the extra-organismal environment in the case of the claws, and the lumenal space in the case of the pharyngeal apophyses. The floating storage cells had a lifetime of around 1500ps, which according to our calibration represents a viscosity of around 91cP, much lower than we previously observed in mammalian cells.

The rest of the cells and tissues, including the nervous tissues, muscle fibres, and gonads had fairly homogenous lifetimes, with peaks that ranged from around 160-180 cP depending on the individual.

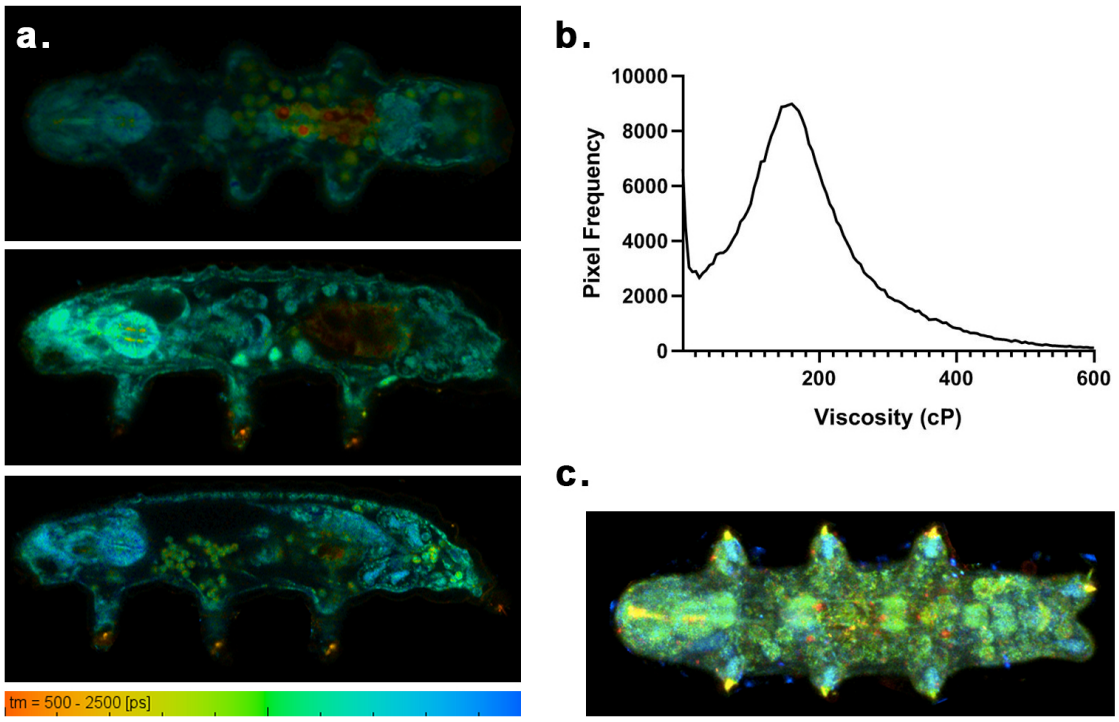

Figure 5.3: **FLIM measurements of whole live tardigrades.** a. A frontal plane and two midsagittal plane FLIM images of three individual tardigrades with most of the major structures on view. b. Viscosity histogram of a whole tardigrade, with a peak at ~180cP. c. A 3D projection of FLIM Z-stacks collected of a frontal plane of a tardigrade. All images are oriented such that the caudal end of the organism is to the left of the image.

5.2.3 Internal viscosity of tuns formed in response to desiccation

In order to survive desiccation, tardigrades require a period of 'preconditioning' in order to synthesise levels of TDPs required for vitrification (Boothby *et al.*, 2017).

We dried *H. exemplaris* that had been stained with BG-BODIPY both in low humidity (fast drying condition) for around 30 minutes and high humidity (>90% humidity) (slow drying condition) overnight to determine whether the molecular underpinnings of desiccation survival resulted in a change in microviscosity within the organism.

Both drying conditions resulted in the formation of the tun phenotype. The lifetime of the BG-BODIPY probe within the tuns in each condition was wildly different, however. In the fast drying condition, in which the tardigrades were desiccated too quickly for the production of the TDPs that mediate their survival, a wide range of higher viscosities were reported. The spread seems to be formed by two peaks, one slightly higher than the peak of hydrated tardigrades at ~180cP and another much higher at ~260cP. The slow drying condition had much stranger behaviour. These tuns, which should have properly vitrified, were brightly fluorescent, which typically indicates a higher lifetime, as fluorescence lifetime and intensity are positively correlated. However, the FLIM measurements we made revealed a narrow peak of extremely short lifetimes of around 500-600ps, which correspond to negligible viscosity values close to 0cP.

This was precisely the opposite of what we were expecting, given our knowledge that tardigrades that successfully enter the cryptobiotic state are supposed to vitrify. We expected to see an increase in lifetime with the transition to the glass phase. This major discrepancy, along with the apparent decoupling of fluorescence yield from lifetime, led us to conclude that the vitrification process had somehow caused BG-BODIPY to begin misreporting its microviscous environment. We envisioned several possible causes for this aberrant behaviour. In order to determine whether the behaviour was due to the phase transition to glass causing BG-BODIPY to 'drop out' of its useful reporting range or due to the desiccation of the molecule, we made a trehalose solution containing 5μM BG-BODIPY, and heated it to the glass transition point to make sugar glass. We then measured the fluorescence lifetime of the BG-BODIPY in the sugar glass, which was about ~3.5ns, which we estimate to be the upper limit of BG-BODIPY's useful reporting range. Thus, neither the boiling, nor the transition to the glass state seems to cause the aberrant lifetime. Future investigations will include examination of the possibility that the lifetime has become so long that it is not correctly reported when the laser pulses are separated by only 12.5 ns.

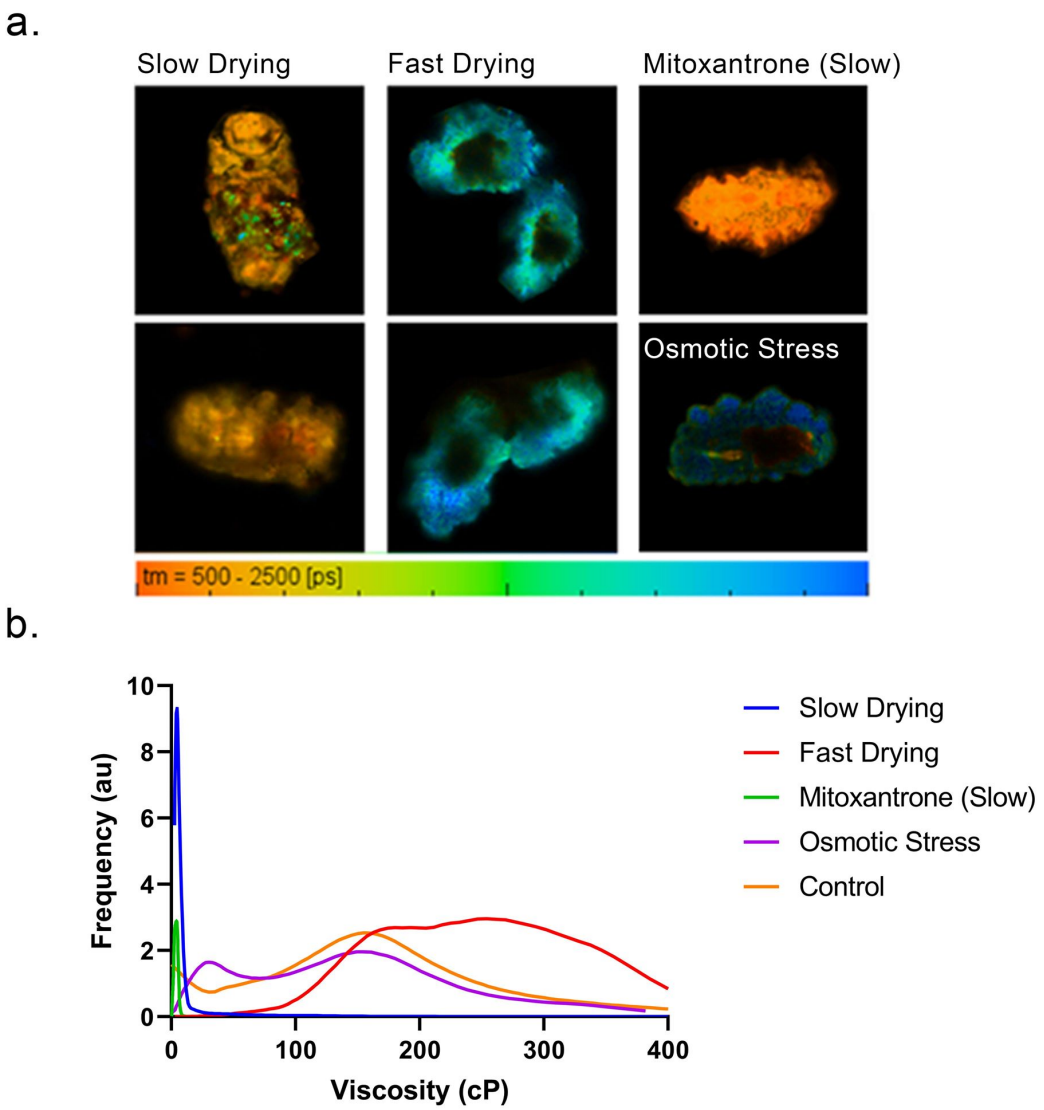

Figure 5.4: **Comparative internal states of tardigrade tuns formed under different stress conditions.** a. FLIM images of tardigrade tuns formed in high humidity (slow drying) and low humidity (fast drying) conditions, in high humidty while treated with mitoxantrone, and during acute osmotic stress (see Section 5.2.5). b. A comparison of the viscosity (cP) histograms for tuns in each condition.

We then treated tardigrades with 10µM mitoxantrone to see if it would affect the ability of these tardigrade specific disordered proteins to undergo the glass phase transition. Slow dried tuns formed in the presence of mitoxantrone showed the exact same aberrant lifetime as those formed without mitoxantrone (Figure 5.4).

5.2.4 *H. exemplaris* appears to tolerate osmotic stress

The ability of tardigrades to undergo cryobiosis in response to osmotic stress (osmobiosis) has been disputed, but recently *Ramazzottius oberhaeuseri* was shown to be able to survive acute exposure of up to 600 mOsm kg^{-1} NaCl (Heidemann *et al.*, 2017). We discovered, quite by accident, that *H. exemplaris* appears to have some ability to survive acute osmotic stress. While trying to isolate tardigrades in grids using the IsoCell system described in Chapter 3, we noticed that all of the tardigrades formed tuns when they came into contact with the DMEM that is used to make the chambers.

In order to see whether tuns could recover from osmotic stress, we isolated individual tardigrades and introduced them to PBS/distilled water mixtures of 90% or 30% PBS (270 and 90 mOsm kg^{-1}). By 30min, the all of the tardigrades in 90% had formed tuns, and by 3 hours all tardigrades had formed tuns. When tuns were placed in spring water once again, they all appeared to recover (Figure 5.5).

5.2.5 Tuns formed in response to desiccation and osmotic stress have differing internal viscosities

Having seen that *H. exemplaris* appears to have some ability to withstand acute osmotic stress, we wanted to see how the internal state of these tuns compared to those formed through desiccation. Given that production of TDPs takes time, we did not expect to see the same viscosity changes as in the slow drying conditions.

We stained tardigrades once more with 2.5µM BG-BODIPY overnight and then subjected them to acute osmotic stress by introducing them to 90% PBS (Figure 5.4a). FLIM analysis revealed an interesting picture: the tuns formed through osmotic stress had almost an identical lifetime histogram to that of tardigrades under normal conditions with a small second peak at around 400ps This second smaller peak is likely due to the fact that in the tun, the algae in the gut lumen represents a larger proportion of the total organismal volume, and therefore its lifetime is a more significant contribution to the lifetime histogram.

The fact that *H. examplaris* appears to survive both acute osmotic stress and desiccation, yet their internal viscosity appears to be completely different indicates that there are two distinct processes that mediate survival in response to each of the stressors. This has some precedents. Boothby *et al.* (2017) found that the transcriptomes of tardigrades undergoing cryptobiosis in response to desiccation

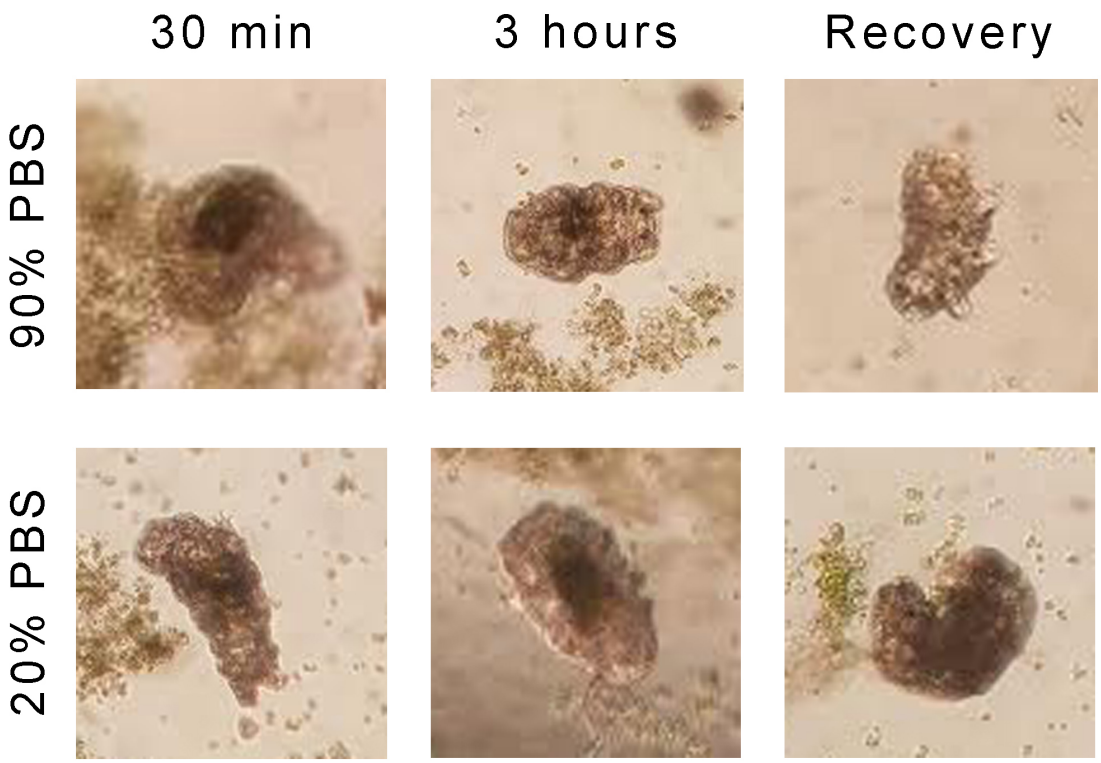

Figure 5.5: ***H. exemplaris* forms tuns in response to acute osmotic stress.** Tardigrades form tuns in response to acute osmotic stress from 90% PBS by 30 minutes and 3 hours in 20% PBS. In both conditions, when tuns were reintroduced to water, the organisms appeared to recover and regain motility. Images are examples, but all tuns ($n = 6$, $n = 4$) behaved uniformly.

or freezing and found that gene expression diverged under these conditions, indicating that instead of cross-tolerance, tardigrades have at least some differentiated stress responses. We were not able to repeat our experimental technique on tardigrades that had been frozen, as BG-BODIPY's response is sensitive to extreme temperature changes, and therefore would not be comparable. However, the results from our osmotic stress experiments demonstrate that tardigrades likely possess a response for acute osmotic stress that is distinct from its desiccation response.

5.2.6 Measuring microviscosity in bdelloid rotifers

Like tardigrades, bdelloid rotifers are a pioneering species, ubiquitously present in aquatic and semi-terrestrial environments. Their pioneering abilities are conferred by two traits that set them apart from other rotifers: their complete reliance

on apomictic thelytoky for reproduction and their ability to withstand harsh, fast changes in their environment through anhydrobiosis (Ricci, 1987). In fact, the ability to survive desiccation and maximise their geographic spread may be a requirement for survival with obligatory parthenogenetic reproduction; without sexual reproduction, dispersal is the only means by which bdelloids can escape parasitic invasion and The Red Queen (Judson, 1996). While most genetic clusters are limited to the continental scale or smaller geographies, bdelloids do show broad genetic dispersal consistent with other microscopic organisms, and some are truly cosmopolitan (Fontaneto *et al.*, 2008).

Also like Tardigrades, desiccation tolerance in bdelloids was initially believed to be mediated by a disaccharide such as trehalose or sucrose, however this no longer appears to be the case. Two species of bdelloids, *Philodina roseola* and *Adineta vaga*, were shown to be able to survive desiccation without the presence of significant amounts of trehalose or other disaccharides in tuns, and without the presence of a trehalose synthase gene (Lapinski & Tunnacliffe, 2003). *P. roseola* does, however, upregulate hydrophilic late embryogenesis abundant (LEA) proteins upon desiccation (Tunnacliffe *et al.*, 2005), indicating that bdelloid anhydrobiosis may also rely on the production of natively unfolded proteins.

This presents rotifers as the logical organism to study next, for comparison with our work in tardigrades. We received a culture of the desiccation tolerant *Philodina sp.* from the Barraclough lab, and subcultured them with the *E. coli* strain OP50 and baker's yeast. To make viscosity measurements in the hydrated rotifers, we stained them with 2.5µM BG-BODIPY overnight. They seemed to tolerate this staining, as they were still mobile and feeding the following day. In order to immobilise them, we added 1% chloroform to the water, as we had done with the tardigrades, but this led to contraction of the organisms into a characteristic barrel shape (Marotta *et al.*, 2010). This meant it would be difficult to identify individual organs and structures during FLIM analysis, however we carried on as we believed gross viscosity changes could still be seen between hydrated and dehydrated organisms.

The retracted rotifers had a fairly uniform lifetime across the organism of around 1500ps, with some higher lifetimes at the boundary between organs and at the head and the tail (Figure 5.6a). There were large spots of very low lifetime in the midgut, which we attribute to autofluorescence from the *E. coli* or yeast the rotifers were fed.

5.2.7 Rotifer desiccation leads to a sharp increase in viscosity

We had now demonstrated that BG-BODIPY could be used to detect distinct responses to stressors within a single species. We were now curious as to what it could reveal about responses to the same stressor across different species. Rotifer desiccation survival, like tardigrade anhydrobiosis, relies on the expression of IDPs, so we wanted to find out if we would observe the same inexplicable drop in lifetime in rotifer tuns as in slowly dried tardigrade tuns. Rotifer desiccation took place over a much longer timespan than that of tardigrades, with the labelled organisms first being incubated in >90% humidity for 24 hours, and then moved to ~40% humidity chamber for a further 96 hours.

After desiccation, all of the rotifers successfully formed tuns. The plate they were dried on was held at an angle during the drying process, resulting in all of the tuns coming to rest at one edge of the wells, which allowed us to collect FLIM images of numerous organisms over a short period of time (Figure 5.6b). FLIM revealed that BG-BODIPY within all of the tuns reported a sharp increase in viscosity, with the fluorescence lifetime increasing from an average of ~1500ps to ~3000ps. This represents an average viscosity of around 700cP in the desiccated tuns (Figure 5.6c).

This result was what we had initially assumed would happen with the tardigrade tuns in the slow drying condition, making that result all the stranger. CAHS and SAHS proteins were actually discovered in an attempt to identify LEA proteins and other heat soluble proteins in *R. varieornatus*, and are thought to largely act in place of LEA proteins, which appear to be absent in tardigrades, other than in the mitochondria (Yamaguchi *et al.*, 2012; Tanaka *et al.*, 2015). While CD of hydrated SAHS1 revealed the presence of β-structures, hydrated CAHS1 was largely disordered similar to LEA proteins (Yamaguchi *et al.*, 2012). Further, in conditions that mimicked dehydration, both proteins gained an α-helical structure, as is the case in LEA proteins, however the α-helical motifs in CAHS proteins had an additional negatively charged region compared with that of LEA proteins, indicating that its helices may be narrower, possibly protecting it from hydrophobic or electro-static interaction with other molecules of too much magnitude. It seems doubtful that this change could account for the considerable difference in lifetime between desiccated tardigrade and rotifer tuns.

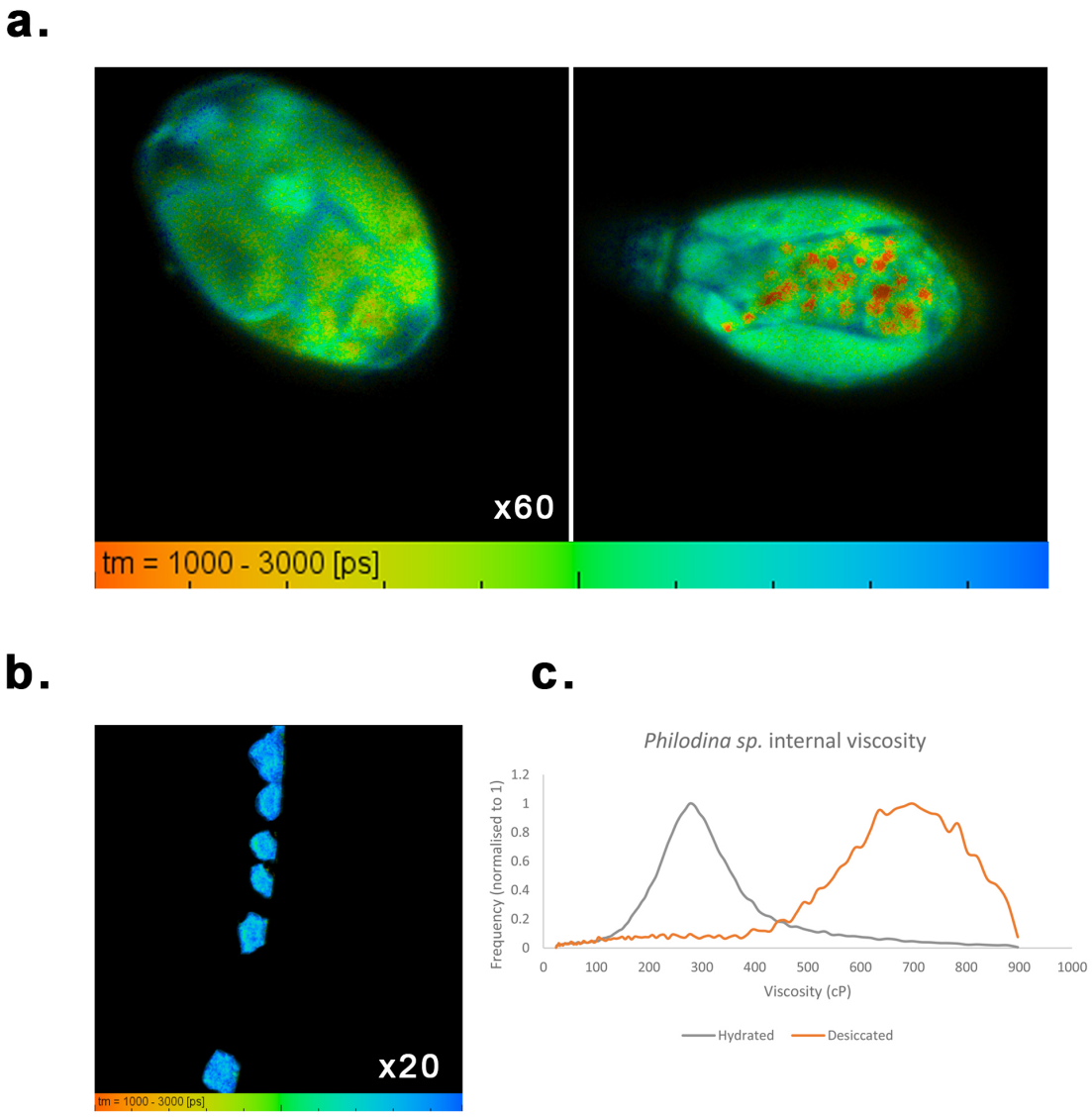

Figure 5.6: **Desiccation of rotifers results in tuns with increased viscosity.** a. FLIM images of hydrated rotifers. In respones to chloroform, the rotifers retract, making it difficult to discern all of the anatomical features. The red spots in the right hand image are likely autofluorescence of bacteria in the gut. b. A FLIM image of a row of 6 rotifer tuns that had formed in a line agains the edge of a well. All tuns demonstrate a fairly uniform increase in lifetime, which, as can be seen in c., corresponds to a large upward shift in viscosity.

5.3 Discussion

Here we have demonstrated that BG-BODIPY can incorporate into the various anatomical structures of the tardigrade *H. exemplaris* and measure the microvis-

cosity in its cells. Lifetime measurements clearly demonstrate disparate microviscous environments in different organs. BG-BODIPY that has simply stuck to the chitinous structures of the carapace or the apophyses of the pharynx or the claws reports a low viscosity environment, equivalent to that of the external aqueous medium, which makes sense. The actual cells with the lowest apparent viscosity appear to be the storage cells, which float throughout the body cavity in eutardigrades. While the energetic reserves of tardigrades has been linked to anhydrobiotic survival (Crowe & Higgins, 1967; Kinchin, 1993), this would seem to conflict with the current view that anhydrobiosis is an ametabolic state (Ingemar, 2001). However, one could foresee a way in which there could be a requisite metabolic expenditure for successfully entering anhydrobiosis.

FLIM's primary advantage to fluorescence intensity based measurements of viscometers is that it is concentration independent. Because of this, we were able to label tardigrade cells with BG-BODIPY without having to be primarily concerned about any concentration differences between cells. This is useful as we are uncertain as to how exactly BG-BODIPY distributes within the organism. Whilst BG-BODIPY was designed to be used in conjunction with SNAP-tag for labelling of specific organelles, here we demonstrate that it can be used to make average viscosity measurements of whole cells and organs. This highlights the adaptivity of BG-BODIPY for use on many different scales and resolutions.

BG-BODIPY provides a unique means of studying tardigrade cryptobiotic processes, as it allows us to measure which tuns have successfully vitrified without having to rehydrate them and count the survivors. While it is unfortunate that BG-BODIPY lifetime is unable to accurately measure the viscosity in anhydrobiotic tardigrades, the uniform short lifetime it reports is unambiguously distinct from the lifetime range for both tardigrades in both the hydrated and low humidity drying conditions. Moreover, measurements in the intensity domain are consistent with the hypothesis that anhydrobiotic tardigrades indeed express increased internal viscosity. This gives us high confidence that it is therefore indicative of a molecular process occurring in successful anhydrobiosis.

BG-BODIPY staining also appears to give us insight into the differing internal states of tuns formed in response to varying stressors. The viscosities reported within tuns formed in response to acute osmotic stress, particularly within the visible lower viscosity feeding apparatus, show that the osmotic stress response

appears to be a very different process from the dessication response. The preservation of the feeding anatomy with its characteristic lower lifetime contrasts with the homogeneous lifetimes observed throughout the whole of tuns formed in response to both fast and slow drying. Further, our observation that after 24 hours of osmotic stress, tardigrades reverted from tun states and appeared to die, indicates that if there is an osmobiotic response, it is extremely limited in comparison to anhydrobiosis.

What is more, BG-BODIPY appears to be able to detect differences in the anhydrobiotic processes of different organisms. Despite the fact that both bdelloid rotifer and tardigrade species used heat soluble, intrinsically disordered proteins to maintain lipid integrity and prevent protein aggregation during desiccation, the lifetimes reported by BG-BODIPY in tuns of each organism were wildly different. We were unable to explain the aberrant behaviour of BG-BODIPY in slowly dried tardigrade tuns, and were even more puzzled when the viscosity change in rotifers matched our initial expectations.

These results highlight the usefulness of BG-BODIPY for studying the microviscous environment on the order of whole multicellular microorganisms. Hitherto, we have been intent on demonstrating the ability to target BG-BODIPY to specific proteins expressed with a SNAP-tag, however this shows the probe is more versatile than initially thought.

Chapter 6

Discussion

6.1 Summary of results

We first demonstrated here that the novel dye BG-BODIPY is suitable for live cell imaging by proving it is non-toxic to cells over long periods and the levels of its background labelling can be reduced to that of autofluorescence by back extracting the dye with delipidated BSA. We then calibrated the probe over a range of viscosities by making measurements of BG-BODIPY's lifetime and intensity at various glycerol concentrations. We also measured its lifetime and intensity from pH 4-10 and showed that the probe is pH insensitive.

We had also produced a couple probes with longer-length linkers, however these had reduced dynamic ranges and were thus not utilised extensively in the context of this thesis. They were still, however, sensitive to viscosity and could be appropriate at future junctures.

Next, partially as a proof of principle, but also because it is of interest in its own right, we attempted to map HeLa cells in terms of viscosity. To this end, we used CRISPR knock-in cell lines created by my colleague Lior Pytowski that expressed targeting sequences for most of the major organelles in conjunction with the SNAP-tag enzyme and mCherry from the AAVS1 locus. We attempted to measure the viscosity of these organelles in both the intensity and lifetime domains. Due to the fact that we were unable to calibrate the ratiometric measurements of mCherry and BG-BODIPY, we were unable to make absolute measurements in the intensity domain and had to settle for relative comparisons of the organelles.

The lifetime measurements were also complicated by the presence of mCherry, the

lifetime of which confounded and masked the BG-BODIPY lifetime. However, we were able to bleach the mCherry lifetime prior to BG-BODIPY labelling, which appears to have reduced the mCherry signal enough to allow us to make lifetime measurements. We were able to make lifetime measurements for several of the organelles, but expression in some of the other cell lines was too weak to generate a sufficient signal to make measurements. One thing we noticed was that the AAVS1 CRISPR line and our transient expression of the COX8/SNAP-tag construct targeted BG-BODIPY to different compartments within the mitochondria, and resulted in a large difference in the reported lifetime.

We were then curious as to whether BG-BODIPY could be targeted to the more transient membraneless organelles. We transiently expressed a TDP43/SNAP-tag construct in HeLa cells and then treated these cells with $ZnCl_2$ overnight and saw that the TDP43 (and therefore BG-BODIPY) concentrated in stress granules. These stress granules had a significantly higher viscosity than that experienced by BG-BODIPY attached to TDP43 free in the nucleoplasm and cytoplasm. The stress granules could then be dissolved with mitoxantrone.

Having shown that individual organelles could be targeted with BG-BODIPY, we then set our sights on a smaller target: the NPC. We targeted BG-BODIPY to the cytoplasmic face of the NPC using transient expression of a nup214/SNAP-tag construct. We were able to visualise individual pores using confocal microscopy, but the overexpression caused the formation of large cytoplasmic aggregates of protein. We performed FLIM and found a relatively high lifetime, ~2.3ns. The large aggregates had nearly an identical lifetime. The lifetime within the NPCs could be dramatically reduced by treatment with mitoxantrone.

Because of the problems with overexpression, we set out to create CRISPR knock-in lines tagging several nups with the SNAP-tag, allowing it to be expressed at endogenous levels. We created cell lines that expressed the SNAP-tag enzyme as a fusion protein with nup214, nup153, and nup98. These lines were incredibly difficult to make, as we did not design our experiment so that a second tag or marker was also knocked in. We attempted to make additional cell lines knocking in the SNAP-tag enzyme to further nups along with a puromycin resistance marker, however none of the surviving colonies following selection appeared to be positive, as none of them labelled with BG-BODIPY.

FLIM of the nup214, nup153, and nup98 cell lines revealed that, while there was considerable variation between cells within the cell lines, the different cell lines had statistically significant differences in their reported lifetimes. All three lines showed similar responses to mitoxantrone and lipoamide, with mitoxantrone inducing a large reduction in lifetime and the appearance of a bi- or trimodal distribution, while lipoamide resulted in only minor decreases in lifetime. In keeping with this, mitoxantrone caused the breakdown of the permeability barrier, allowing mCherry-NLS to escape from the nucleus, while lipoamide did not.

We then attempted to disrupt NPCs by reducing the O-GlcNAcylation of FG-nups through inhibition of *O*-GlcNAc transferase, which has been shown to cause a breakdown in the selective permeability barrier and leakage through the NPC (Zhu *et al.*, 2016). Unfortunately, when we treated cells with Ac5SGlcNAc, we saw no changes to the lifetime of BG-BODIPY, and observed no leakage of mCherry-NLS from the nucleus.

The scale of our investigation then shifted to that of whole organisms. We demonstrated that BG-BODIPY can be used to label cells all throughout several semi-terrestrial species, chiefly *H. exemplaris* and *Philodina sp.* Labelling overnight with BG-BODIPY resulted in the dye being concentrated in every organ of tardigrades, which allowed us to make detailed confocal and FLIM images of the organisms. FLIM analysis revealed the majority of the cells in the muscle and neural tissues, as well as the gonads, had a fairly uniform, low lifetime while the storage cells and the BG-BODIPY stuck to the chitinous claws and stylets all had lower lifetimes.

When we desiccated tardigrades following two desiccation regimes, fast and slow, we found that the two regimes resulted in very different lifetimes from within the tuns that formed. The fast dried tuns appeared to retain the initial lifetime peak, as well as gain a second, longer lifetime distribution, while the slow dried tuns exhibited a strange behaviour. Though tremendously bright, they had very short lifetimes, on the order or 500-700ps. This is still inexplicable to us, but represents a unique process occurring during the tardigrade anhydrobiotic response. The internal viscous environment of tuns formed in response to acute osmotic stress differed from both that of the slow drying and fast drying conditions, highlighting that this response likely has different molecular underpinnings.

We then looked at another desiccation resistant organism the bdelloid rotifer *Philodina sp.* This species retracted into itself upon exposure to chloroform, which

prohibited as detailed an analysis of its internal viscosity in physiological conditions. However, when desiccated at controlled humidity, the rotifer tuns produced a change in lifetime much more in line with how we imagined tardigrade tun formation would look: a sharp, homogeneous increase in lifetime. This showed that BG-BODIPY is able to discern between the anhydrobiotic responses of two different organisms.

6.2 Inferences from results

I believe, that while there is still much work to be done with BG-BODIPY to demonstrate its usefulness, we have shown BG-BODIPY is a promising new probe for measuring viscosity *in vivo* in a variety of systems.

The vast majority of work on protein phase transition and aggregation dynamics is performed *in vitro*. Our lab's own past work on IAPP and Abeta gelation has taken place *in vitro* at high concentrations, despite our efforts to keep experimental setups as physiological as possible (Jean *et al.*, 2016). Seminal work on phase transitions in FUS were performed at very high concentrations and required temperature shifts to induce LLPS (Patel *et al.*, 2015). BG-BODIPY's ability to monitor LLPS and potentially aggregation processes whilst in a cellular environment represents a dramatic paradigm shift in this field. To be able to test the effects of compounds on these processes in live cells while getting real time information on the microviscous environment of a protein of interest is truly a boon.

Our results indicate that membrane bound (and membraneless) organelles within the cell have distinct viscous environments, a notion that is echoed by Chambers *et al.* (2018). It seems reasonable to suggest that these discrete viscosities are likely to be just as vital to the proper functioning of these organelles as their unique pHs. Disruption of these distinct microviscous environments likely occurs (or is a causal factor) in pathological conditions. While previous studies of the effects in changes in microviscosity on disease states was limited to the plasma membrane, BG-BODIPY represents an opportunity to study a host of other cellular environments.

When we had first conceptualised this project, we had imagined that in order to determine whethere the phase inside the NPC central channel was a hydrogel, we would compare the lifetime of BG-BODIPY within the central channel to that of BG-BODIPY in hydrogels we would make *in vitro*. However, when we used

BG-BODIPY to monitor gelation in two very different systems, we had to conclude there is no 'characteristic' hydrogel microviscosity. It was serendipitous, then, that I had a conversation with Richard Wheeler and he informed me that mitoxantrone might be useful for our purposes. Treatment of NPCs with mitoxantrone became the strongest indicator we have that the FG-nups within the central channel form a hydrogel, or are at least a distinct liquid phase from the cytoplasm, in physiological conditions. Mitoxantrone has a broad action against most condensates within the cell, while lipoamide acts specifically on SGs. Consistent with this, lipoamide did not cause a breakdown of the permeability barrier and caused only modest reductions in BG-BODIPY lifetime, while mitoxantrone caused significant leakage across the NPC and a large reduction in lifetime. This is some of the first evidence performed *in vivo* supporting the selectivity phase model.

One of the interesting themes that continued to pop up throughout my work was the usefulness of mitoxantrone for interrogating a variety of disparate cellular processes. Not only was it able to dissolve stress granules, but at the same concentrations it was shown to alter the micorviscous environment of the NPC central channel. Mitoxantrone's mechanism of action in these instances is unknown. In cancer treatment, mitoxantrone is used as type II topoisomerase inhibitor to prevent DNA replication in tumor cells (Mazerski, 1998). It works by intercalating itself between DNA nucleotides. A similar mechanism could be responsible for mitoxantrone's behaviour in preventing phase separation; it could be associating with molecules involved in such a way as to prevent their assembly. In systems with RNA present, it has been shown mitoxantrone can disrupt condensates, likely through intercalating with base pairs in the RNA (Fang *et al.*, 2019). However, it has the same effect in *in vitro* systems that lack RNA, which the authors suggest is possibly due to mitoxantrone reducing cation-π interactions required for LLPS (Wheeler *et al.*, 2019).

There are clearly limitations to using BG-BODIPY that need to be considered before deciding its use is appropriate for a given experiment. In two instances in this thesis – the IAPP gelation experiments and the tardigrade desiccation – we have highlighted an aberrant behaviour where BG-BODIPY appears to 'fall out' of its useful reporting range and gives an inaccurate low lifetime. Both instances were cases in which we were monitoring protein aggregation, so it seems likely that in certain instances, BG-BODIPY becomes intercalated in the aggregating proteins

in a fashion that constrains the probe in such a way that it no longer can accurately report. Or, beyond steric hindrance, it could be possible that BG-BODIPY is interacting with side chains that quench its fluorescence.

6.3 Future directions

It is probably clear from the rest of this body of work, that we could come up with dozens of other applications for BG-BODIPY that we would like to trial. If anything, the struggle with this project has been to rein in the number of disparate experimental threads we worked on. I will attempt to limit the scope of the potential future projects I outline here to those that directly follow on from the chapters within this thesis, although there were many more threads we were tempted to pull.

To give but one example of a path we were unable to follow to its conclusion, we had imagined an entire set of experiments based on the finding in Section 3.2.7 (that likely would surprise nobody but ourselves) that BG-BODIPY targeted to the outside of the plasma membrane encounters a microviscous environment distinct from that of the surrounding media. We were keen to follow on from this with the creation of a construct that would attach the SNAP-enzyme to the distal end of a rigid extracellular domain of CD45. This would have allowed us to map the glycocalyx in terms of viscosity at various distances from the plasma membrane. Unfortunately, after expressing the construct in HeLa cells and labelling with BG-BODIPY, we could not see any targeting of the probe. Had I had more time, it would have been great to be able to ascertain why this construct did not work.

I could enumerate a number of such abortive projects that we would love to be able to attend to going forward, but for the sake of brevity, and to prevent this thesis from looking any more scattershot than it is, I will attempt to limit the scope of this section to experiments that follow on logically from what has already been presented in the preceding chapters.

Chapter 3 presents a proof of principle and our calibration of the probe, but it is our initial attempts at mapping the cell in terms of viscosity that could really be taken further in the future. We were unable to determine a means of calibrating the ratiometric measurements of BG-BODIPY with mCherry, and addressing this would be a priority going forward. Being able to make absolute viscosity measurements in the intensity domain would be of great benefit to this research.

As it stands, our data from the work with the various CRISPR'd SNAP-tag targeting lines raises more questions than it answers. It appears that the viscous environment changes as one moves through the secretory pathway, which, if true, has all sorts of implications for the sorting of proteins in this pathways. It would be important in the future to, in the future, make viscosity measurements of a protein making its way through the secretory pathway as cargo, in order to see whether a protein passing through the system experiences the same changes in viscosity as we found by targeting BG-BODIPY to the individual organelles. An ideal candidate for this would be a mutated viral protein of the vesicular somatic virus (VSV), VSV-G, which is unable to exit the ER at 42° but is then able to be released in a wave at 37° (Bergmann, 1989). Being able to tag VSV-G with BG-BODIPY would therefore allow us to measure cargo moving through the secretory pathway in a synchronous fashion.

We were also interested in carrying out further experiments on mitochondria labelled with BG-BODIPY. The literature is full of experiments perturbing mitochondria in various ways to induce swelling and test molecular rotors targeted there. Chambers *et al.* (2018) used changes in extracellular osmolality and ionomycin treatments to test this. We had plans to replicate these studies with our system, in both whole cells and isolated mitochondria.

The section that requires the most continued work going forward is Chapter 4. CRISPR was not in my repertoire, and I would like to have another shot at creating the nup/SNAP-tag cell lines now that I have made connections with people in the department with far more experience and expertise than was available when I started out. In addition to perhaps recreating the cell lines I've already made with another tag (this could even be another fluorophore now that we know we can bleach any interfering signal), I would like to tag a few more nucleoporins with the SNAP-tag. Of particular interest is nup62, which is cleaved from a 186 kDa precursor protein alongside nup98, and then becomes part ot the nup62 subcomplex which forms rings within the inner core of the channel (Fontoura *et al.*, 1999; Guan *et al.*, 2017). There is also evidence that nup62 has a role in maintaining centrosome integrity during mitosis, as nup62 depletion results in a number of dramatic problems with cell division (Hashizume *et al.*, 2013).

With more nucleoporins tagged at more points along the central channel, we would be able to see if there are further variations in the microviscous environment at more points within the channel.

We would also be interested in attempting to improve the resolution of our FLIM instrumentation going forward so that we might be able to make measurements of individual pore complexes. This would open a whole set of experiments we had initially contemplated when first setting out on this project, but had to abandon when it became clear we would not be able to resolve the individual pores with our current configuration. To give but one possibility, there is some evidence that the composition of nups within NPCs can have significant heterogeneity, not between different cell lines, but at different points in the architecture of a single nucleus (Kinoshita *et al.*, 2012). This means we may not be getting the full picture of the microviscosity by sampling at only a single plane for a given cells, and there are possibly variations in the viscous properties of the putative gels within NPCs at different points in the nucleus due to their varying nup composition.

We were puzzled by our inability to reproduce Ac5SGlcNAc's disruption of NPC function through decreases in O-GLcNAcylation of FG-nups. Though stored correctly, we received Ac5SGlcNAc from the Vocadlo group quite some time before we utilised it, leaving the possibility that it might have expired. Alternatively, we could simply need to optimise the treatment, and going forward we would love the time to attempt to retry this experiment.

Chapter 5 represents, in my opinion, the most satisfyingly complete biological story presented here. From one lunchtime conversation, we were able to produce a body of work demonstrating a completely novel use for BG-BODIPY, and for molecular rotors in general. However, as with anything in science, there are still threads to be pulled in this story, and in the future we have a number of experiments we would love to carry out in this vein.

While we used BG-BODIPY to characterise the desiccation response of two organisms, there is a third taxon of desiccation tolerant invertebrates we would have liked to have been able to study: nematodes. Nematodes would be of interest because they use the production of trehalose in addition to LEA proteins to survive desiccation, unlike tardigrades and rotifers (Goyal *et al.*, 2003; Erkut *et al.*, 2011). We would like to see whether this would be discernible when nematodes are labelled with BG-BODIPY. I made some initial measurements on nematodes isolated from moss, and determined that BG-BODIPY labels worms well, however these were of an indeterminate species and we would perform future work on a clonal line.

Given the strange behaviour of BG-BODIPY in *H. exemplaris*, we would also like to pursue expressing CAHS, MAHS, and SAHS proteins *in vitro* and desiccating the isolated proteins with BG-BODIPY in a range of conditions in order to better understand this process.

References

[,] (No Title).

[Abedini and Schmidt, 2013a] Abedini, A. and Schmidt, A. M. (2013a). Mechanisms of islet amyloidosis toxicity in type 2 diabetes.

[Abedini and Schmidt, 2013b] Abedini, A. and Schmidt, A. M. (2013b). Mechanisms of islet amyloidosis toxicity in type 2 diabetes.

[Ahmed, 2015] Ahmed, E. M. (2015). Hydrogel: Preparation, characterization, and applications: A review.

[Andersen et al., 2017] Andersen, M. K., Folkersen, R., MacMillan, H. A., and Overgaard, J. (2017). Cold acclimation improves chill tolerance in the migratory locust through preservation of ion balance and membrane potential. *The Journal of Experimental Biology*, 220(3):487–496.

[Arai et al., 2006] Arai, T., Hasegawa, M., Akiyama, H., Ikeda, K., Nonaka, T., Mori, H., Mann, D., Tsuchiya, K., Yoshida, M., Hashizume, Y., and Oda, T. (2006). TDP-43 is a component of ubiquitin-positive tau-negative inclusions in frontotemporal lobar degeneration and amyotrophic lateral sclerosis. *Biochemical and Biophysical Research Communications*, 351(3):602–611.

[Aulas et al., 2012] Aulas, A., Stabile, S., and Vande Velde, C. (2012). Endogenous TDP-43, but not FUS, contributes to stress granule assembly via G3BP. *Molecular Neurodegeneration*, 7(1).

[Baron et al., 2013] Baron, D. M., Kaushansky, L. J., Ward, C. L., Sama, R. R. K., Chian, R.-J., Boggio, K. J., Quaresma, A. J. C., Nickerson, J. A., and Bosco, D. A. (2013). Amyotrophic lateral sclerosis-linked FUS/TLS alters stress granule assembly and dynamics. *Molecular Neurodegeneration*, 8(1):30.

[Baty et al., 2000] Baty, A. M., Eastburn, C. C., Techkarnjanaruk, S., Goodman, A. E., and Geesey, G. G. (2000). Spatial and temporal variations in chitinolytic gene expression and bacterial biomass production during chitin degradation. *Applied and Environmental Microbiology*, 66(8):3574–3585.

[Bayry et al., 2012] Bayry, J., Aimanianda, V., Guijarro, J. I., Sunde, M., and Latgé, J.-P. (2012). Hydrophobins—Unique Fungal Proteins. *PLoS Pathogens*, 8(5):e1002700.

[Becker, 2015] Becker, W. (2015). *The bh TCSPC Handbook*. 6 edition.

[Bergmann, 1989] Bergmann, J. E. (1989). Using Temperature-Sensitive Mutants of VSV to Study Membrane Protein Biogenesis. *Methods in Cell Biology*, 32(C):85–110.

[Berlin and Fera, 1977] Berlin, R. D. and Fera, J. P. (1977). Changes in membrane microviscosity associated with phagocytosis: effects of colchicine. *Proceedings of the National Academy of Sciences of the United States of America*, 74(3):1072–6.

[Bespalova, 2019] Bespalova, I. (2019). Tardigrade Anatomy — Ask A Biologist.

[Black et al., 2015] Black, K. A., Lin, B. F., Wonder, E. A., Desai, S. S., Chung, E. J., Ulery, B. D., Katari, R. S., and Tirrell, M. V. (2015). Biocompatibility and Characterization of a Peptide Amphiphile Hydrogel for Applications in Peripheral Nerve Regeneration. *Tissue Engineering Part A*, 21(7-8):1333–1342.

[Bolisetty et al., 2012] Bolisetty, S., Harnau, L., Jung, J.-m., and Mezzenga, R. (2012). Gelation, Phase Behavior, and Dynamics of β-Lactoglobulin Amyloid Fibrils at Varying Concentrations and Ionic Strengths. *Biomacromolecules*, 13(10):3241–3252.

[Buell et al., 2014] Buell, A. K., Galvagnion, C., Gaspar, R., Sparr, E., Vendruscolo, M., Knowles, T. P., Linse, S., and Dobson, C. M. (2014). Solution conditions determine the relative importance of nucleation and growth processes in α-synuclein aggregation. *Proceedings of the National Academy of Sciences of the United States of America*, 111(21):7671–7676.

[Butko et al., 2001a] Butko, P., Buford, J. P., Goodwin, J. S., Stroud, P. A., McCormick, C. L., and Cannon, G. C. (2001a). Spectroscopic evidence for amyloid-like interfacial self-assembly of hydrophobin Sc3. *Biochemical and Biophysical Research Communications*, 280(1):212–215.

[Butko et al., 2001b] Butko, P., Goodwin, J., Buford, J., and Stroud, P. (2001b). B-Sheet Stacking in Interfacial Self-Assembly of Hydrophobin Sc3. *Biophysical Journal*, 80(1).

[Charge et al., 1995] Charge, S. B. P., de Koning, E. J. P., and Clark, A. (1995). Effect of pH and insulin on fibrillogenesis of islet amyloid polypeptide in vitro. *Biochemistry*, 34(44):14588–14593.

[Chavez et al., 2019] Chavez, C., Cruz-Becerra, G., Fei, J., Kassavetis, G. A., and Kadonaga, J. T. (2019). The tardigrade damage suppressor protein binds to nucleosomes and protects DNA from hydroxyl radicals. *eLife*, 8.

[Clark and Nilsson, 2004] Clark, A. and Nilsson, M. R. (2004). Islet amyloid: A complication of islet dysfunction or an aetiological factor in Type 2 diabetes?

[Colombrita et al., 2009] Colombrita, C., Zennaro, E., Fallini, C., Weber, M., Sommacal, A., Buratti, E., Silani, V., and Ratti, A. (2009). TDP-43 is recruited to stress granules in conditions of oxidative insult. *Journal of Neurochemistry*, 111(4):1051–1061.

[Costerton et al., 1987] Costerton, J. W., Cheng, K. J., Geesey, G. G., Ladd, T. I., Nickel, J. C., Dasgupta, M., and Marrie, T. J. (1987). Bacterial Biofilms in Nature and Disease. *Annual Review of Microbiology*, 41(1):435–464.

[Cox et al., 2007] Cox, A. R., Cagnol, F., Russell, A. B., and Izzard, M. J. (2007). Surface Properties of Class II Hydrophobins from Trichoderma reesei and Influence on Bubble Stability. *Langmuir*, 23(15):7995–8002.

[Crick et al., 2013] Crick, S. L., Ruff, K. M., Garai, K., Frieden, C., and Pappu, R. V. (2013). Unmasking the roles of N- and C-terminal flanking sequences from exon 1 of huntingtin as modulators of polyglutamine aggregation. *Proceedings of the National Academy of Sciences of the United States of America*, 110(50):20075–20080.

[Cushman et al., 2010] Cushman, M., Johnson, B. S., King, O. D., Gitler, A. D., and Shorter, J. (2010). Prion-like disorders: Blurring the divide between transmissibility and infectivity.

[Daigle et al., 2013] Daigle, J. G., Lanson, N. A., Smith, R. B., Casci, I., Maltare, A., Monaghan, J., Nichols, C. D., Kryndushkin, D., Shewmaker, F., and Pandey, U. B. (2013). RNA-binding ability of FUS regulates neurodegeneration, cytoplasmic

mislocalization and incorporation into stress granules associated with FUS carrying ALS-linked mutations. *Human Molecular Genetics*, 22(6):1193–1205.

[De Brabander et al., 1988] De Brabander, M., Nuydens, R., Geerts, H., and Hopkins, C. R. (1988). Dynamic behavior of the transferrin receptor followed in living epidermoid carcinoma (A431) cells with nanovid microscopy. *Cell Motility and the Cytoskeleton*, 9(1):30–47.

[Degma et al.,] Degma, P., Degma, P., Bertolani, R., and Guidetti, R. 1 Actual checklist of Tardigrada species (2009-2015, Ver. 28: 31-03-2015).

[Deliconstantinos et al., 1995] Deliconstantinos, G., Villiotou, V., and Stavrides, J. C. (1995). Modulation of particulate nitric oxide synthase activity and peroxynitrite synthesis in cholesterol enriched endothelial cell membranes. *Biochemical Pharmacology*, 49(11):1589–1600.

[Deng et al., 2010] Deng, C., Li, F., Hackett, J. M., Chaudhry, S. H., Toll, F. N., Toye, B., Hodge, W., and Griffith, M. (2010). Collagen and glycopolymer based hydrogel for potential corneal application. *Acta Biomaterialia*, 6(1):187–194.

[Dent et al., 2015a] Dent, M. R., López-Duarte, I., Dickson, C. J., Geoghegan, N. D., Cooper, J. M., Gould, I. R., Krams, R., Bull, J. A., Brooks, N. J., and Kuimova, M. K. (2015a). Imaging phase separation in model lipid membranes through the use of BODIPY based molecular rotors. *Physical Chemistry Chemical Physics*, 17(28):18393–18402.

[Dent et al., 2015b] Dent, M. R., López-Duarte, I., Dickson, C. J., Geoghegan, N. D., Cooper, J. M., Gould, I. R., Krams, R., Bull, J. A., Brooks, N. J., and Kuimova, M. K. (2015b). Imaging phase separation in model lipid membranes through the use of BODIPY based molecular rotors. *Physical Chemistry Chemical Physics*, 17(28):18393–18402.

[Dewey et al., 2011] Dewey, C. M., Cenik, B., Sephton, C. F., Dries, D. R., Mayer, P., Good, S. K., Johnson, B. A., Herz, J., and Yu, G. (2011). TDP-43 Is Directed to Stress Granules by Sorbitol, a Novel Physiological Osmotic and Oxidative Stressor. *Molecular and Cellular Biology*, 31(5):1098–1108.

[Dewey et al., 2012] Dewey, C. M., Cenik, B., Sephton, C. F., Johnson, B. A., Herz, J., and Yu, G. (2012). TDP-43 aggregation in neurodegeneration: Are stress granules the key?

[Dix and Verkman, 1990] Dix, J. and Verkman, A. (1990). Mapping of fluorescence anisotropy in living cells by ratio imaging. Application to cytoplasmic viscosity. *Biophysical Journal*, 57(2):231–240.

[Dombek and Ingram, 1984] Dombek, K. M. and Ingram, L. O. (1984). Effects of ethanol on the Escherichia coli plasma membrane. *Journal of Bacteriology*, 157(1):233.

[Erkut et al., 2011a] Erkut, C., Penkov, S., Khesbak, H., Vorkel, D., Verbavatz, J. M., Fahmy, K., and Kurzchalia, T. V. (2011a). Trehalose renders the dauer larva of caenorhabditis elegans resistant to extreme desiccation. *Current Biology*, 21(15):1331–1336.

[Erkut et al., 2011b] Erkut, C., Penkov, S., Khesbak, H., Vorkel, D., Verbavatz, J. M., Fahmy, K., and Kurzchalia, T. V. (2011b). Trehalose renders the dauer larva of caenorhabditis elegans resistant to extreme desiccation. *Current Biology*, 21(15):1331–1336.

[Espeland and Wetzel, 2001] Espeland, E. M. and Wetzel, R. G. (2001). Complexation, stabilization, and UV photolysis of extracellular and surface-bound glucosidase and alkaline phosphatase: Implications for biofilm microbiota. *Microbial Ecology*, 42(4):572–585.

[Fang et al., 2019] Fang, M. Y., Markmiller, S., Vu, A. Q., Javaherian, A., Dowdle, W. E., Jolivet, P., Bushway, P. J., Castello, N. A., Baral, A., Chan, M. Y., Linsley, J. W., Linsley, D., Mercola, M., Finkbeiner, S., Lecuyer, E., Lewcock, J. W., and Yeo, G. W. (2019). Small-Molecule Modulation of TDP-43 Recruitment to Stress Granules Prevents Persistent TDP-43 Accumulation in ALS/FTD. *Neuron*, 103(5):802–819.e11.

[Ferry, 1980] Ferry, J. (1980). *Viscoelastic Properties of Polymers*. Wiley, New York, NY, USA, 3rd ed. edition.

[Fontaneto et al., 2008] Fontaneto, D., Barraclough, T. G., Chen, K., Ricci, C., and Herniou, E. A. (2008). Molecular evidence for broad-scale distributions in bdelloid rotifers: everything is not everywhere but most things are very widespread. *Molecular Ecology*, 17(13):3136–3146.

[Fontoura et al., 1999] Fontoura, B. M., Blobel, G., and Matunis, M. J. (1999). A conserved biogenesis pathway for nucleoporins: Proteolytic processing of a 186-

kilodalton precursor generates Nup98 and the novel nucleoporin, Nup96. *Journal of Cell Biology*, 144(6):1097–1112.

[Ford et al., 2019] Ford, H. Z., Zeboudj, L., Purvis, G. S., Ten Bokum, A., Zarebski, A. E., Bull, J. A., Byrne, H. M., Myerscough, M. R., and Greaves, D. R. (2019). Efferocytosis perpetuates substance accumulationinsidemacrophagepopulations. *Proceedings of the Royal Society B: Biological Sciences*, 286(1904).

[Frey and Görlich, 2007] Frey, S. and Görlich, D. (2007). A Saturated FG-Repeat Hydrogel Can Reproduce the Permeability Properties of Nuclear Pore Complexes. *Cell*, 130(3):512–523.

[Fueller et al., 2018] Fueller, J., Meurer, M., Herbst, K., Gubicza, K., Kurtulmus, B., Knopf, J. D., Kirrmaier, D., Buchmuller, B., Pereira, G., Lemberg, M. K., and Knop, M. (2018). CRISPR/Cas12a-assisted PCR tagging of mammalian genes. *bioRxiv*, page 473876.

[Fujiwara et al., 2002] Fujiwara, T., Ritchie, K., Murakoshi, H., Jacobson, K., and Kusumi, A. (2002). Phospholipids undergo hop diffusion in compartmentalized cell membrane. *Journal of Cell Biology*, 157(6):1071–1081.

[Fulton, 1982] Fulton, A. B. (1982). How crowded is the cytoplasm? *Cell*, 30(2):345–7.

[Fux et al., 2005] Fux, C. A., Costerton, J. W., Stewart, P. S., and Stoodley, P. (2005). Survival strategies of infectious biofilms.

[Gallaghers et al., 2010] Gallaghers, S. S., Jing, C., Peterka, D. S., Konate, M., Wombacher, R., Kaufman, L. J., Yuste, R., and Cornish, V. W. (2010). A trimethoprim-based chemical tag for live cell two-photon imaging. *ChemBioChem*, 11(6):782–784.

[Geerts et al., 1987] Geerts, H., De Brabander, M., Nuydens, R., Geuens, S., Moeremans, M., De Mey, J., and Hollenbeck, P. (1987). Nanovid tracking: a new automatic method for the study of mobility in living cells based on colloidal gold and video microscopy. *Biophysical Journal*, 52(5):775–782.

[Giovannini et al., 2018] Giovannini, I., Altiero, T., Guidetti, R., and Rebecchi, L. (2018). Will the Antarctic tardigrade *Acutuncus antarcticus* be able to withstand environmental stresses related to global climate change? *The Journal of Experimental Biology*, 221(4):jeb160622.

[Goyal et al., 2003] Goyal, K., Tisi, L., Basran, A., Browne, J., Burnell, A., Zurdo, J., and Tunnacliffe, A. (2003). Transition from natively unfolded to folded state induced by desiccation in an anhydrobiotic nematode protein. *Journal of Biological Chemistry*, 278(15):12977–12984.

[Gritsch and Motta, 2015] Gritsch, L. and Motta, F. L. (2015). History and Applications of Hydrogels.

[Guan et al., 1995] Guan, T., Müller, S., Klier, G., Panté, N., Blevitt, J. M., Haner, M., Paschal, B., Aebi, U., and Gerace, L. (1995). Structural analysis of the p62 complex, an assembly of O-linked glycoproteins that localizes near the central gated channel of the nuclear pore complex. *Molecular Biology of the Cell*, 6(11):1591–1603.

[Guidetti et al., 2011] Guidetti, R., Altiero, T., Bertolani, R., Grazioso, P., and Rebecchi, L. (2011). Survival of freezing by hydrated tardigrades inhabiting terrestrial and freshwater habitats. *Zoology*, 114(2):123–128.

[Guidetti and Jönsson, 2002] Guidetti, R. and Jönsson, K. I. (2002). Long-term anhydrobiotic survival in semi-terrestrial micrometazoans. *Journal of Zoology*, 257(2):S095283690200078X.

[Guigas et al., 2007] Guigas, G., Kalla, C., and Weiss, M. (2007). Probing the Nanoscale Viscoelasticity of Intracellular Fluids in Living Cells. *Biophysical Journal*, 93(1):316.

[Guo et al., 2019] Guo, L., Fare, C. M., and Shorter, J. (2019). Therapeutic Dissolution of Aberrant Phases by Nuclear-Import Receptors.

[Gupta et al., 2016] Gupta, N., Reja, S. I., Bhalla, V., Gupta, M., Kaur, G., and Kumar, M. (2016). A bodipy based fluorescent probe for evaluating and identifying cancer, normal and apoptotic C6 cells on the basis of changes in intracellular viscosity. *Journal of Materials Chemistry B*, 4(11):1968–1977.

[Hackman et al., 2013] Hackman, P., Sarparanta, J., Lehtinen, S., Vihola, A., Evilä, A., Jonson, P. H., Luque, H., Kere, J., Screen, M., Chinnery, P. F., Åhlberg, G., Edström, L., and Udd, B. (2013). Welander distal myopathy is caused by a mutation in the RNA-binding protein TIA1. *Annals of Neurology*, 73(4):500–509.

[Haidekker et al., 2006] Haidekker, M. A., Brady, T. P., Lichlyter, D., and Theodorakis, E. A. (2006). A ratiometric fluorescent viscosity sensor. *Journal of the American Chemical Society*, 128(2):398–399.

[Hall-Stoodley et al., 2004] Hall-Stoodley, L., Costerton, J. W., and Stoodley, P. (2004). Bacterial biofilms: From the natural environment to infectious diseases.

[Hashimoto et al., 2016] Hashimoto, T., Horikawa, D. D., Saito, Y., Kuwahara, H., Kozuka-Hata, H., Shin-I, T., Minakuchi, Y., Ohishi, K., Motoyama, A., Aizu, T., Enomoto, A., Kondo, K., Tanaka, S., Hara, Y., Koshikawa, S., Sagara, H., Miura, T., Yokobori, S.-i., Miyagawa, K., Suzuki, Y., Kubo, T., Oyama, M., Kohara, Y., Fujiyama, A., Arakawa, K., Katayama, T., Toyoda, A., and Kunieda, T. (2016). Extremotolerant tardigrade genome and improved radiotolerance of human cultured cells by tardigrade-unique protein. *Nature Communications*, 7(1):12808.

[Hashimoto and Kunieda, 2017] Hashimoto, T. and Kunieda, T. (2017). DNA Protection Protein, a Novel Mechanism of Radiation Tolerance: Lessons from Tardigrades. *Life (Basel, Switzerland)*, 7(2).

[Hashizume et al., 2013] Hashizume, C., Moyori, A., Kobayashi, A., Yamakoshi, N., Endo, A., and Wong, R. W. (2013). Nucleoporin Nup62 maintains centrosome homeostasis. *Cell Cycle*, 12(24):3804–3816.

[Heidemann et al., 2017] Heidemann, N. W. T., Smith, D. K., Hygum, T. L., Stapane, L. ., Clausen, L. K. B., Jørgensen, A. ., and Møbjerg, . . (2017). Osmotic stress tolerance in semi-terrestrial tardigrades. *Linnean Society. Zoological Journal*, 178(4):912–918.

[Heidemann et al., 2016] Heidemann, N. W. T., Smith, D. K., Hygum, T. L., Stapane, L., Clausen, L. K. B., Jørgensen, A., Hélix-Nielsen, C., and Møbjerg, N. (2016). Osmotic stress tolerance in semi-terrestrial tardigrades. *Zoological Journal of the Linnean Society*, 178(4):912–918.

[Hengherr et al.,] Hengherr, S., BrümmerBr, F., Schill, R. O., and Steffen Hengherr, C. Anhydrobiosis in tardigrades and its effects on longevity traits.

[Hengherr et al., 2009] Hengherr, S., Worland, M. R., Reuner, A., Brümmer, F., and Schill, R. O. (2009). Freeze tolerance, supercooling points and ice formation: comparative studies on the subzero temperature survival of limno-terrestrial tardigrades. *The Journal of experimental biology*, 212(Pt 6):802–7.

[Heuser, 1989] Heuser, J. (1989). Changes in lysosome shape and distribution correlated with changes in cytoplasmic pH. *Journal of Cell Biology*, 108(3):855–864.

[Horikawa et al., 2009] Horikawa, D. D., Iwata, K.-I., Kawai, K., Koseki, S., Okuda, T., and Yamamoto, K. (2009). High Hydrostatic Pressure Tolerance of Four Different Anhydrobiotic Animal Species. *Zoological Science*, 26(3):238–242.

[Hosny et al., 2013] Hosny, N. A., Fitzgerald, C., Tong, C., Kalberer, M., Kuimova, M. K., and Pope, F. D. (2013). Fluorescent lifetime imaging of atmospheric aerosols: A direct probe of aerosol viscosity. *Faraday Discussions*, 165:343–356.

[Hosny et al., 2016] Hosny, N. A., Fitzgerald, C., Vyšniauskas, A., Athanasiadis, A., Berkemeier, T., Uygur, N., Pöschl, U., Shiraiwa, M., Kalberer, M., Pope, F. D., and Kuimova, M. K. (2016). Direct imaging of changes in aerosol particle viscosity upon hydration and chemical aging. *Chemical Science*, 7(2):1357–1367.

[Hungerford et al., 2009] Hungerford, G., Allison, A., McLoskey, D., Kuimova, M. K., Yahioglu, G., and Suhling, K. (2009). Monitoring sol-to-gel transitions via fluorescence lifetime determination using viscosity sensitive fluorescent probes. *Journal of Physical Chemistry B*, 113(35):12067–12074.

[Ifkovits et al., 2010] Ifkovits, J. L., Tous, E., Minakawa, M., Morita, M., Robb, J. D., Koomalsingh, K. J., Gorman, J. H., Gorman, R. C., and Burdick, J. A. (2010). Injectable hydrogel properties influence infarct expansion and extent of postinfarction left ventricular remodeling in an ovine model. *Proceedings of the National Academy of Sciences of the United States of America*, 107(25):11507–11512.

[Ingemar, 2001] Ingemar, J. K. (2001). The Nature of Selection on Anhydrobiotic Capacity in Tardigrades. *Zoologischer Anzeiger*, 240:409–417.

[Jean et al., 2016] Jean, L., Lee, C. F., Hodder, P., Hawkins, N., and Vaux, D. J. (2016). Dynamics of the formation of a hydrogel by a pathogenic amyloid peptide: Islet amyloid polypeptide. *Scientific Reports*, 6.

[Johnson et al., 2009] Johnson, B. S., Snead, D., Lee, J. J., McCaffery, J. M., Shorter, J., and Gitler, A. D. (2009). TDP-43 is intrinsically aggregation-prone, and amyotrophic lateral sclerosis-linked mutations accelerate aggregation and increase toxicity. *Journal of Biological Chemistry*, 284(30):20329–20339.

[Jönsson et al., 2008] Jönsson, K. I., Rabbow, E., Schill, R. O., Harms-Ringdahl, M., and Rettberg, P. (2008). Tardigrades survive exposure to space in low Earth orbit. *Current Biology*, 18(17):R729–R731.

[Judson, 1997] Judson, O. P. (1997). A model of asexuality and clonal diversity: Cloning the Red Queen. *Journal of Theoretical Biology*, 186(1):33–40.

[Kalwarczyk et al., 2011] Kalwarczyk, T., Ziębacz, N., Bielejewska, A., Zaboklicka, E., Koynov, K., Szymański, J., Wilk, A., Patkowski, A., Gapiński, J., Butt, H. J., and Hołyst, R. (2011). Comparative analysis of viscosity of complex liquids and cytoplasm of mammalian cells at the nanoscale. *Nano Letters*, 11(5):2157–2163.

[Kato et al., 2012] Kato, M., Han, T. W., Xie, S., Shi, K., Du, X., Wu, L. C., Mirzaei, H., Goldsmith, E. J., Longgood, J., Pei, J., Grishin, N. V., Frantz, D. E., Schneider, J. W., Chen, S., Li, L., Sawaya, M. R., Eisenberg, D., Tycko, R., and McKnight, S. L. (2012). Cell-free formation of RNA granules: Low complexity sequence domains form dynamic fibers within hydrogels. *Cell*, 149(4):753–767.

[Kim et al., 2013] Kim, H. J., Kim, N. C., Wang, Y. D., Scarborough, E. A., Moore, J., Diaz, Z., MacLea, K. S., Freibaum, B., Li, S., Molliex, A., Kanagaraj, A. P., Carter, R., Boylan, K. B., Wojtas, A. M., Rademakers, R., Pinkus, J. L., Greenberg, S. A., Trojanowski, J. Q., Traynor, B. J., Smith, B. N., Topp, S., Gkazi, A. S., Miller, J., Shaw, C. E., Kottlors, M., Kirschner, J., Pestronk, A., Li, Y. R., Ford, A. F., Gitler, A. D., Benatar, M., King, O. D., Kimonis, V. E., Ross, E. D., Weihl, C. C., Shorter, J., and Taylor, J. P. (2013). Mutations in prion-like domains in hnRNPA2B1 and hnRNPA1 cause multisystem proteinopathy and ALS. *Nature*, 495(7442):467–473.

[Kinoshita et al., 2012] Kinoshita, Y., Kalir, T., Dottino, P., and Kohtz, D. S. (2012). Nuclear Distributions of NUP62 and NUP214 Suggest Architectural Diversity and Spatial Patterning among Nuclear Pore Complexes. *PLoS ONE*, 7(4):e36137.

[Klapper et al., 2002] Klapper, I., Rupp, C. J., Cargo, R., Purvedorj, B., and Stoodley, P. (2002). Viscoelastic fluid description of bacterial biofilm material properties. *Biotechnology and Bioengineering*, 80(3):289–296.

[Kondo et al., 2015] Kondo, K., Kubo, T., and Kunieda, T. (2015). Suggested Involvement of PP1/PP2A Activity and De Novo Gene Expression in Anhydro-

biotic Survival in a Tardigrade, Hypsibius dujardini, by Chemical Genetic Approach. *PLOS ONE*, 10(12):e0144803.

[Körstgens et al., 2001] Körstgens, V., Flemming, H. C., Wingender, J., and Borchard, W. (2001). Uniaxial compression measurement device for investigation of the mechanical stability of biofilms. *Journal of Microbiological Methods*, 46(1):9–17.

[Kraemer et al., 1994] Kraemer, D., Wozniak, R. W., Blobel, G., and Radu, A. (1994). The human CAN protein, a putative oncogene product associated with myeloid leukemogenesis, is a nuclear pore complex protein that faces the cytoplasm. *Proceedings of the National Academy of Sciences of the United States of America*, 91(4):1519–1523.

[Krysmann et al., 2008] Krysmann, M. J., Castelletto, V., Kelarakis, A., Hamley, I. W., Hule, R. A., and Pochan, D. J. (2008). Self-Assembly and Hydrogelation of an Amyloid Peptide Fragment. *Biochemistry*, 47(16):4597–4605.

[Kuimova et al., 2009] Kuimova, M. K., Botchway, S. W., Parker, A. W., Balaz, M., Collins, H. A., Anderson, H. L., Suhling, K., and Ogilby, P. R. (2009). Imaging intracellular viscosity of a single cell during photoinduced cell death. *Nature Chemistry*, 1(1):69–73.

[Kuimova et al., 2008] Kuimova, M. K., Yahioglu, G., Levitt, J. A., and Suhling, K. (2008). Molecular Rotor Measures Viscosity of Live Cells via Fluorescence Lifetime Imaging. *Journal of the American Chemical Society*, 130(21):6672–6673.

[Kwan et al., 2006] Kwan, A. H., Winefield, R. D., Sunde, M., Matthews, J. M., Haverkamp, R. G., Templeton, M. D., and Mackay, J. P. (2006). Structural basis for rodlet assembly in fungal hydrophobins. *Proceedings of the National Academy of Sciences of the United States of America*, 103(10):3621–3626.

[Kwiatkowski et al., 2009] Kwiatkowski, T. J., Bosco, D. A., LeClerc, A. L., Tamrazian, E., Vanderburg, C. R., Russ, C., Davis, A., Gilchrist, J., Kasarskis, E. J., Munsat, T., Valdmanis, P., Rouleau, G. A., Hosler, B. A., Cortelli, P., De Jong, P. J., Yoshinaga, Y., Haines, J. L., Pericak-Vance, M. A., Yan, J., Ticozzi, N., Siddique, T., McKenna-Yasek, D., Sapp, P. C., Horvitz, H. R., Landers, J. E., and Brown, R. H. (2009). Mutations in the FUS/TLS gene on chromosome 16 cause familial amyotrophic lateral sclerosis. *Science*, 323(5918):1205–1208.

[Lakshmanan et al., 2013] Lakshmanan, A., Cheong, D. W., Accardo, A., Di Fabrizio, E., Riekel, C., and Hauser, C. A. (2013). Aliphatic peptides show similar self-assembly to amyloid core sequences, challenging the importance of aromatic interactions in amyloidosis. *Proceedings of the National Academy of Sciences of the United States of America*, 110(2):519–524.

[Lane and Martin, 2010] Lane, N. and Martin, W. (2010). The energetics of genome complexity. *Nature*, 467(7318):929–934.

[Latgé et al., 1986] Latgé, J.-P., Beauvais, A., and Vey, A. (1986). Wall synthesis in the entomophthorales and its role in the immune-reaction of infected insects. *Dev. Comp. Immunol.*, 10(639).

[Le Magrex-Debar et al., 2000] Le Magrex-Debar, E., Lemoine, J., Gellé, M. P., Jacquelin, L. F., and Choisy, C. (2000). Evaluation of biohazards in dehydrated biofilms on foodstuff packaging. *International Journal of Food Microbiology*, 55(1-3):239–243.

[Lei et al., 2011] Lei, Y., Rahim, M., Ng, Q., and Segura, T. (2011). Hyaluronic acid and fibrin hydrogels with concentrated DNA/PEI polyplexes for local gene delivery. *Journal of Controlled Release*, 153(3):255–261.

[Lepère et al., 2007] Lepère, M., Chevallard, C., Hernandez, J.-F., Mitraki, A., and Guenoun, P. (2007). Multiscale Surface Self-Assembly of an Amyloid-like Peptide. *Langmuir*, 23(15):8150–8155.

[Levi et al., 2005] Levi, V., Ruan, Q. Q., and Gratton, E. (2005). 3-D particle tracking in a two-photon microscope: Application to the study of molecular dynamics in cells. *Biophysical Journal*, 88(4):2919–2928.

[Levitt et al., 2009] Levitt, J. A., Kuimova, M. K., Yahioglu, G., Chung, P.-H., Suhling, K., and Phillips, D. (2009). Membrane-Bound Molecular Rotors Measure Viscosity in Live Cells via Fluorescence Lifetime Imaging. *The Journal of Physical Chemistry C*, 113(27):11634–11642.

[Li et al., 2019] Li, Y., Aksenova, V., Yu, J., Ma, P., Arnaoutov, A., Dasso, M., and Yang, W. (2019). Copy Number and Function of Individual Disordered Proteins in the Nuclear Pore Complex Revealed by Combining Auxin-Inducible Degron Strategy and High-Speed Single -Molecule Microscopy. *Biophysical Journal*, 116(3):441a.

[Li et al., 2013] Li, Y. R., King, O. D., Shorter, J., and Gitler, A. D. (2013). Stress granules as crucibles of ALS pathogenesis.

[Lieleg and Ribbeck, 2011] Lieleg, O. and Ribbeck, K. (2011). Biological hydrogels as selective diffusion barriers.

[Lim et al., 2016] Lim, L., Wei, Y., Lu, Y., and Song, J. (2016). ALS-Causing Mutations Significantly Perturb the Self-Assembly and Interaction with Nucleic Acid of the Intrinsically Disordered Prion-Like Domain of TDP-43. *PLOS Biology*, 14(1):e1002338.

[Linder, 2009] Linder, M. B. (2009). Hydrophobins: Proteins that self assemble at interfaces.

[Lindner et al., 2008] Lindner, A. B., Madden, R., Demarez, A., Stewart, E. J., and Taddei, F. (2008). Asymmetric segregation of protein aggregates is associated with cellular aging and rejuvenation. *Proceedings of the National Academy of Sciences of the United States of America*, 105(8):3076–81.

[Liu et al., 2013] Liu, F., Wu, T., Cao, J., Cui, S., Yang, Z., Qiang, X., Sun, S., Song, F., Fan, J., Wang, J., and Peng, X. (2013). Ratiometric Detection of Viscosity Using a Two-Photon Fluorescent Sensor. *Chemistry - A European Journal*, 19(5):1548–1553.

[Liu-Yesucevitz et al., 2010] Liu-Yesucevitz, L., Bilgutay, A., Zhang, Y.-J., Vanderwyde, T., Citro, A., Mehta, T., Zaarur, N., McKee, A., Bowser, R., Sherman, M., Petrucelli, L., and Wolozin, B. (2010). Tar DNA Binding Protein-43 (TDP-43) Associates with Stress Granules: Analysis of Cultured Cells and Pathological Brain Tissue. *PLoS ONE*, 5(10):e13250.

[Lizana et al., 2008] Lizana, L., Bauer, B., and Orwar, O. (2008). Controlling the rates of biochemical reactions and signaling networks by shape and volume changes. *Proceedings of the National Academy of Sciences of the United States of America*, 105(11):4099–4104.

[Loison et al., 2013] Loison, P., Hosny, N. A., Gervais, P., Champion, D., Kuimova, M. K., and Perrier-Cornet, J. M. (2013). Direct investigation of viscosity of an atypical inner membrane of Bacillus spores: A molecular rotor/FLIM study. *Biochimica et Biophysica Acta - Biomembranes*, 1828(11):2436–2443.

[Lomakin et al., 1996] Lomakin, A., Chung, D. S., Benedek, G. B., Kirschner, D. A., and Teplow, D. B. (1996). On the nucleation and growth of amyloid β-protein fibrils: Detection of nuclei and quantitation of rate constants. *Proceedings of the National Academy of Sciences of the United States of America*, 93(3):1125–1129.

[Mackay et al., 2001] Mackay, J. P., Matthews, J. M., Winefield, R. D., Mackay, L. G., Haverkamp, R. G., and Templeton, M. D. (2001). The hydrophobin EAS is largely unstructured in solution and functions by forming amyloid-like structures. *Structure*, 9(2):83–91.

[Manno et al., 2010] Manno, M., Giacomazza, D., Newman, J., Martorana, V., and San Biagio, P. L. (2010). Amyloid Gels: Precocious Appearance of Elastic Properties during the Formation of an Insulin Fibrillar Network. *Langmuir*, 26(3):1424–1426.

[Martins et al., 2018] Martins, R. S., José, A. C., Faria, J. M. R., and Pereira, W. V. S. (2018). Ultrastructural analysis of the loss of desiccation tolerance in germinating Eremanthus erythropappus seeds. *Journal of Forestry Research*.

[Mazerski et al., 1998] Mazerski, J., Martelli, S., and Borowski, E. (1998). The geometry of intercalation complex of antitumor mitoxantrone and ametantrone with DNA: Molecular dynamics simulations. *Acta Biochimica Polonica*, 45(1):1–11.

[McDonald et al., 2011] McDonald, K. K., Aulas, A., Destroismaisons, L., Pickles, S., Beleac, E., Camu, W., Rouleau, G. A., and Vande Velde, C. (2011). TAR DNA-binding protein 43 (TDP-43) regulates stress granule dynamics via differential regulation of G3BP and TIA-1. *Human Molecular Genetics*, 20(7):1400–1410.

[Murakami et al., 2015] Murakami, T., Qamar, S., Lin, J. Q., Schierle, G. S., Rees, E., Miyashita, A., Costa, A. R., Dodd, R. B., Chan, F. T., Michel, C. H., Kronenberg-Versteeg, D., Li, Y., Yang, S. P., Wakutani, Y., Meadows, W., Ferry, R. R., Dong, L., Tartaglia, G. G., Favrin, G., Lin, W. L., Dickson, D. W., Zhen, M., Ron, D., Schmitt-Ulms, G., Fraser, P. E., Shneider, N. A., Holt, C., Vendruscolo, M., Kaminski, C. F., and St George-Hyslop, P. (2015). ALS/FTD Mutation-Induced Phase Transition of FUS Liquid Droplets and Reversible Hydrogels into Irreversible Hydrogels Impairs RNP Granule Function. *Neuron*, 88(4):678–690.

[Murase et al., 2004] Murase, K., Fujiwara, T., Umemura, Y., Suzuki, K., Iino, R., Yamashita, H., Saito, M., Murakoshi, H., Ritchie, K., and Kusumi, A. (2004).

Ultrafine membrane compartments for molecular diffusion as revealed by single molecule techniques. *Biophysical Journal*, 86(6):4075–4093.

[Nadiv et al., 1994] Nadiv, O., Shinitzky, M., Manu, H., Hecht, D., Roberts, C. T., LeRoith, D., and Zick, Y. (1994). Elevated protein tyrosine phosphatase activity and increased membrane viscosity are associated with impaired activation of the insulin receptor kinase in old rats. *Biochemical Journal*, 298(2):443–450.

[Neumann et al., 2006] Neumann, M., Sampathu, D. M., Kwong, L. K., Truax, A. C., Micsenyi, M. C., Chou, T. T., Bruce, J., Schuck, T., Grossman, M., Clark, C. M., McCluskey, L. F., Miller, B. L., Masliah, E., Mackenzie, I. R., Feldman, H., Feiden, W., Kretzschmar, H. A., Trojanowski, J. Q., and Lee, V. M. (2006). Ubiquitinated TDP-43 in frontotemporal lobar degeneration and amyotrophic lateral sclerosis. *Science*, 314(5796):130–133.

[Oliveira et al., 2016] Oliveira, S. M. D., Neeli-Venkata, R., Goncalves, N. S. M., Santinha, J. A., Martins, L., Tran, H., Mäkelä, J., Gupta, A., Barandas, M., Häkkinen, A., Lloyd-Price, J., Fonseca, J. M., and Ribeiro, A. S. (2016). Increased cytoplasm viscosity hampers aggregate polar segregation in *Escherichia coli*. *Molecular Microbiology*, 99(4):686–699.

[Ölveczky and Verkman, 1998] Ölveczky, B. P. and Verkman, A. S. (1998). Monte Carlo analysis of obstructed diffusion in three dimensions: Application to molecular diffusion in organelles. *Biophysical Journal*, 74(5):2722–2730.

[Pal et al., 2016] Pal, S., Chakraborty, H., Bandari, S., Yahioglu, G., Suhling, K., and Chattopadhyay, A. (2016). Molecular rheology of neuronal membranes explored using a molecular rotor: Implications for receptor function.

[Pallarés et al., 2017] Pallarés, S., Botella-Cruz, M., Arribas, P., Millán, A., and Velasco, J. (2017). Aquatic insects in a multistress environment: cross-tolerance to salinity and desiccation. *The Journal of Experimental Biology*, 220(7):1277–1286.

[Pappu et al., 2008] Pappu, R. V., Wang, X., Vitalis, A., and Crick, S. L. (2008). A polymer physics perspective on driving forces and mechanisms for protein aggregation.

[Parker et al., 2010] Parker, W. C., Chakraborty, N., Vrikkis, R., Elliott, G., Smith, S., and Moyer, P. J. (2010). High-resolution intracellular viscosity measurement using time-dependent fluorescence anisotropy. *Optics Express*, 18(16):16607.

[Patel et al., 2015] Patel, A., Lee, H. O., Jawerth, L., Maharana, S., Jahnel, M., Hein, M. Y., Stoynov, S., Mahamid, J., Saha, S., Franzmann, T. M., Pozniakovski, A., Poser, I., Maghelli, N., Royer, L. A., Weigert, M., Myers, E. W., Grill, S., Drechsel, D., Hyman, A. A., and Alberti, S. (2015). A Liquid-to-Solid Phase Transition of the ALS Protein FUS Accelerated by Disease Mutation. *Cell*, 162(5):1066–1077.

[Peterson et al., 2015] Peterson, B. W., He, Y., Ren, Y., Zerdoum, A., Libera, M. R., Sharma, P. K., van Winkelhoff, A. J., Neut, D., Stoodley, P., van der Mei, H. C., and Busscher, H. J. (2015). Viscoelasticity of biofilms and their recalcitrance to mechanical and chemical challenges.

[Principles and Valeur,] Principles, F. . and Valeur, A. B. Bernard Valeur Molecular Fluorescence Principles and Applications. Technical report.

[Protter and Parker, 2016] Protter, D. S. and Parker, R. (2016). Principles and Properties of Stress Granules.

[Qin et al., 2018] Qin, J., Shangguan, Z., and Xi, W. (2018). Seasonal variations of leaf traits and drought adaptation strategies of four common woody species in South Texas, USA. *Journal of Forestry Research*.

[Rajanala and Nandicoori, 2012] Rajanala, K. and Nandicoori, V. K. (2012). Localization of Nucleoporin Tpr to the Nuclear Pore Complex Is Essential for Tpr Mediated Regulation of the Export of Unspliced RNA. *PLoS ONE*, 7(1):e29921.

[Rebecchi et al., 2006] Rebecchi, L., Guidetti, R., Borsari, S., Altiero, T., and Bertolani, R. (2006). Dynamics of Long-term Anhydrobiotic Survival of Lichen-dwelling Tardigrades. *Hydrobiologia*, 558(1):23–30.

[Rebecci et al., 2007] Rebecci, L., Altiero, T., and Guidetti, R. (2007). *Anhydrobiosis: the extreme limit of desiccation tolerance*, volume 4. University of Modena and Reggio Emilia.

[Ricci, 1987] Ricci, C. N. (1987). Ecology of bdelloids: how to be successful. In *Rotifer Symposium IV*, pages 117–127. Springer Netherlands.

[Rijkers et al., 2002] Rijkers, D. T. S., Höppener, J. W. M., Posthuma, G., Lips, C. J. M., and Liskamp, R. M. J. (2002). Inhibition of Amyloid Fibril Formation of Human Amylin by N-Alkylated Amino Acid and -Hydroxy Acid Residue Containing Peptides. *Chemistry - A European Journal*, 8(18):4285–4291.

[Rubert Pérez et al., 2015] Rubert Pérez, C. M., Stephanopoulos, N., Sur, S., Lee, S. S., Newcomb, C., and Stupp, S. I. (2015). The Powerful Functions of Peptide-Based Bioactive Matrices for Regenerative Medicine. *Annals of Biomedical Engineering*, 43(3):501–514.

[Saini and Chauhan, 2014] Saini, A. and Chauhan, V. S. (2014). Self-Assembling Properties of Peptides Derived from TDP-43 C-Terminal Fragment. *Langmuir*, 30(13):3845–3856.

[Selvaggi et al., 2010] Selvaggi, L., Salemme, M., Vaccaro, C., Pesce, G., Rusciano, G., Sasso, A., Campanella, C., and Carotenuto, R. (2010). Multiple-Particle-Tracking to investigate viscoelastic properties in living cells.

[Shigeta et al., 1997] Shigeta, M., Komatsuzawa, H., Sugai, M., Suginaka, H., and Usui, T. (1997). Effect of the Growth Rate of Pseudomonas aeruginosa Biofilms on the Susceptibility to Antimicrobial Agents. *Chemotherapy*, 43(2):137–141.

[Smith et al., 2016] Smith, F. W., Boothby, T. C., Giovannini, I., Rebecchi, L., Jockusch, E. L., and Correspondence, B. G. (2016). The Compact Body Plan of Tardigrades Evolved by the Loss of a Large Body Region. *Current Biology*, 26:224–229.

[Su et al., 2016] Su, D., Teoh, C. L., Gao, N., Xu, Q. H., and Chang, Y. T. (2016). A simple bodipy-based viscosity probe for imaging of cellular viscosity in live cells. *Sensors (Switzerland)*, 16(9).

[Suhling et al., 2004] Suhling, K., Siegel, J., Lanigan, P. M. P., Lévêque-Fort, S., Webb, S. E. D., Phillips, D., Davis, D. M., and French, P. M. W. (2004). Time-resolved fluorescence anisotropy imaging applied to live cells. *Optics Letters*, 29(6):584.

[Talal et al., 2015] Talal, S., Ayali, A., and Gefen, E. (2015). Discontinuous gas-exchange cycle characteristics are differentially affected by hydration state and energy metabolism in gregarious and solitary desert locusts. *Journal of Experimental Biology*, 218(23):3807–3815.

[Tanaka et al., 2015] Tanaka, S., Tanaka, J., Miwa, Y., Horikawa, D. D., Katayama, T., Arakawa, K., Toyoda, A., Kubo, T., and Kunieda, T. (2015). Novel mitochondria-targeted heat-soluble proteins identified in the anhydrobiotic tardigrade improve osmotic tolerance of human cells. *PLoS ONE*, 10(2).

[Tapia and Koshland, 2014] Tapia, H. and Koshland, D. E. (2014). Trehalose is a versatile and long-lived chaperone for desiccation tolerance. *Current Biology*, 24(23):2758–2766.

[Teitzel and Parsek, 2003] Teitzel, G. M. and Parsek, M. R. (2003). Heavy metal resistance of biofilm and planktonic Pseudomonas aeruginosa. *Applied and Environmental Microbiology*, 69(4):2313–2320.

[Towler et al., 2003] Towler, B. W., Rupp, C. J., Cunningham, A. L., and Stoodley, P. (2003). Viscoelastic Properties of a Mixed Culture Biofilm from Rheometer Creep Analysis. *Biofouling*, 19(5):279–285.

[Trappmann et al., 2012] Trappmann, B., Gautrot, J. E., Connelly, J. T., Strange, D. G., Li, Y., Oyen, M. L., Cohen Stuart, M. A., Boehm, H., Li, B., Vogel, V., Spatz, J. P., Watt, F. M., and Huck, W. T. (2012). Extracellular-matrix tethering regulates stem-cell fate. *Nature Materials*, 11(7):642–649.

[Tseng, 2004] Tseng, Y. (2004). Micro-organization and visco-elasticity of the interphase nucleus revealed by particle nanotracking. *Journal of Cell Science*, 117(10):2159–2167.

[Tubert-Brohman et al., 2013] Tubert-Brohman, I., Sherman, W., Repasky, M., and Beuming, T. (2013). Improved docking of polypeptides with glide. *Journal of Chemical Information and Modeling*, 53(7):1689–1699.

[Vance et al., 2009] Vance, C., Rogelj, B., Hortobágyi, T., De Vos, K. J., Nishimura, A. L., Sreedharan, J., Hu, X., Smith, B., Ruddy, D., Wright, P., Ganesalingam, J., Williams, K. L., Tripathi, V., Al-Saraj, S., Al-Chalabi, A., Leigh, P. N., Blair, I. P., Nicholson, G., De Belleroche, J., Gallo, J. M., Miller, C. C., and Shaw, C. E. (2009). Mutations in FUS, an RNA processing protein, cause familial amyotrophic lateral sclerosis type 6. *Science*, 323(5918):1208–1211.

[Vance et al., 2013] Vance, C., Scotter, E. L., Nishimura, A. L., Troakes, C., Mitchell, J. C., Kathe, C., Urwin, H., Manser, C., Miller, C. C., Hortobágyi, T., Dragunow, M., Rogelj, B., and Shaw, C. E. (2013). ALS mutant FUS disrupts nuclear localization and sequesters wild-type FUS within cytoplasmic stress granules. *Human Molecular Genetics*, 22(13):2676–2688.

[Vyšniauskas et al., 2016] Vyšniauskas, A., Qurashi, M., and Kuimova, M. K. (2016). A Molecular Rotor that Measures Dynamic Changes of Lipid Bi-

layer Viscosity Caused by Oxidative Stress. *Chemistry - A European Journal*, 22(37):13210–13217.

[Walters et al., 2003] Walters, M. C., Roe, F., Bugnicourt, A., Franklin, M. J., and Stewart, P. S. (2003). Contributions of antibiotic penetration, oxygen limitation, and low metabolic activity to tolerance of Pseudomonas aeruginosa biofilms to ciprofloxacin and tobramycin. *Antimicrobial Agents and Chemotherapy*, 47(1):317–323.

[Wang et al., 2013] Wang, L., Xiao, Y., Tian, W., and Deng, L. (2013). Activatable Rotor for Quantifying Lysosomal Viscosity in Living Cells. *Journal of the American Chemical Society*, 135(8):2903–2906.

[Wang et al., 2004] Wang, X., Permentier, H. P., Rink, R., Kruijtzer, J. A., Liskamp, R. M., Wösten, H. A., Poolman, B., and Robillard, G. T. (2004). Probing the self-assembly and the accompanying structural changes of hydrophobin SC3 on a hydrophobic surface by spectrometry. *Biophysical Journal*, 87(3):1919–1928.

[Wheeler and Hyman, 2018] Wheeler, R. J. and Hyman, A. A. (2018). Controlling compartmentalization by non-membrane-bound organelles.

[Wheeler et al., 2019] Wheeler, R. J., Lee, H. O., Poser, I., Pal, A., Doeleman, T., Kishigami, S., Kour, S., Anderson, E. N., Marrone, L., Murthy, A. C., Jahnel, M., Zhang, X., Boczek, E., Fritsch, A., Fawzi, N. L., Sterneckert, J., Pandey, U., David, D. C., Davis, B. G., Baldwin, A. J., Hermann, A., Bickle, M., Alberti, S., and Hyman, A. A. (2019). Small molecules for modulating protein driven liquid-liquid phase separation in treating neurodegenerative disease.

[Winston and Bates, 1960] Winston, P. W. and Bates, D. H. (1960). Saturated Solutions For the Control of Humidity in Biological Research. *Ecology*, 41(1):232–237.

[Winter and Mours, 1997] Winter, H. H. and Mours, M. (1997). Rheology of Polymers Near Liquid-Solid Transitions. *Advances in Polymer Science*, 134:164–234.

[Wösten, 2001] Wösten, H. A. B. (2001). Hydrophobins: Multipurpose Proteins. *Annual Review of Microbiology*, 55(1):625–646.

[Wright, 1989] Wright, J. C. (1989). Desiccation Tolerance and Water-Retentive Mechanisms in Tardigrades. *Journal of Experimental Biology*, 142(1).

[Wu et al., 2001] Wu, M. M., Grabe, M., Adams, S., Tsien, R. Y., Moore, H. P. H., and Machen, T. E. (2001). Mechanisms of pH Regulation in the Regulated Secretory Pathway. *Journal of Biological Chemistry*, 276(35):33027–33035.

[Wu et al., 2013] Wu, Y., Štefl, M., Olzyńska, A., Hof, M., Yahioglu, G., Yip, P., Casey, D. R., Ces, O., Humpolíčková, J., and Kuimova, M. K. (2013). Molecular rheometry: Direct determination of viscosity in Lo and Ld lipid phases via fluorescence lifetime imaging. *Physical Chemistry Chemical Physics*, 15(36):14986–14993.

[Yadav and Sharma, 2014] Yadav, P. and Sharma, V. K. (2014). Correlated changes in life history traits in response to selection for faster pre-adult development in the fruit fly Drosophila melanogaster. *Journal of Experimental Biology*, 217(4):580–589.

[Yamada et al., 2010] Yamada, J., Phillips, J. L., Patel, S., Goldfien, G., Calestagne-Morelli, A., Huang, H., Reza, R., Acheson, J., Krishnan, V. V., Newsam, S., Gopinathan, A., Lau, E. Y., Colvin, M. E., Uversky, V. N., and Rexach, M. F. (2010). A Bimodal Distribution of Two Distinct Categories of Intrinsically-Disordered Structures with Separate Functions in FG Nucleoporins as Manuscript M000035-MCP201 Downloaded from. Technical report.

[Yamaguchi et al., 2012] Yamaguchi, A., Tanaka, S., Yamaguchi, S., Kuwahara, H., Takamura, C., Imajoh-Ohmi, S., Horikawa, D. D., Toyoda, A., Katayama, T., Arakawa, K., Fujiyama, A., Kubo, T., and Kunieda, T. (2012). Two Novel Heat-Soluble Protein Families Abundantly Expressed in an Anhydrobiotic Tardigrade. *PLoS ONE*, 7(8):e44209.

[Yang et al., 2012] Yang, Y., Dicko, C., Bain, C. D., Gong, Z., Jacobs, R. M., Shao, Z., Terry, A. E., and Vollrath, F. (2012). Behavior of silk protein at the air-water interface. *Soft Matter*, 8(37):9705–9712.

[Yang et al., 2014] Yang, Z., He, Y., Lee, J. H., Chae, W. S., Ren, W. X., Lee, J. H., Kang, C., and Kim, J. S. (2014). A Nile Red/BODIPY-based bimodal probe sensitive to changes in the micropolarity and microviscosity of the endoplasmic reticulum. *Chemical Communications*, 50(79):11672–11675.

[Yoon et al., 2011] Yoon, H. J., Dakanali, M., Lichlyter, D., Chang, W. M., Nguyen, K. A., Nipper, M. E., Haidekker, M. A., and Theodorakis, E. A. (2011). Synthe-

sis and evaluation of self-calibrating ratiometric viscosity sensors. *Organic and Biomolecular Chemistry*, 9(9):3530–3540.

[Zampieri et al., 2010] Zampieri, F., Wösten, H. A. B., and Scholtmeijer, K. (2010). Creating Surface Properties Using a Palette of Hydrophobins. *Materials*, 3(9):4607–4625.

[Zhu et al., 2014] Zhu, H., Fan, J., Li, M., Cao, J., Wang, J., and Peng, X. (2014). A "Distorted-BODIPY"-Based Fluorescent Probe for Imaging of Cellular Viscosity in Live Cells. *Chem. Europe K.*, 20:4691–4696.

[Zhu and Marchant, 2011] Zhu, J. and Marchant, R. E. (2011). Design properties of hydrogel tissue-engineering scaffolds.

[Zhu et al., 2016] Zhu, Y., Liu, T. W., Madden, Z., Yuzwa, S. A., Murray, K., Cecioni, S., Zachara, N., and Vocadlo, D. J. (2016). Post-translational O-GlcNAcylation is essential for nuclear pore integrity and maintenance of the pore selectivity filter. *Journal of Molecular Cell Biology*, 8(1):2–16.

[Zubenko et al., 1999] Zubenko, G. S., Kopp, U., Seto, T., and Firestone, L. L. (1999). Platelet membrane fluidity individuals at risk for Alzheimer's disease: A comparison of results from fluorescence spectroscopy and electron spin resonance spectroscopy. *Psychopharmacology*, 145(2):175–180.